Title
Drag Measurements On A Platoon Of Vehicles

Authors
Zabat, Michael
Farascaroli, Stefano
Browand, Frederick
et al.

Publication Date
1994

CALIFORNIA PATH PROGRAM
INSTITUTE OF TRANSPORTATION STUDIES
UNIVERSITY OF CALIFORNIA, BERKELEY

Drag Measurements on a Platoon of Vehicles

Michael Zabat
Stefano Frascaroli
Frederick Browand
with contributions from
Michael Nestlerode and John Baez

California PATH Research Paper

UCB-ITS-PRR-93-27

This work was performed as part of the California PATH Program of the University of California, in cooperation with the State of California Business, Transportation, and Housing Agency, Department of Transportation; and the United States Department Transportation, Federal Highway Administration.

February 1994

ISSN 1055-1425

Drag Measurements on a Platoon of Vehicles

A Preliminary Report

Presented to the California Department of Transportation

Partners for Advanced Transit and Highways(PATH) Program

by

Michael Zabat

Stefano Frascaroli

and

Frederick Browand

with contributions from

Michael Nestlerode and John Baez

25 January, 1994

Abstract

This report details the design and implementation of wind tunnel tests to evaluate the aerodynamic performance of individual members of 2, 3 and 4-vehicle platoons. The purpose of the tests described here is to quantify the behavior of vehicle drag as a function of vehicle spacing. One-eighth scale models of the 1991 GM Lumina APV are used as the prototype vehicle. Each model is fitted with a force balance capable of measuring drag, side force and yawing moment. A porous ground plane equipped with suction is used to simulate the road surface. Results show a reduction in average drag for all platoon members as a function of both inter-vehicle spacing and the number of vehicles in the platoon. The reduction in average drag is measured to be almost 40% for a 4-vehicle platoon at ½-car length spacing. Based on the data presented, some conclusions are drawn as to the expected drag reduction for a platoon of any size. The low average drag coefficients for platoon operation translate directly to increased fuel savings and to less pollution per mile traveled.

Executive Summary

This report details the design and implementation of wind tunnel tests to evaluate the aerodynamic performance of individual members of 2, 3 and 4-vehicle platoons. The purpose of the tests described here is to quantify the behavior of vehicle drag, or-more properly-drag coefficient, as a function of vehicle spacing. One-eighth scale models of the 1991 GM Lumina van are used as the prototype vehicle. The design and fabrication of force balances capable of measuring drag, side force and yawing moment is described (each vehicle contains a force balance). Models are mounted above a porous ground plane surface designed to control the surface boundary layer thickness.

When the separation between vehicles is greater than about one car-length, there is only weak interaction between members of the platoon. Roughly speaking, the values of drag coefficient decrease as one moves aft in the platoon, so the most downstream platoon member experiences the lowest drag. This behavior can be understood in terms of the progressively lower airstream velocity seen by each of the trailing vehicles. For separation distance less than one car-length, the interaction between platoon members is strong. All members of the platoon experience drag reduction-including the most forward vehicle. The interior members of the platoon have lower drag coefficients than either the most forward or most rear vehicle. The numerically averaged drag coefficient for the platoon is substantially less than the single-vehicle drag coefficient, and decreases with increasing number of vehicles within the platoon. The average drag coefficient for a platoon of four vehicles at one-half vehicle spacing is 62 per cent of the single car value. Even lower drags are predicted for platoons containing more vehicles and also for smaller spacings. The low average drag coefficients for platoon operation translate directly to increased fuel savings and to less pollution per mile traveled.

Table of Contents

I. Overview

Establishing Confidence in Wind Tunnel Test Results/The Significance of Drag Coefficient
When bodies under aerodynamic study are modeled in a wind tunnel test, all possible care must be taken to establish conditions consistent with full scale operation. In principle, the model test should reflect perfect dynamic similarity as well as perfect geometrical similarity. Such perfection is never realized in practice. Even if the model tested is a full-scale vehicle, complete in every detail, the presence of the wind tunnel walls destroys perfect geometric similarity. In most wind tunnel tests, dynamic and geometric similarity are only approximately established for a variety of reasons. Wind tunnel tests still give valuable information about aerodynamic performance, provided the limitations of the test are kept in mind.

Dynamic similarity first requires the definition of force coefficients for the body. Since we are primarily interested in drag force, a drag coefficient is defined,

$$C_D = \frac{D}{\frac{1}{2}\rho U^2 A}$$

where D = measured drag
ρ = air density
U = vehicle forward speed, wind tunnel speed
A = Maximum cross-sectional area of the body perpendicular to the flow

Couching discussion in terms of ***drag coefficient*** rather than in terms of ***drag*** automatically accounts for differences in vehicle size and vehicle relative velocity. It allows one to make predictions for the performance of the full scale vehicle from wind tunnel model measurements. In addition, perfect dynamic similarity requires that the Reynolds number of the model flow be made to match the Reynolds number in the full scale operation.

$$Re = \frac{Ud}{\nu}$$

where d = characteristic length scale
v = kinematic viscosity of air

The magnitude of the Reynolds number expresses the ratio of fluid inertia force to fluid-viscous effect, or shear stress. When the Reynolds number is large, the fluid moves in response to differences in pressure within the flow field. Only in very thin ***boundary layer*** regions adjacent to surfaces are viscous shearing stresses important. The characteristic length scale of our vehicle model is 1/8th that of the full scale vehicle. Since the test is conducted with air as the fluid, the viscosity v is the same for both cases. To keep ***Re*** constant, the freestream velocity in the test case

must be 8 times higher than the full-scale vehicle velocity. This, of course, is not possible-model Reynolds numbers are lower than Reynolds numbers for full scale operation. An automobile traveling at highway speed may correspond to $Re = O(10^6\text{-}10^7)$, while our wind tunnel tests are conducted at Reynolds numbers about one order of magnitude lower. To account for these differences, and to judge the sensitivity of the force measurements to changes in Reynolds number, we will frequently present measurements at several Reynolds numbers. Another simulation technique is to utilize a series of small roughness elements to artificially "trip" the boundary layer on the model. Tripping insures a turbulent boundary layer more nearly in character with a boundary layer at higher Reynolds number.

The model and full-scale vehicle are geometrically similar in the sense that all body dimensions have been scaled by the same ratio. The mold used to cast the models is fashioned by a stereo-lithographic process using computer-generated coordinates. For all practical purposes, the model is an exact replica. However, all minor external features such as window frames, side mirrors, door handles, windshield wipers, etc., have been removed. Also, the details of the undercarriage have been left out, and the wheels are stationary. The absence of these protuberances on the full-scale vehicle would result in a lower C_D.

The Unwanted Presence of the Ground Plane Boundary Layer In the case of ground vehicles an additional effect is introduced by the presence of the road surface. If one uses a flat plate to model the road surface in a wind-tunnel, a layer of slow moving fluid (the ground plane boundary layer) grows continuously in the downstream direction. This layer does not exist on the actual road surface since it is the vehicle that is in motion and not the medium (air). It is necessary then to minimize the thickness of the ground plane boundary layer, δ, in wind-tunnel tests. The growth of a turbulent boundary layer on a flat plate can be approximated by

$$\delta = \frac{0.37x}{Re_x^{0.2}}$$

where x is the distance from the leading edge. Based upon the above expression, the thickness of the boundary layer at 4 model lengths (1.22m) from the start of the ground plane at 25m/s would be about 2.46 cm. Four model lengths would correspond to a case where 2 models are in the tunnel at 1 length spacing, the first model being placed 1 length from the leading edge. Further down the plate, say at x=5 m, δ would be about 7.71 cm.

Hucho and Sovran (1993) suggest that for a passenger car model affixed to a ground plane, the displacement thickness, δ^*, should be less than 10% of the model ground clearance, H, (in our case H is about 37 mm). The displacement thickness can be thought of as the amount by which an outer flow streamline is displaced due to the presence of the boundary layer. For turbulent

boundary layers, δ^* is approximately $(1/8)\delta$. The range of δ^*/H then would be much greater than the accepted value of 0.10, unless some means for controlling boundary layer growth is adopted.

Control of boundary layer thickness can be achieved by several methods. Conceptually, the simplest way to eliminate the unwanted boundary layer is to move the ground plane at the wind tunnel speed, U. Unfortunately, this scheme is mechanically complex and impractical for the long ground plane length required to test a platoon of vehicles. Our choice is to siphon off the boundary layer through a uniformly porous ground plane surface. This is a much simpler method to implement. Other possibilities, such as tangential blowing or single slot suction, are not viable because their effectiveness would not extend over the entire length of the ground plane.

The porous ground plane allows the possibility not only of removing the troublesome boundary layer flow, but of allowing additional unintended flow at the lower boundary. Thus it is not dynamically similar to a solid surface, as our later results will demonstrate. One must keep in mind that the objective of these experiments is to determine the change in the drag coefficient of a vehicle operating in a platoon compared to single vehicle operation. In both cases, the same ground plane is used, and ***the relative change*** will be less sensitive to the details of the ground plane boundary than the drag coefficients themselves.

Organization of the Manuscript The various sections of the manuscript are arranged as follows. **Section II** contains a detailed discussion of the Dryden wind tunnel and the performance of the ground plane. **Section III** is a discussion of the force balance design, including calibration procedures and results. **Section IV** lists pertinent data for the Lumina APV, and describes how the models are constructed. Finally, **Section V** contains the drag measurements on platoons of various lengths as well as additional discussion of these results. The **raw data** discussed **in Section V** is tabulated **in the Appendix.** Bottom-liners, who are interested only in the results and discussion, can turn directly to **Section V.**

II. Performance Characteristics of the Dryden Wind Tunnel and Suction Ground Plane System

Wind-Tunnel The tests to determine the aerodynamic forces on a platoon are conducted in the USC Dryden wind tunnel, This facility was built in the period between 1925-1935, and for many years was the best low-turbulence wind tunnel in the United States. It was donated to USC by the National Bureau of Standards in 1976. For this experiment, a large ground plane structure, incorporating a porous upper surface and a suction system, is installed. Before force measurements on the models are performed, a thorough survey of the flow in the tunnel is necessary. This includes investigations on the growth of the boundary layer on the ground plane, the turbulence level in the fieestream at frequencies of interest, the uniformity of the freestream velocity over a cross-sectional area of the test section, and the variations in static pressure, and therefore velocity, along the length of the test section for a variety of freestream velocities and under suction and no-suction conditions.

The Dryden wind-tunnel is a closed-return facility with a contraction ratio of 8:1 (see figure 1). The test section has an octagonal shape 1.37 m wide and 7.4 m long. The entire tunnel is constructed of tongue-and-groove siding reinforced by steel bands except for the contraction section which is sheet metal formed on wooden ribs. The downstream end of the test section is open to the room, which fixes the pressure at this point in the wind tunnel to be atmospheric. It also allows replacement of air lost due to minor leaks at other locations. The large, upstream settling section is equipped with ten turbulence-reduction screens used to reduce the freestream fluctuations. A DC-motor turns the 8-bladed, fixed pitch propeller that drives the flow. The DC-motor drive can be set to either low-speed or high-speed operation via a toggle switch on the power supply. Depending of the setting of this switch, the approximate maximum velocity attainable is either 26 m/sec. or 36 m/sec. respectively. Fine adjustments to velocity can be made using a multi-turn potentiometer on the operator control panel.

Ground Plane Construction The ground plane is installed in the test section as shown in figure 2. It is 5.8 meters long and 1.30 meters wide. It is actually a hollow, box-like structure of 10 cm height. The sides of the box are 10 cm x 10 cm x 0.95 cm aluminum angles, the legs of which are turned inward to support a 0.95 cm aluminum plate that makes up the bottom of the box. Square aluminum bar stock (2.5 cm) is attached to the top portion of the angles, and the entire box is supported on 2 T-shaped rails that attach to the tunnel walls (see detail, figure 2). In addition, the plate is supported from below by three airfoil shaped struts which extend the 42 cm to the bottom wall of the tunnel. The upper surface is constructed with interchangeable sections of perforated

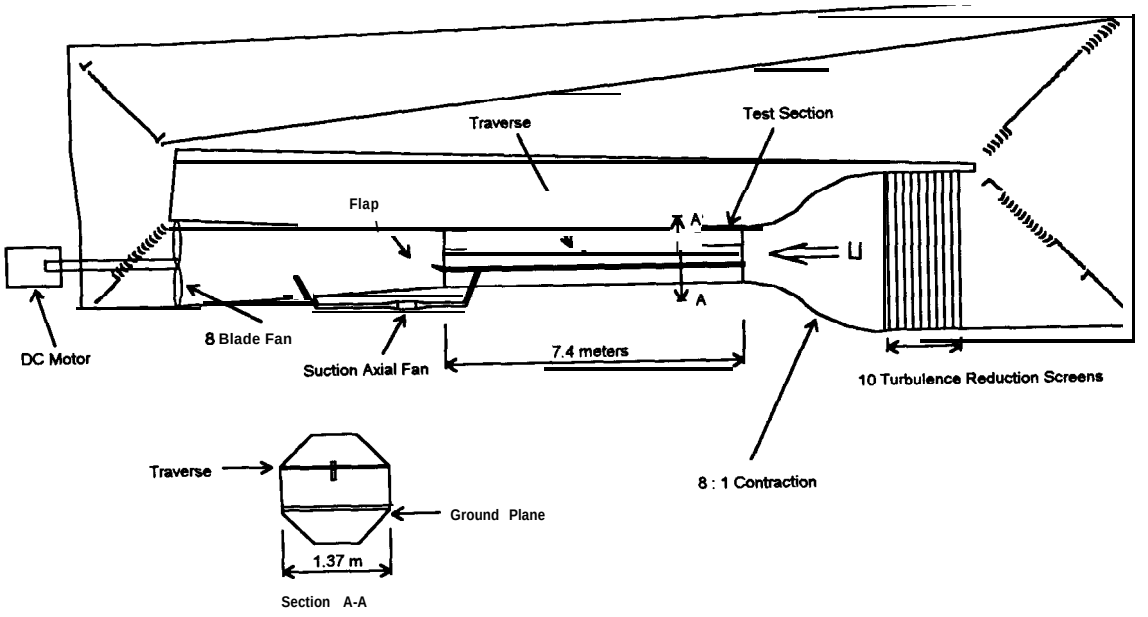

Figure 1. Schematic of the Dryden Wind-Tunnel

aluminum plates. By changing the configuration of the upper surface, the models can be tested at a 10” angle of yaw with respect to the freestream. The yaw is meant to simulate a crosswind.

The evenly distributed hole pattern in the porous upper surface is designed with 7% open area. The upper surface really consists of two aluminum plates spot-welded together, each having a different thickness and hole pattern. The thicker of the two plates is 4.8 mm in thickness and is uniformly perforated with 1.6 cm diameter holes on 2.06 cm centers. The uppermost plate is 0.8 mm in thickness and is also uniformly perforated with 1.0 mm diameter holes on 2.44 mm centers.

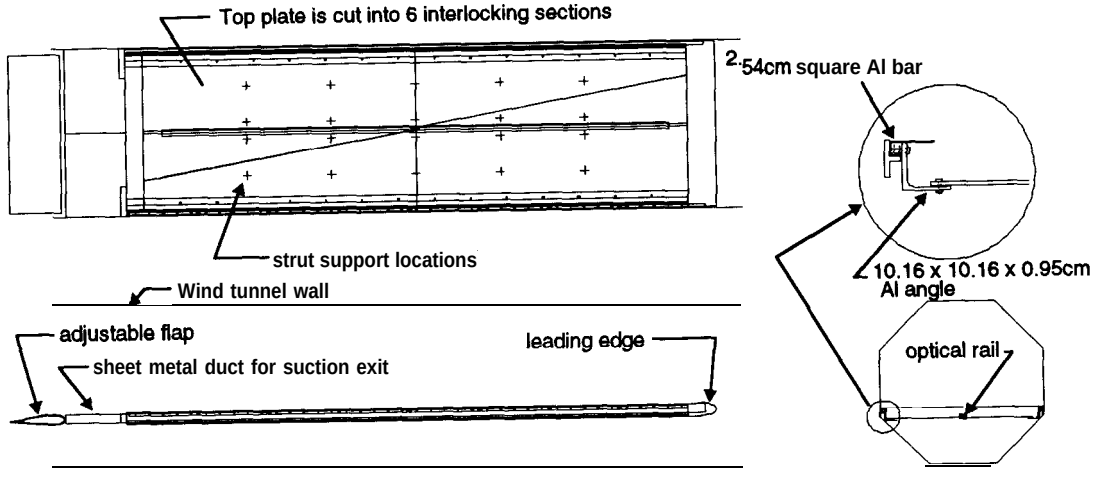

Figure 2. Ground Plane Structure in the wind-tunnel test section

The leading edge of the ground plane box is constructed of Styrofoam covered with refinished fiberglass having an elliptical shape of ratio 4: 1. The ellipse is attached to an inverted aluminum angle as shown in figure 3.

The downstream end of the ground plane box contains a sheet metal suction duct. The duct exits on both sides of the test section underneath the ground plane, and connects the plenum to two Joy@ AVR 90-75 D1298 axial fans that provide the necessary pressure drop to remove boundary layer air from the ground plane surface. The air is returned to the wind tunnel at the point of lowest pressure just forward of the propeller. The pressures across the two blowers are monitored on two vertical-column manometers. The pressure drop-volume flow characteristics for the fans can be found in the appendix.

A 1.2 m adjustable flap is connected to the back of the suction duct with a dowel type hinge. The flap can be positioned at different angles of incidence to modify the percentage of flow above and below the plate, as well as the static pressure gradient in the upper stream. A potentiometer is connected to the hinge mechanism and is used to set the flap angle to a predetermined position.

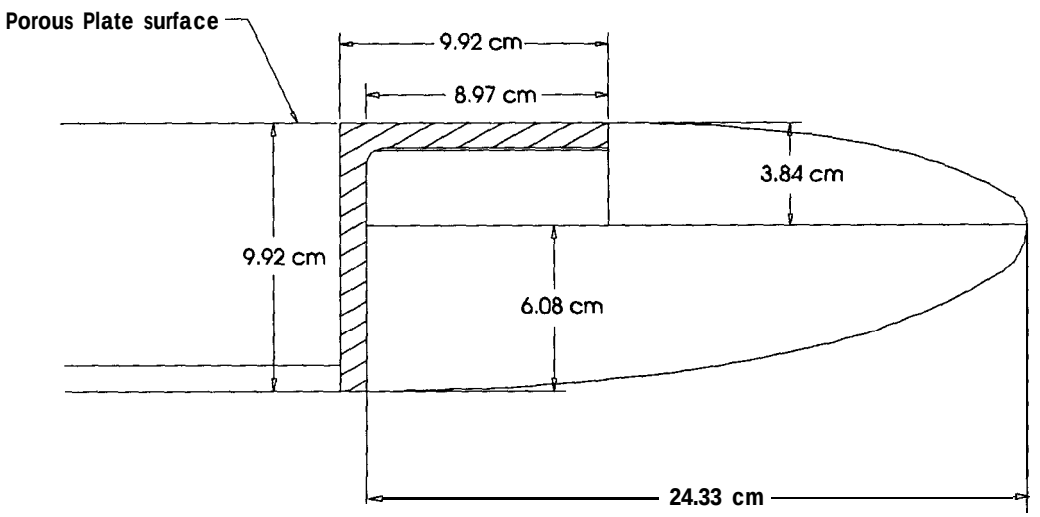

Figure 3. Detail of the Leading Edge of the Ground Plane Box

Instrumentation The interior of the ground plane is equipped with an optical rail secured to the center line of the bottom plate. It extends from 30 cm behind the leading edge to a downstream point about 10 cm forward of the end of the perforated upper plates – a distance of 4.27 meters. Four movable carriages slide along the optical rail, and are used to support the vehicle models above the porous surface. These carriages can be locked at any location along the optical rail. The box contains four electrical signal cables that connect the force sensors in the models to the external data acquisition system. It also contains four Pitot-static tube probes to measure static

and total pressure in the plenum interior. They are evenly spaced beginning 1 meter from the leading edge, in an alternating side-to-side pattern.

The wind-tunnel test section is equipped with a traverse mechanism which can be moved in three directions by means of stepper motors. Pitot tubes or hot-wire sensors are mounted on this traverse to measure local values of pressure or velocity at virtually any location in the test section. Two Pitot-static tube probes are fixed to the tunnel wall 86.4 cm from the leading edge of the ground plane, one above the ground plane, the other below. This arrangement is used to monitor the velocity, and the percentage of flow passing above and below the ground plane. A static pressure rail, approximately 5.80 meters in length and containing 38 static pressure taps at 15.2 cm spacings, is fixed along the center line of the tunnel ceiling. This is used to monitor the static pressure gradient in the tunnel during tests for later correction of data to include blockage effects. A thermocouple, fixed to the tunnel wall is used to monitor air temperature in the wind-tunnel.

All pressure measurements are made using either of two MKS® Baratron™ 310CD pressure sensors paired with a 270B signal conditioner/readout. This system has a nominal accuracy of about 0.1% of full scale (10 mmHg). This resolution is equivalent to ± 1 N/m^2, or about $\pm 10^{-5}$ atmospheres. Two Scanivalves'" are used to step from one pressure port to another. The uniformity of velocity in the test section is typically measured using Pitot-static tubes of 0.32 cm diameter. For the boundary layer, a Pitot tube with an outer diameter of approximately 1 mm is used. Hot-wire anemometers are also used in parallel with the pressure probes to measure freestream turbulence levels as well as boundary layer turbulence. The hot-wire sensing elements are typically platinum-rhodium alloys (10% rhodium) and solid platinum wires having diameters in the range 2.5-5 microns. The stronger 10% Rh material is used for the boundary layer measurements since these probes can survive an occasional brush with the wall. The boundary layer survey rake also includes a spring-loaded linear potentiometer. As the rake approaches the surface, the linear potentiometer stylus touches first, and gives an estimate of the surface position accurate to approximately ± 0.05 mm in the vertical direction.

Data Acquisition System All data is acquired using a Macintosh@ Quadra 950™. It is equipped with a National Instruments NB-MIO-16H-9 multifunction I/O board containing a 12-bit ADC ($\pm$ 10V max) with a maximum sampling rate of 100 Ksamples/sec. Digital I/O for moving the stepper motors and stepping the Scanivalves is provided by a NB-DIO-24 digital I/O board also installed in the Macintosh. Our custom data processing algorithms are written in the Labview® 2 format.

Setting Freestream Speed The reference freestream velocity, U_∞, is measured at the upper reference Pitot probe for a range of velocity settings. The fluctuation of U_∞ from its mean is observed for both high and low-speed settings and the results are shown in figure 4. The mean velocity presented here is an average taken over 100 records, each taken one second apart. Each record consists of 4096 data points taken 0.1 ms apart. Figure 4 shows the standard deviation, σ, from the mean velocity over the 100 seconds. It is expressed as a percentage of the corresponding mean velocity. In the low-speed setting, the useful range of wind tunnel speeds lies between 10 and 26 m/sec. where $\sigma < 0.2\%$. When the tunnel is operated at speeds less than 10 m/sec, the motor control circuit becomes unstable and large fluctuations in velocity are observed. We are presently attempting to modify the controller. In the high speed mode, the range over which $\sigma < 0.2\%$ is extended beyond 30 m/sec.

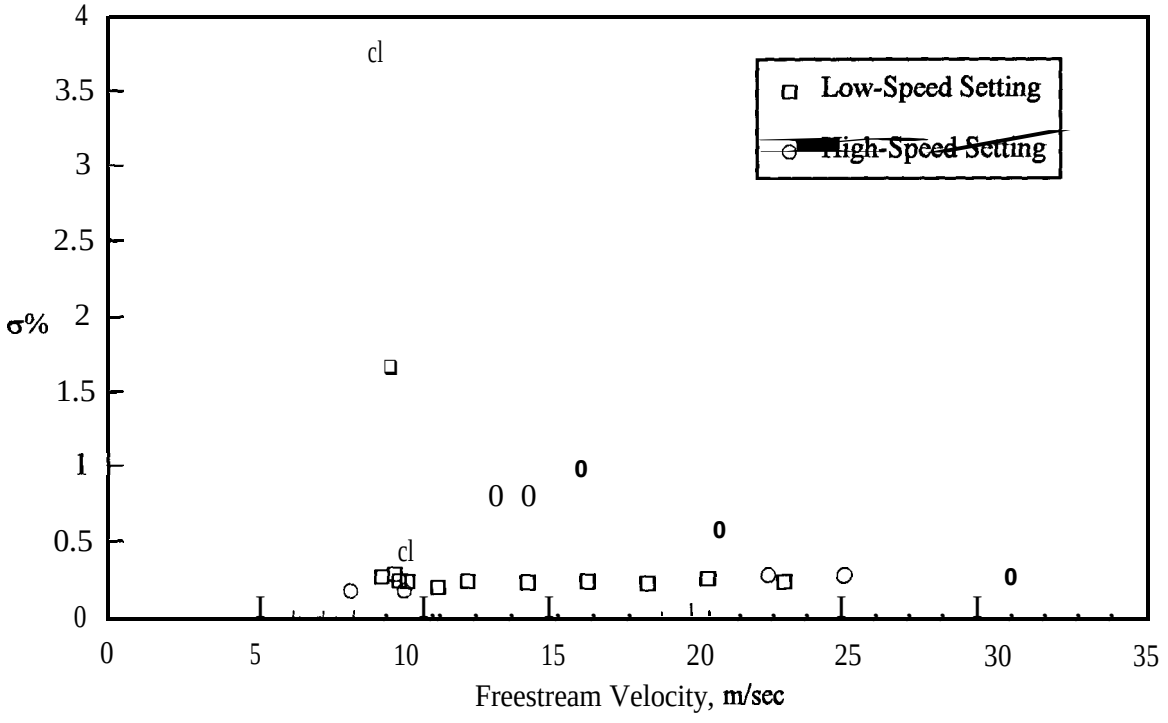

Figure 4. Velocity fluctuation levels at low and high-speed settings

The free stream turbulence level (i.e., the ratio of the r.m.s. value of the axial velocity fluctuation to the freestream speed, u'/U_∞) is measured at different locations using a constant-temperature hot-wire anemometer. The results are shown in figure 5. The abscissa, frequency, is actually the inverse of the averaging time. As frequency decreases (averaging time increases), more low frequency fluctuation is allowed to contribute to the variance. LeBlanc(1993), using the same facility without the ground plane and with an older motor controller, measured the free stream turbulence level with a constant-current hot-wire. His results showed $u'/U_\infty \cong 0.1\%$ for frequencies above 1 Hz (averaging time 1 second) at a speed of 25 m/sec. Figure 5 indicates a freestream

turbulence level that is slightly higher at this frequency. It seems to asymptote to a value of 0.1% as frequency increases. At lower frequencies, the turbulence level increases to about 0.25% at 0.02 Hz. It should be noted that, particularly at frequencies less than 0.2, the turbulence level increases with the **x,** the distance from the leading edge. All this seems to indicate a slight degradation in the flow quality due to the presence of the ground plane.

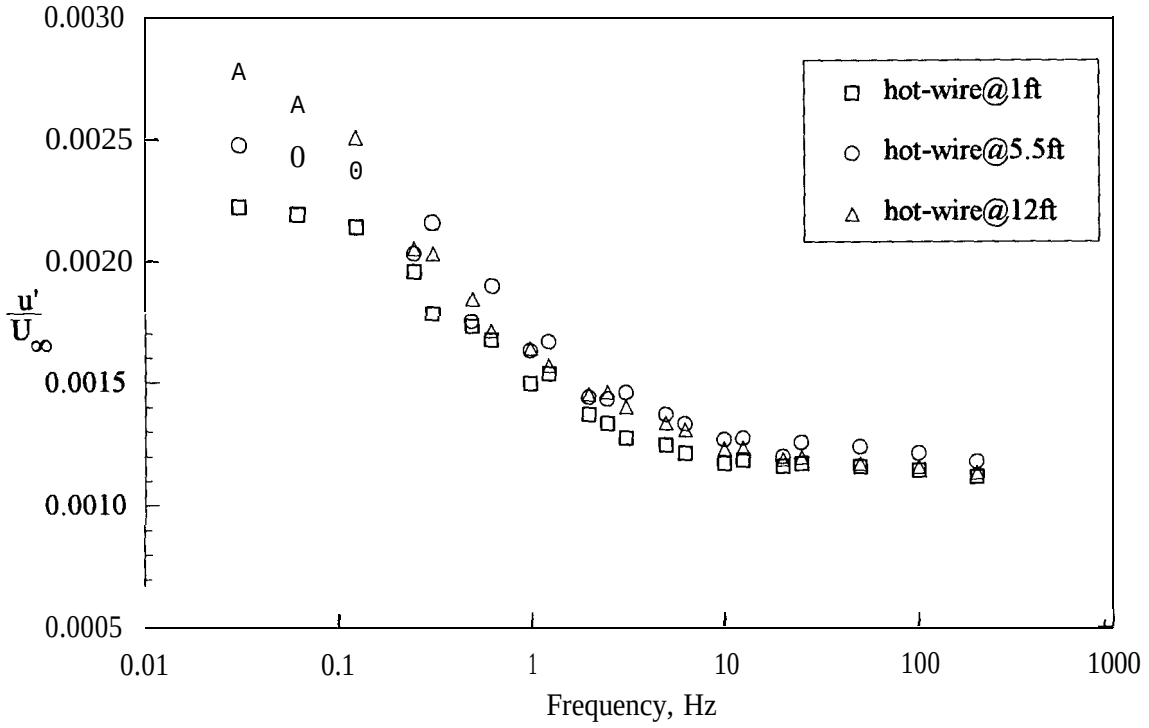

Figure 5. Freestream turbulence levels

The presence of this level of fluctuation raises a question as to what averaging time might be required to establish an accurate average value. To determine this time, the velocity is measured (with the reference Pitot-static tube) in intervals of 5 minutes, using data blocks of varying size and sampling time. The total number of blocks used for a particular set of data is the number needed to cover the entire 5 minutes. Figure 6 presents the results of this test. It shows that the standard deviation from the mean for a single data block increases as the total sampling time for the block increases. Also, it shows that the variation in the mean velocity between blocks decreases as the total sampling time for the block increases.

Figure 6 indicates that a minimum of about 8 seconds of sampling is required to achieve an acceptable data point that gives a relatively steady state average value $(u'/U_\infty < 0.15\%)$ as well as an accurate account of unsteadiness of the signal.

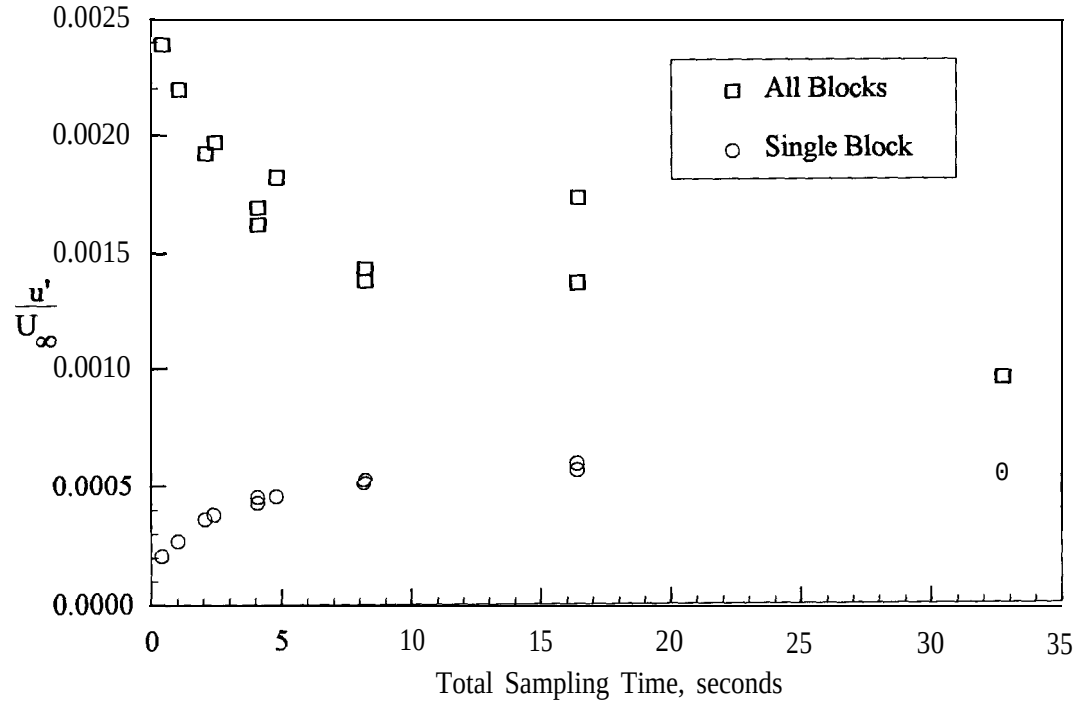

Figure 6. Effect of sampling time on averaged data

The effect of the flap angle, a, and suction on the unsteadiness is also examined using the reference Pitot-static probe. The results are shown in figure 7. A negative α corresponds to a higher blockage below the ground plane box. Suction is given as a percentage of the maximum control setting, corresponding to a volume flow rate of 0.87 m^3/sec (both fans combined). The behavior of u'/U_∞ as a function of a indicates that flow conditions are best when $a \cong 0°$. There is a slight increase in fluctuation level when the flap is rotated to the most negative position (-5°) and a more considerable increase for rotations to positive angles. It should be noted at this point that all measurements discussed in this report are made with the $a \cong 0°$, unless otherwise noted. Suction appears to have some effect on the unsteadiness at $a > 5°$, but the trend is not clear.

The division of flow above and below the ground plane is determined by the relative pressure losses. Both flap angle and suction affect the division, as shown in figure 8. Note that except for $\alpha > 10°$, the velocity above the plane is consistently higher than the velocity below the ground plane. This is likely due to the increased loss below the ground plane box caused by the box supports and the suction ducting. The ratio of U_{low}/U_∞, is in fact very close to unity and, considering the large change in flap angle, is rather insensitive to this variable. Suction causes the upper stream to capture a greater portion of the flow. The stagnation streamline moves toward the lower side, and the ratio U_{low}/U_∞ is decreased.

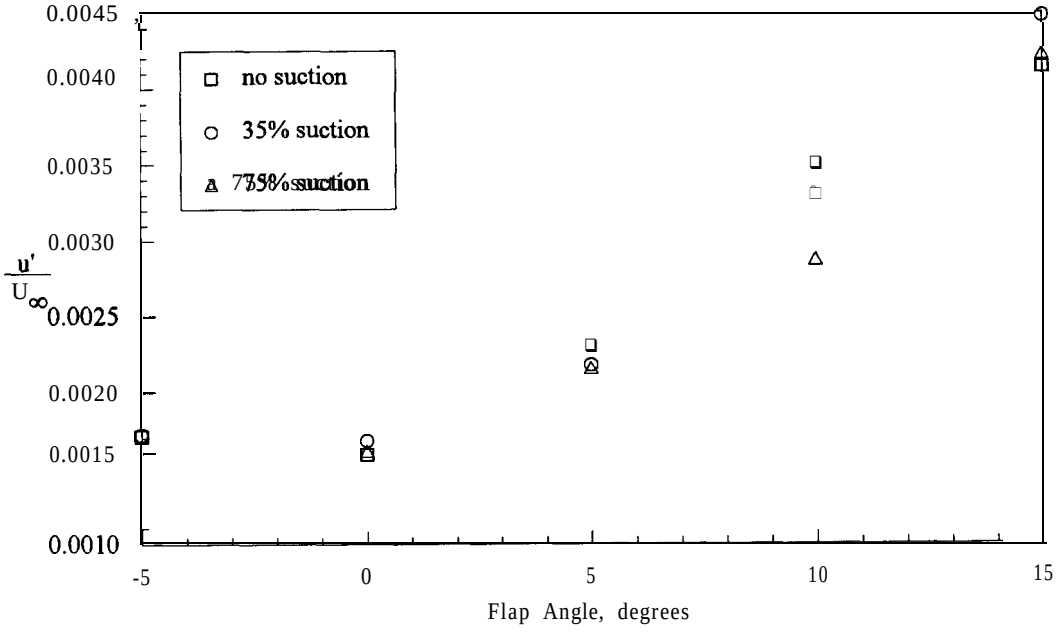

Figure 7. Unsteadiness effects of flap angle and suction

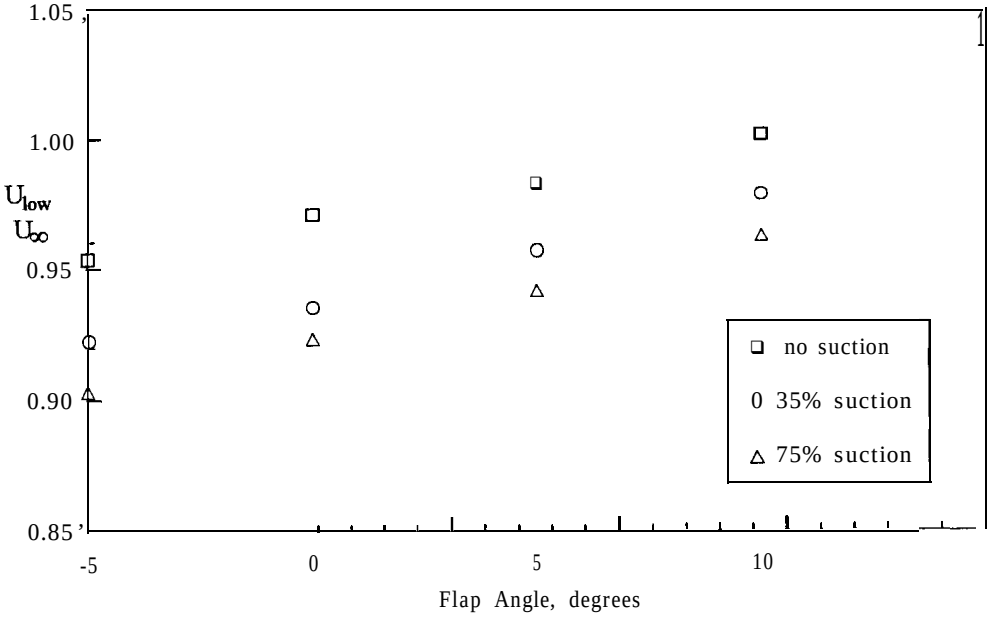

Figure 8. Stream Division as a function of flap angle and suction

Test-Section Pressure Gradient The freestream velocity is not constant throughout the length of the test section, but increases slowly in the downstream direction. This is because a boundary layer exists on the walls of the test section as well as on both sides of the ground plane. The boundary layer growth effectively reduces the cross-sectional area for the flow. This reduction in area causes the freestream flow to accelerate in the downstream direction. This behavior can be estimated by assuming a turbulent boundary layer which grows as described earlier. The effective diameter of the test section at every streamwise station then decreases by $2\delta^*$. The resulting approximation is shown in figure 9 along with velocities estimated from the static pressure measured along the wind tunnel ceiling. The flap angle in this case is 0" and no suction is applied. The estimated increase is calculated assuming turbulent boundary layer growth on the walls starting at the front of the test section (4.5 cm in front of the leading edge), and no boundary layer on the ground plane.

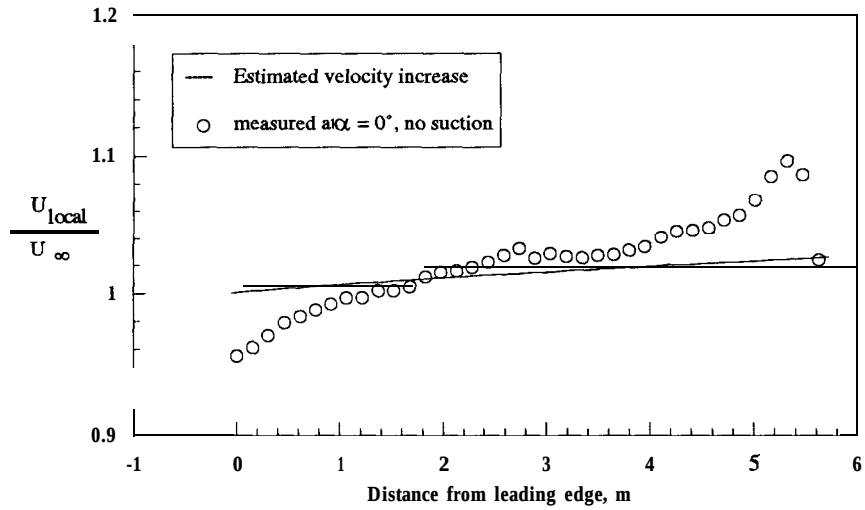

Figure 9. Velocity gradient along tunnel center line

The rapid increase in velocity at the front of the test section (O-l.0 meter) is due to flow acceleration around the leading edge of the ground plane box. The acceleration slows at about 1 m and, considering the crudity of the method used for estimation, behaves roughly as expected for the next four meters. Beyond 4.5 meters there is again increased growth. These local variations about a slightly accelerating flow are believed to be produced by redistributions of flow over the porous surface, and are best discussed in connection with the detailed ground plane boundary layer measurements.

Flap angle and suction level both influence the streamwise velocity gradient to some degree. In figure 10, the trend with increasing a is most noticeable beyond 2.8 meters. At large flap angles there is a region from (2.8 – 3.5) meters where the velocity may actually decrease with distance. This decrease is always followed by a rapid increase in velocity as the flow accelerates over the

upwardly deflected flap. At α=1 0 and particularly at α=15 degrees, the flow is much more unsteady. For this reason, such flap angles are probably outside the useful range of operation.

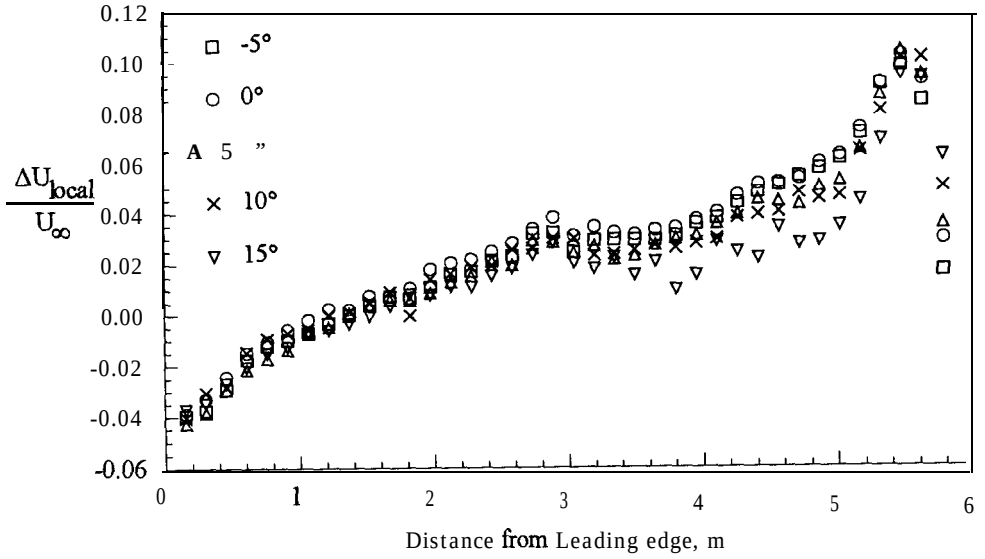

Figure 10. Effect of flap angle on streamwise velocity gradient with no suction.

Suction does not seem to affect the velocity gradient significantly over the first 2.8 meters of the test section, but downstream of this point the influence of suction is quite noticeable. In both the 35% and 75% suction cases, the velocity actually decreases between 2.8 and 5.0 meters. The decrease is a modest 0.14 m/sec/m at 35% suction, and about double that at 75% suction. The region downstream of 5 meters is still a region of flow acceleration. It becomes clear that the region of the test section beyond 5 meters should not be used since it is too near the flap (and possibly too near the wall gap) for uniform flow to be maintained.

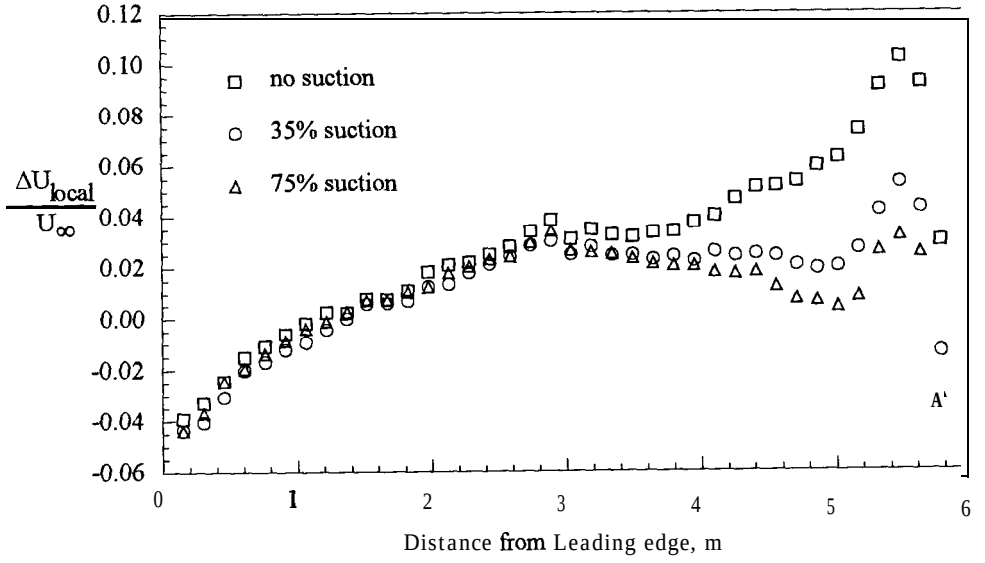

Figure 11. Effects of suction on velocity gradient with a = 0”

Flow Uniformity Flow uniformity in each cross section is determined by means of Pitot-static pressure surveys. Measurements of velocity are made on an 11 by 11 grid with uniform spacing of ***3.5*** cm in both y and z directions. The measurements covered approximately the central 15% of the cross sectional area. The survey is repeated at 12 streamwise (x) locations 30.5 cm apart between x=30.5 cm and x=366 cm. Figure 12 is a contour map of a typical distribution of velocity at one streamwise location. In figure 12, the average velocity is 23.85 m/sec.

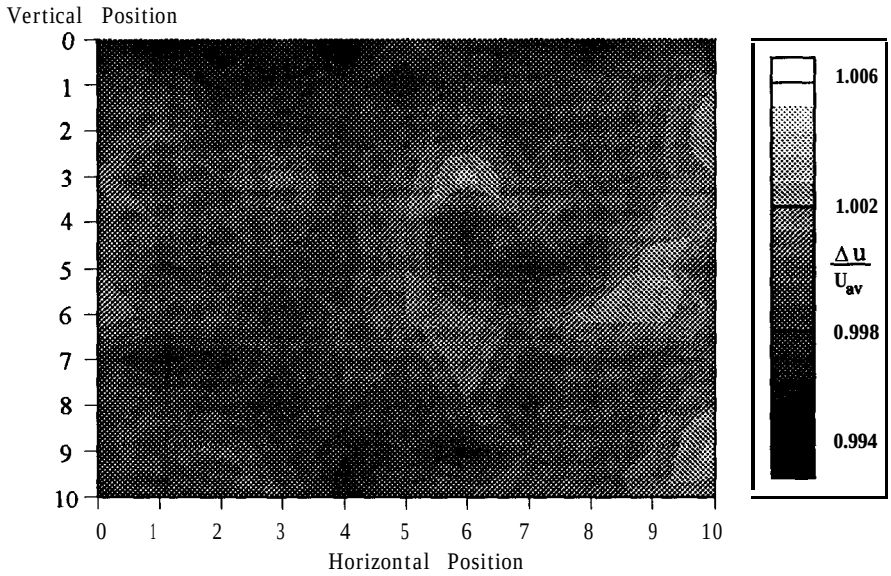

Figure 12. Contour map of typical velocity distribution over a cross-sectional area

Typically, the velocity at any point in a given cross-section deviates by no more than 0.5% from the mean velocity for that cross-section. The standard deviation from the mean is typically 0.15% over most of the test section, as illustrated in figure 13 (σ% represents the standard deviation of velocities in a cross section.). This was not quite true close to the leading edge of the ground plane at x=30.5 cm, where the local acceleration is higher.

Boundary Layer Surveys Velocity measurements are made in the boundary layer on the perforated surface with and without applied suction. In the suction case, 75% of the maximum control setting was used. (The maximum corresponds to a volume flow of 0.87 m^3/sec.) At a tunnel speed of 25 m/sec, this volume flow represents 2.6% of the flow rate through the wind tunnel cross section. Measurements are made with both a Pitot tube and a hot-wire probe. If the direction of the flow close to the plate deviates significantly from that of the freestream, the total pressure measured by the Pitot tube may be in error. The error would be minimal for a hot-wire probe.

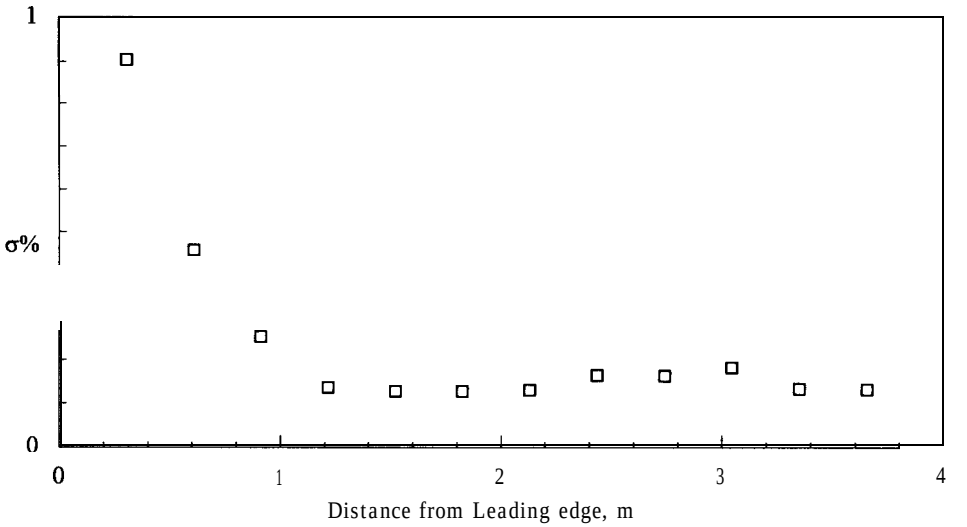

Figure 13. Variation in flow uniformity over a cross-sectional area

Initial measurements indicate that the two methods are essentially identical. In figure 14, note scale changes on the horizontal axis. The bulk of the measurements are made using only the Pitot probe since it provides sufficient resolution and eliminates the need for time consuming calibrations and extra care in handling. Velocity profile measurements are made at 14 streamwise stations at 30.5 cm spacing starting from the leading edge, and 6 spanwise locations at z = 0, ±15.24, ±30.48, ±45.72 cm from the centerline.

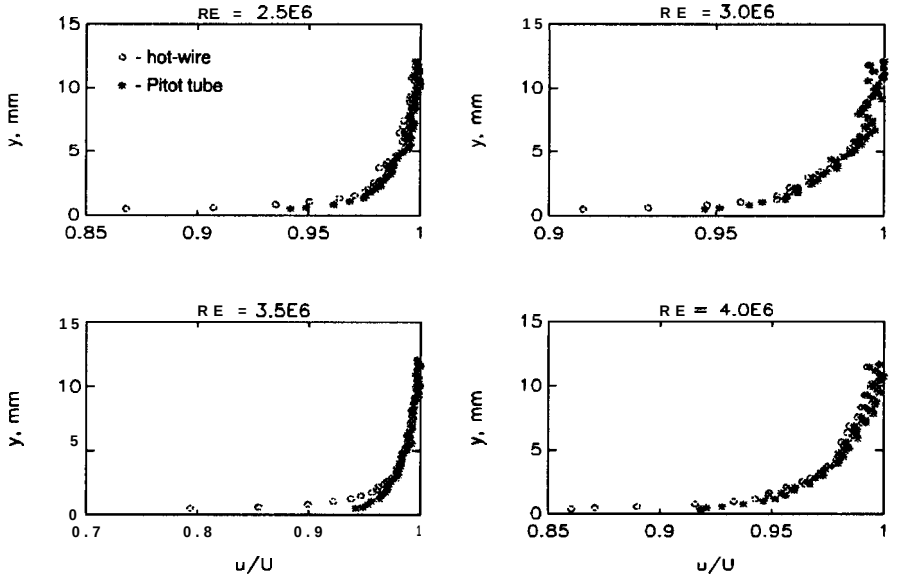

Figure 14. Comparison of velocity profiles using Pitot tube and hot-wire probes

The displacement thickness is estimated by integrating the measured velocity profiles based on the definition

$$\delta^* = \int_{y=0}^{U_\infty} \left(1 - \frac{u(y)}{U_\infty}\right) dy$$

Figure 15 shows the variation in δ^* along the ground plane without suction. Z1-Z6 represent the spanwise stations in use. Z4 is along the centerline of the ground plane. Consider the other five spanwise stations first. One is immediately struck by the uniformity and thinness of the boundary layer displacement thickness over most of the surface. Indeed it is so thin that our Pitot instrumentation can scarcely resolve it accurately. Only downstream of x=3 meters does the boundary layer begin to grow substantially. We believe the explanation for this surprising behavior is connected with the porous surface and the slightly favorable pressure gradient due to wall boundary layer growth. The favorable pressure gradient is imposed upon the ground plane boundary layer and upon the porous boundary itself *Thus flow wifhin* the ground plane plenum also proceeds from regions of high pressure to regions of low pressure-that is, from upstream to downstream. To satisfy continuity of flow, air must flow *info* the plenum over the forward portions of the plate-thus maintaining a relatively thin boundary layer. When no suction is applied, there can be no net flow into the ground plane plenum. (In this configuration, the suction duct outlets are sealed.) The *flow info* the plenum over the forward 3 meters of the ground plane becomes an ***outflow*** in the region downstream of x=3 meters. This is the explanation for the dramatic thickening of the boundary layer illustrated in figure 15. The application of active suction is needed to remove only the accumulated volume flow at the rear of the plenum.

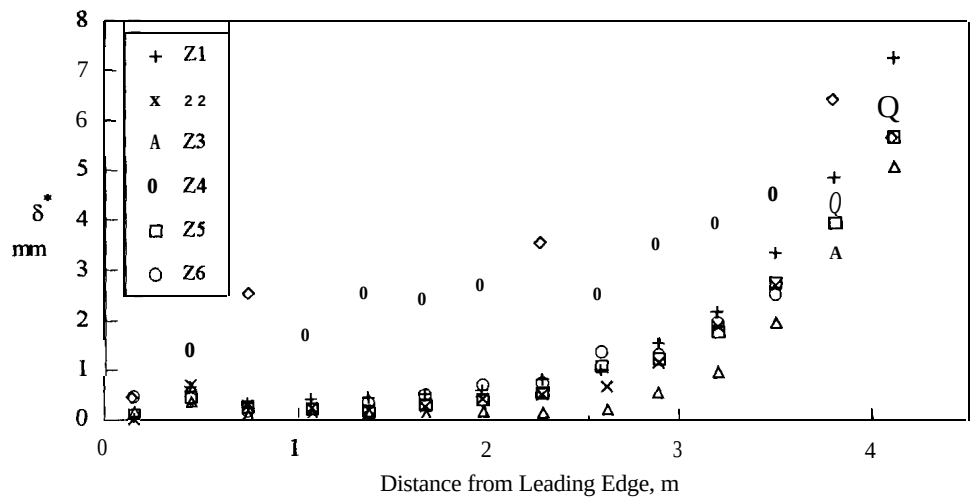

Figure 15. Boundary layer displacement thickness on ground plane without suction

Figure 16 shows how suction affects δ^*. As expected, fluid is removed from the rear of the plenum preventing the blowing that occurs when suction is not applied. The suction is successful in keeping δ^* at a nominal value of less than 1 mm over the entire working length of the ground plane.

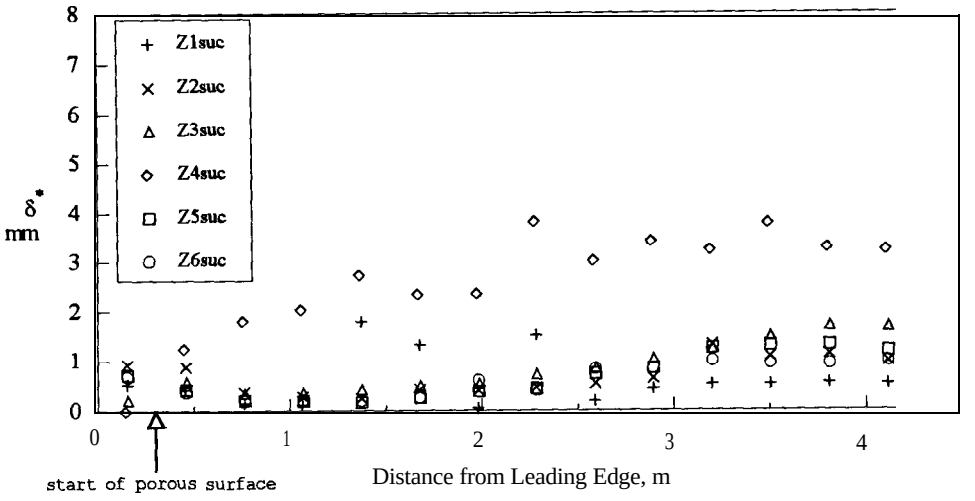

Figure 16. Boundary layer displacement thickness on ground plane with 75% suction

In both figures 15 and 16, the boundary layer thicknesses at the spanwise position Z4, along the centerline of the plane, are greater than at surrounding points. The larger values are due to the impermeability of the covers that are placed over the center slot of the ground plane. In spite of this, δ^* stays below 4 mm over the entire working length of the ground plane. In the worst case, this would represent a δ^*/H value of 10% which is acceptable (recall that H is model-to-ground plane clearance, 37 mm).

III. Design and Performance Evaluation of the Three-Component Force Balance

Force Balance Geometry The force balance used for the tests described here is designed specifically to measure drag, side force and yawing moment on a series of vehicles in tandem undergoing wind-tunnel tests. The design minimizes the sensitivity of the sensor to lift, and pitch and roll moments, which are not measured, as well as minimizing crosstalk between drag and side force. Two possibilities exist for the placement of strain elements – one scheme utilizes the model support posts which protrude through the ground plane, the other possibility requires construction of a self-contained balance which will fit within the model. We choose the latter. Internal mounting of the balance actually simplifies the design and reduces the number of strain gauges required to resolve the three components needed. It also allows greater flexibility of model position when platoon misalignments are studied. Figure 17 is a planform view of the sensor showing the attachment locations of the strain gauges and the sign convention used for calibration. The long-side arms attach to a plate that is fixed to the vehicle model. The shorter arms at the top and bottom attach to a plate that is fixed to the posts supporting the model above the ground plane. The entire assembly resembles a "sandwich" with the cruciform containing the flexures as the middle layer.

The particular design of flexures follows Ono & Hatamura (1986). They are termed parallel-plate-structures or PPS – all of the deformation takes place at the flexure location in a manner which resembles the deformation of two parallel plates (as in figure 18(b)). Each flexure is designed to yield approximately 1 mV output per Volt of excitation at a nominal total load of nine Newtons. Each of the four Wheatstone bridges contains four strain gages for maximum sensitivity. Bridges A and D are sensitive to side force and yaw moment, and bridges B and C are sensitive to drag and yaw moment.

Ono & Hatamura(1986) showed that a sensor based on a PPS has a much lower total deflection for the same strain at the gage location than a sensor based upon a uniform beam. Figures 18(a) and (b) show a comparison of these two cases.

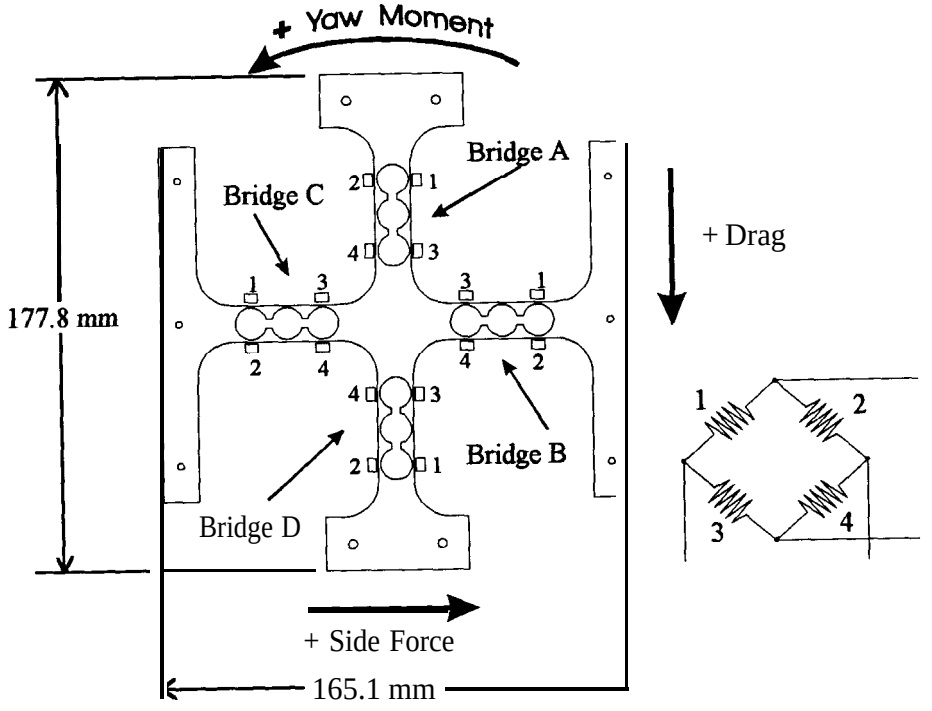

Figure 17. Planform of 3-component force balance showing strain gauge placement and force sign convention. Overall thickness is 12.7 mm.

For the uniformly deformed beam, the end deflection is

$$\delta = \frac{F L^3}{3 E I} \qquad (1)$$

where the moment of inertia is

$$I = \frac{b t^3}{12}. \qquad (2)$$

The strain at the gage location is

$$\varepsilon = \frac{F x y}{E I} \qquad (3)$$

where y = distance from neutral axis.

Thus,

$$\varepsilon_1 = \frac{6 F x}{E b t^2} \qquad (4)$$

and

$$\delta_1 = \frac{4 F L^3}{E b t^3} \qquad (5)$$

For the PPS, the only strain occurs across the cut-out portion of the beam. The upper and lower plates can be taken as separate beams, each carrying half the load. Therefore the moment of inertia, I, for the PPS is

$$I = \frac{b' t'^3}{12} \qquad (6)$$

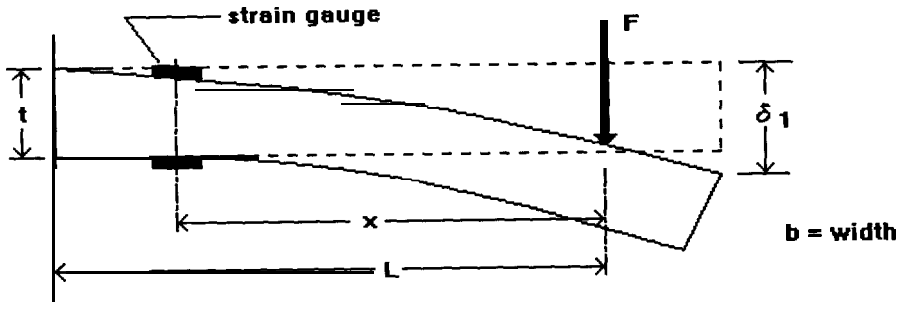

(a) Uniformly Deformed Beam

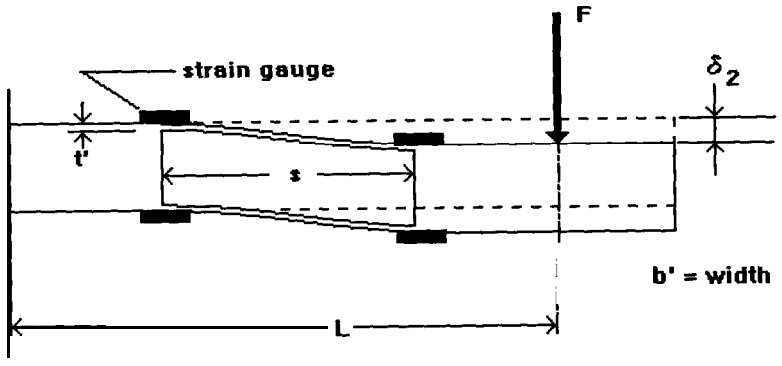

(b) Parallel Plate Structure (PPS)

Figure 18. Comparison of a uniform cantilever beam with a Parallel Plate Structure

Furthermore, one sees that either the upper or lower plate can be thought of as 2 beams cantilevered at each end and joined at the center. The effective length of each half-beam is just s/2, the force on each plate is F/2, and y = t'/2. One can use equation 1 to find the half-displacement $\delta_2/2$.

The resulting equations for strain and displacement for the PPS are then:

$$\varepsilon_2 = \frac{3\,F\,s}{2\,E\,b'\,t'^2} \qquad (7) \qquad \text{and} \qquad \delta_2 = \frac{F\,s^3}{2\,E\,b'\,t'^3} \qquad (8)$$

Fixing $\varepsilon_1 = \varepsilon_2$ gives the following expression for the ratio of deflections.

$$\frac{\delta_1}{\delta_2} = \frac{1}{8}\left(\frac{t}{t'}\right)^3 = O\left(10 - 10^2\right) \qquad (9)$$

It is also important to notice that neither the strain nor the displacement are dependent on the location of the point of application of the force to be measured. In this approximation, the response of a PPS flexure to an applied force is exclusively determined by the flexure geometry.

Design Strain Estimates The problem of machining a precise rectangular cut-out such as is needed for a PPS type flexure is circumvented by replacing it with a hole-and-slot configuration. Ochiai, et al.(1986) describe this method as used on a robot arm. Figure 19 shows the details of a typical flexure used for the sensor. The peak strains experienced by this flexure in bending align with the centers of the two end holes. This is where the strain gauges are located. The material used is 7075-T6 aluminum which has a nominal modulus of elasticity, E = 73 GPa.

The dimensions of the flexure are limited by the tolerance that can be achieved in machining. For a reasonable tolerance of ±0.25 mm, a minimum thickness for t' is deemed to be t' = 6.0 mm. This represents an uncertainty of about 8% in the thickness of the gauged location, and is felt to be the maximum tolerable. The overall size of the force balance has little or no effect on the strain levels at the flexures. The size was determined by the mounting requirements for the particular models chosen.

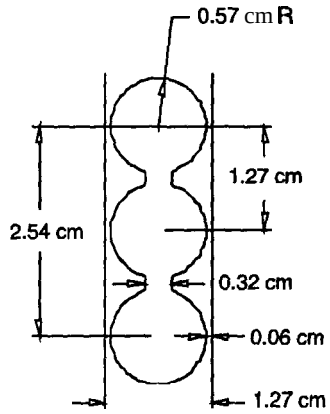

Figure 19. Detail of PPS type flexure

The drag coefficient, C_D, for a full-scale vehicle is reported by General Motors to be 0.32. The frontal area is approximately 2.8 m². Since the models used in this study are 1/8th scale, the frontal area, A, of the model is about 0.044 m². The maximum velocity in the Dryden wind tunnel, U_∞, is about 30 m/s. At this velocity, the drag on a single model would be

$$D = C_D A\left(\tfrac{1}{2}\rho U_\infty^2\right) \approx 8N$$

The force, F, on each flexure sensing drag would be about half of this due to symmetry. The resulting strain then at one portion of the flexure is

$$\varepsilon = \frac{3(4N)(0.0254m)}{2(73\times10^9 Pa)(0.0127m)(0.000635m)^2} \approx 400\mu\varepsilon$$

The expected displacement due to this force is

$$\delta = \frac{(4N)(0.0254m)^3}{2(73 \times 10^9 Pa)(0.0127m)(0.000635m)^3} \approx 0.00014m$$

For a nominal gauge factor, G = 2, and excitation voltage $e_i = 5V$, one can estimate the primary gauge output, Ae, to be

$$\Delta e \approx e_i G\varepsilon \approx 4mV$$

So approximately, the sensitivity of the flexure is 1 mV/V of excitation.

Calibration Method The balances are mounted on a calibration platform as shown in figure 20. Known forces are applied to the balance by means of weights and pulleys. The pulleys to the right and rear of the model are fixed and provide a constant side force and drag. The pulley to the left of the model is mounted on a traversing mechanism and can be translated ±10 cm from the centerline of the balance. This provides a range of drag, side force and yaw moment values for each loading condition, as summarized below:

$$\text{Drag} = W_2 - W_1 \sin\theta$$

$$\text{Side Force} = W_3 - W_1 \cos\theta$$

$$\text{Yaw Moment} = -W_1 L \sin\theta$$

L is the distance from the center of gravity of the balance to the point of application on the yoke (the moment arm) and θ is the angle between the centerline to the line of application.

Validyne SG-297 circuit cards in an MC-170 chassis provide both the excitation voltage and adjustable amplification (0.3-3X) for the bridge outputs. They also provide adjustable, low-pass filtering.

The calibration sequence is as follows. All four bridges on the force sensor are first zeroed so that their output is 0 ± 5 mV with no loads applied. Each of the pulleys is then aligned with the electronic centerline of the balance. This is accomplished by loading the balance in one direction, (drag first), and adjusting the pulley location until the output of the two bridges sensitive to side force (A and D) have outputs of 0 ± 5 mV. The gain of both bridges sensitive to drag (B and C) are then adjusted to have outputs of 8V ± 5 mV when a nominal drag load of 9.81N is applied. In practice, some iteration is required between balancing the bridges with no load and setting the gain as described. The same procedure is followed in the application of a pure side force using the pulley attached to the stepper motor drive. Finally, a load is applied to the fixed-side pulley and its

location adjusted until the drag sensitive bridges read 0 ± 5 mV. (The gains of the two side-force sensitive bridges need no further adjustment.)

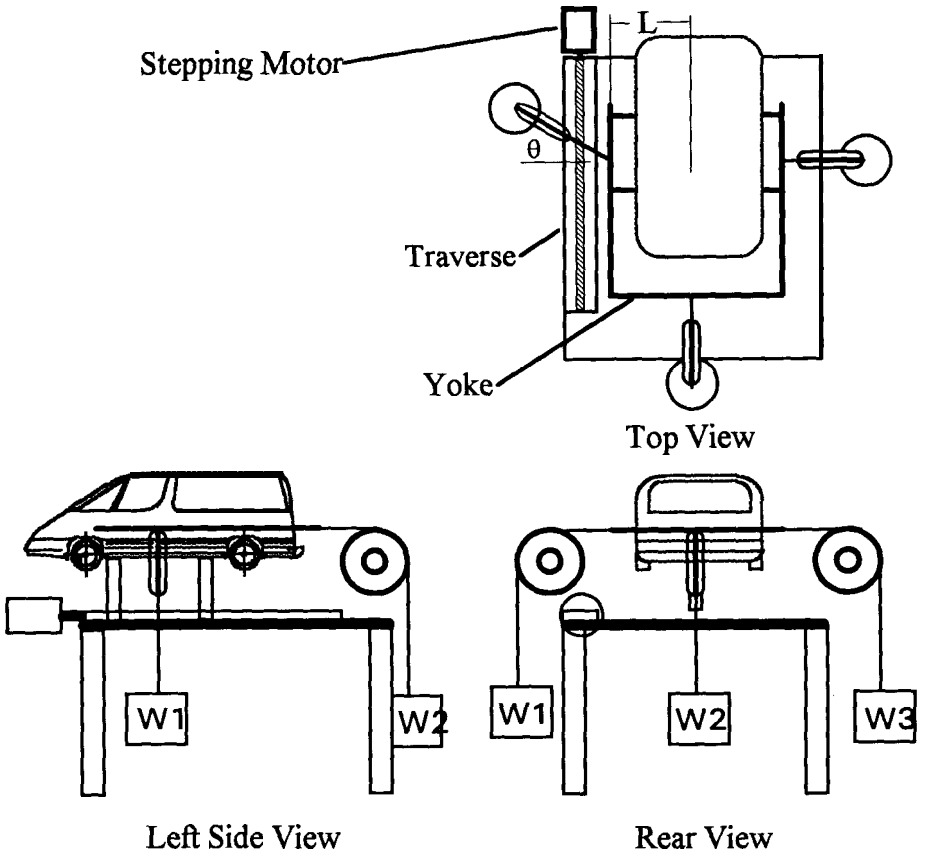

Figure 20. Three View of the Calibration Platform

Data acquisition is performed using a Macintosh IIfx personal computer equipped with a National Instruments@ NB-DIO-16L-9 multifunction I/O board and a Labview® 2 user interface. The computer can record the voltage outputs from the force sensor at a resolution of about 5 mV (one bit). The computer also controls the stepper motor driving the side-force traversing mechanism. The Labview® program prompts the user to apply a predetermined loading condition (W1,W2,W3), and actuates the traverse. At each specified location (now six in all), a two-second average (1024 points @ 500 Hz) of each of the 4 output voltages are recorded and stored in a data file. This is done for a total of four loading conditions. Two zero-load data points are recorded at the start and end of each calibration run, giving a total of 26 data points. At the end of each calibration, the program computes the matrix of influence coefficients as described in the next section. It also provides the user with error estimates for the calibration.

Determining Calibration Coefficients The output voltages from the four bridges, V_A, V_B, V_C and V_D, are combined in the following manner:

$$V_{Drag} = V_B + V_C$$

$$V_{Side} = V_A + V_D$$

$$V_{Yaw} = (V_C - V_B) + (V_A - V_D)$$

During calibration, combinations of Drag, Side Force and Yaw Moment are applied and the resulting voltages are recorded. Assume the following linear system of equations:

$$V_{Drag} = A_{11}Drag + A_{12}Side + A_{13}Yaw + A_{14}$$

$$V_{Side} = A_{21}Drag + A_{22}Side + A_{23}Yaw + A_{24}$$

$$V_{Yaw} = A_{31}Drag + A_{32}Side + A_{33}Yaw + A34$$

Calibration data can be fitted in a least-squares sense to find the matrix of coefficients $A = [A_{ij}]$. The elements A_{14}, A_{24}, and A34 are voltage offsets. These must be subtracted from the voltages read during testing to yield

$$V'_{Drag} = V_{Drag} - A14$$

$$V'_{Side} = V_{Side} - A24$$

$$V'_{Yaw} = V_{Yaw} - A34$$

The remaining 3 X 3 matrix can then be inverted to yield B = inv(A) and Drag, Side Force and Yaw Moment can be estimated from:

$$Drag = B_{11}V'_{Drag} + B_{12}V'_{Side} + B_{13}V'_{Yaw}$$

$$Side\ Force = B_{21}V'_{Drag} + B_{22}V'_{Side} + B_{23}V'_{Yaw}$$

$$Yaw\ Moment = B_{31}V'_{Drag} + B_{32}V'_{Side} + B_{33}V'_{Yaw}$$

Alternatively, one can assume the linear relations:

$$Drag = C_{11}V_{Drag} + C_{12}V_{Side} + C_{13}V_{Yaw} + C_{14}$$

$$Side\ Force = C_{21}V_{Drag} + C_{22}V_{Side} + C_{23}V_{Yaw} + C_{24}$$

$$Yaw\ Moment = C_{31}V_{Drag} + C_{32}V_{Side} + C_{33}V_{Yaw} + C_{34}$$

and solve for the matrix C directly, thus avoiding possible truncation errors in the inversion process.

The matter of fitting voltage on force and inverting the result or fitting force on voltage and using the result directly warrants closer examination. It is clear that physically, voltage is the dependent variable. (It is a change in force that causes voltage to change rather than vice-versa). However, in fitting one variable to the other, one must also consider which of these variable is to be predicted by knowing the other. Buhner(1979) states that one must use the regression of force on voltage rather than vice versa if voltage will be used to predict force. As it turns out, use of one method or the other is not so critical when the relationship under examination is approximately linear and relatively noise free. Both methods show no difference whatsoever when artificial (no noise) data is used. When processing actual data from a calibration, a comparison of the two methods shows that the method involving a matrix inversion predicts loads whose percentage error is higher, by less than 0.01%, than those predicted by the direct method. The method used in these tests for finding the matrix of calibration coefficients is the more direct method of fitting force on voltage. The decision to use this method is based solely on the simplicity of the procedure since, as described above, the results from both methods are almost identical.

Assuming the relations described previously, one must solve for the matrix of coefficients, C,

$$\vec{C} \times \vec{V} = \vec{F}$$

where

$$\vec{C} = \begin{bmatrix} C_{11} & C_{12} & C_{13} & C_{14} \\ C_{21} & C_{22} & C_{23} & C_{24} \\ C_{31} & C_{32} & C_{33} & C_{34} \end{bmatrix}, \quad \vec{V} = \begin{bmatrix} V_{Drag} \\ V_{Side} \\ V_{Yaw} \\ 1 \end{bmatrix}, \quad \vec{F} = \begin{bmatrix} Drag \\ Side\ Force \\ Yaw \end{bmatrix}$$

Using the method of least squares, one can derive the following relationship.

$$\begin{bmatrix} \sum V_{Drag}^2 & \sum V_{Drag} * V_{Side} & \sum V_{Drag} * V_{Yaw} & \sum V_{Drag} \\ \sum V_{Drag} * V_{Side} & \sum V_{Side}^2 & \sum V_{Side} * V_{Yaw} & \sum V_{Side} \\ \sum V_{Drag} * V_{Yaw} & \sum V_{Side} * V_{Yaw} & \sum V_{Yaw}^2 & \sum V_{Yaw} \\ \sum V_{Drag} & \sum V_{Side} & \sum V_{Yaw} & N \end{bmatrix} \times \begin{bmatrix} C_{11} \\ C_{12} \\ C_{13} \\ C_{14} \end{bmatrix} = \begin{bmatrix} \sum Drag * V_{Drag} \\ \sum Drag * V_{Side} \\ \sum Drag * V_{Yaw} \\ \sum Drag \end{bmatrix}$$

Similarly, by substituting Side Force for Drag, one can find C_{21}, C_{22}, C_{23}, and C_{24}. Also, using Yaw, C_{31}, C_{32}, C33, and C34 can be determined.

Calibration Results *The voltages,* V_{Drag}, V_{Side} and V_{Yaw} measured during a typical calibration are shown in figure 21 as functions of drag, side force and yawing moment respectively. Note that in each of these plots, the balance is being acted upon by some combination the three components, not just the single force or moment displayed in the plot. The linear fits attest to the fact that all of the chosen combinations of output voltages to form V_{Drag}, V_{Side} and V_{Yaw} are relatively free of crosstalk from the other force/moment components; they indicate a well-designed force balance.

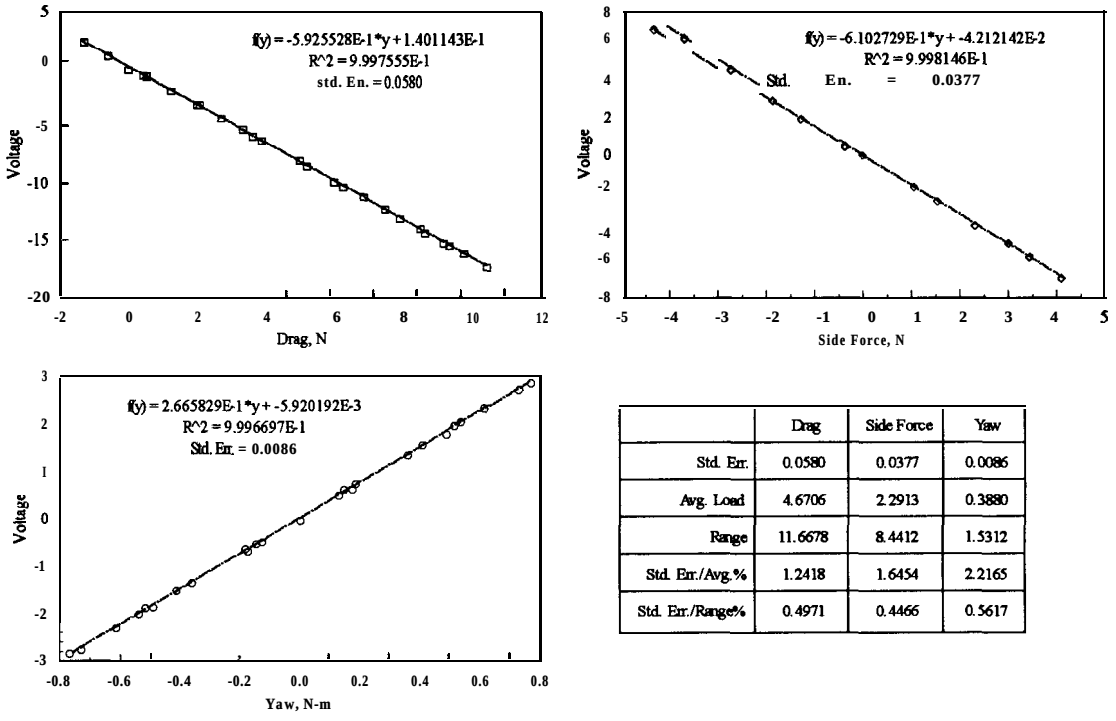

	Drag	Side Force	Yaw
Std. Err.	0.0580	0.0377	0.0086
Avg. Load	4.6706	2.2913	0.3880
Range	11.6678	8.4412	1.5312
Std. Err./Avg.%	1.2418	1.6454	2.2165
Std. Err./Range%	0.4971	0.4466	0.5617

Figure 2 1. Dependence of Individual Voltage Components on Corresponding Force Components

This same orthogonality can be seen in the matrix of calibration coefficients that results from a typical calibration as presented in figure 22, which also contains plots of the predicted loads vs. the applied loads for drag, side force and yawing moment. (The predicted loads are found by multiplying the voltages that result from the loads applied during calibration with the coefficient matrix. If the predictions were exact, all the data points would lie on the diagonal line.) The off diagonal elements of the matrix are typically two orders of magnitude smaller than the terms which lie along the diagonal and account for the bulk of the sensitivity. The standard errors, average loads during calibration, and percentage errors-defined as standard error/average load-are also shown.

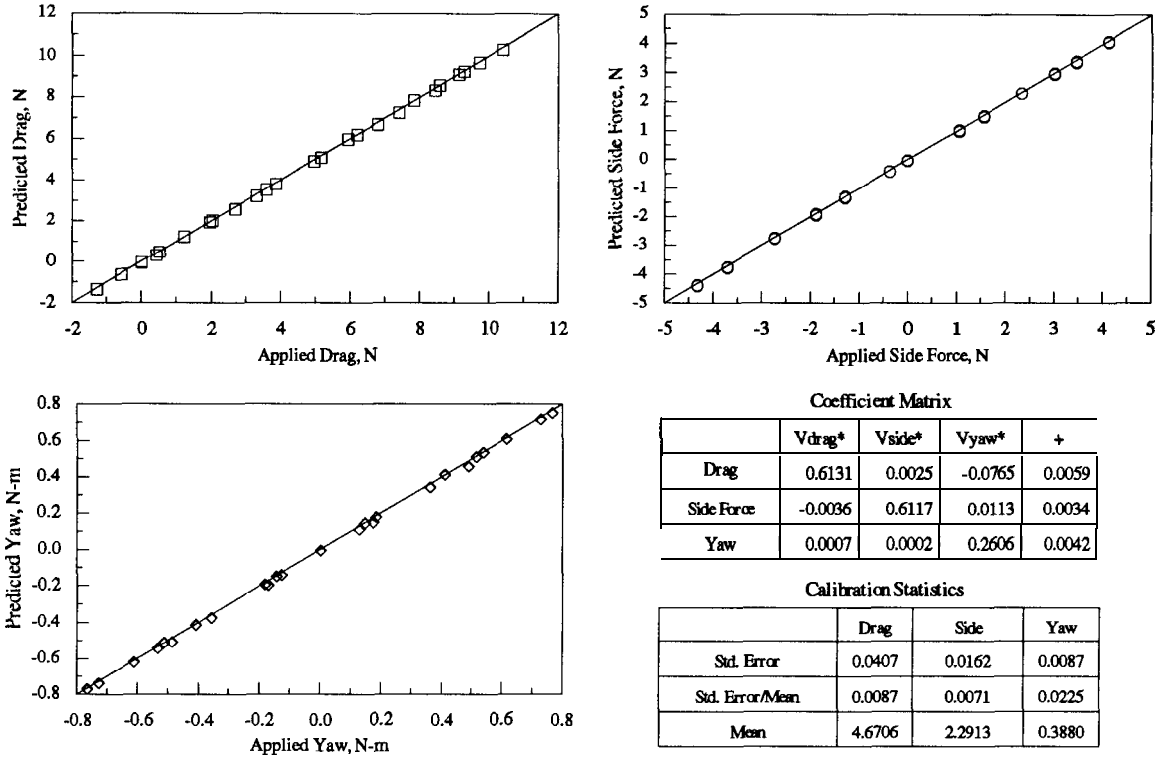

Coefficient Matrix

	Vdrag*	Vside*	Vyaw*	+
Drag	0.6131	0.0025	-0.0765	0.0059
Side Force	-0.0036	0.6117	0.0113	0.0034
Yaw	0.0007	0.0002	0.2606	0.0042

Calibration Statistics

	Drag	Side	Yaw
Std. Error	0.0407	0.0162	0.0087
Std. Error/Mean	0.0087	0.0071	0.0225
Mean	4.6706	2.2913	0.3880

Figure 22. Results from a Typical Calibration

Error based on average load is probably more representative of actual errors, but it is more common to present error as a fraction of full scale range. Using this standard, the estimated errors in drag, side force and yawing moment readings from the force balance are approximately 0.35%, 0.20% and 0.54% respectively. The force balances are left on the calibration table for several days to check for drift in the circuitry. Within that period, the zero-load voltages change by only l-2 mV, which is insignificant since the ADC resolution is ±5 mV.

When the model is transferred from the calibration table to the wind-tunnel, the output voltages at zero load do not remain at zero. The change is approximately 0.1 – 0.3 Volts. Because the forces necessary to produce these output voltages are so small, it is difficult to pinpoint the exact cause for this behavior. There are probably several contributing factors. First, the model is never perfectly level in the wind tunnel, and model weight causes the balance to sense a spurious force. The magnitude of the force corresponding to a 0.3V output is about 0.2N (or 0.04 lb). Since the model weighs about 37 N, the departure from the vertical need only be about 0.30'. Another source for the offset voltage is the slight difference in the mounting hardware between the wind tunnel and the calibration table. The zero-load voltages are recorded after the model is mounted securely in the wind-tunnel, and these voltages are subtracted to establish a new zero-load condition. An alternative method of accounting for this change in zero-load output is to adjust the

balancing potentiometers on the SG297 amplifier cards. In either case, the gains are not affected, and the linear prediction scheme is still valid.

Figure 23 gives an idea of how much the calibration coefficients, and therefore the ability to determine applied forces, vary from day to day. The balance is first calibrated, then used to measure the drag of a model in the wind tunnel. The balance is returned to the calibration table. A new zero is established, but no other adjustments are made to the amplifier circuitry. The applied force or moment in figure 23 is that force/moment applied in the second calibration. The voltages from this calibration are used, but the prediction utilizes the calibration matrix that is obtained from the earlier calibration. The errors are not significantly greater. This result gives us confidence in the stability of the force balances and related circuitry.

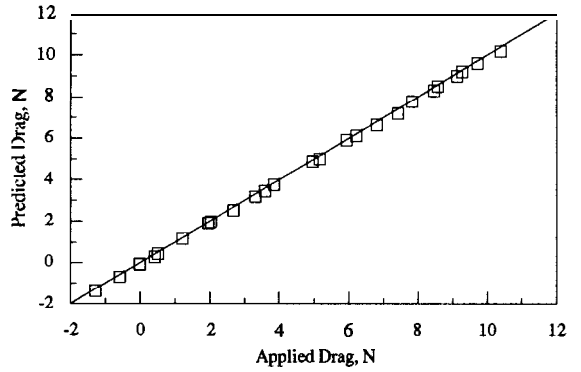

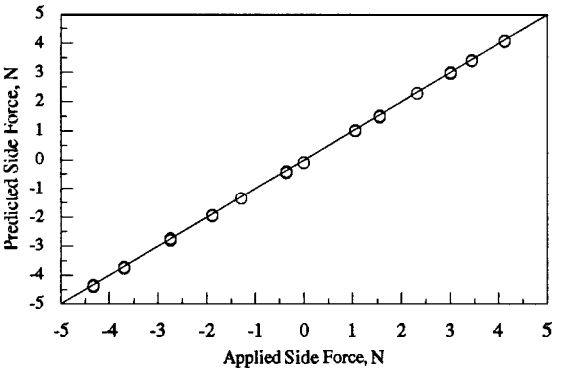

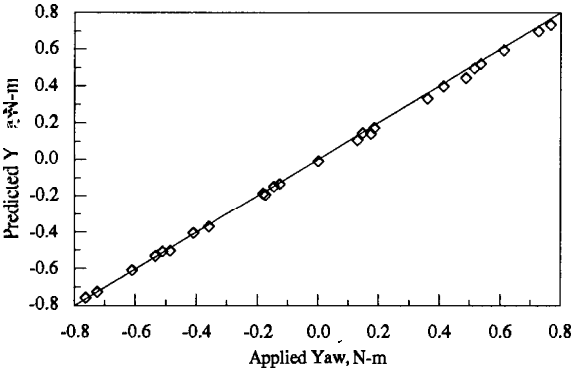

Coefficient Matrix

	Vdrag*	Vside*	Vyaw*	+
Drag	0.6101	0.0041	-0.0732	0.0115
Side Force	0.0029	0.6123	-0.0174	-0.0213
Yaw	0.0009	0.0005	0.2542	0.0043

Calibration Statistics

	Drag	Side	Yaw
Std. Error	0.0466	0.0377	0.0138
Std. Error/Mean	0.0100	0.0165	0.0357
Mean	4.6706	2.2913	0.3880

Figure 23. Comparison of day-to-day calibrations, Predicted values are found by using voltages from a current calibration and a coefficient matrix from an old calibration.

In order to determine the sensitivity of the force balance to lift, a calibration is conducted while an upward load (up to 9.8 1 N) is applied to the balance at the approximate center. The voltages that result from the calibration while lift force is applied are then used with the coefficient matrix from a standard calibration to "predict" the drag, side force and yaw moment in the presence of lift. Figure 24 gives the resulting predictions using a 9.8 N lift force. Compared to the results of a typical calibration without lift, the percentage error is almost doubled. Even in this extreme case the percent error is less than 1% of the sensor range.

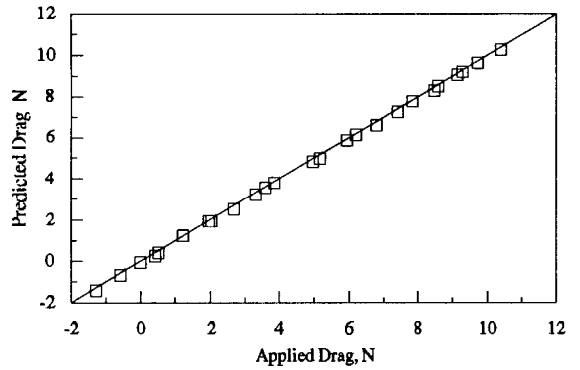

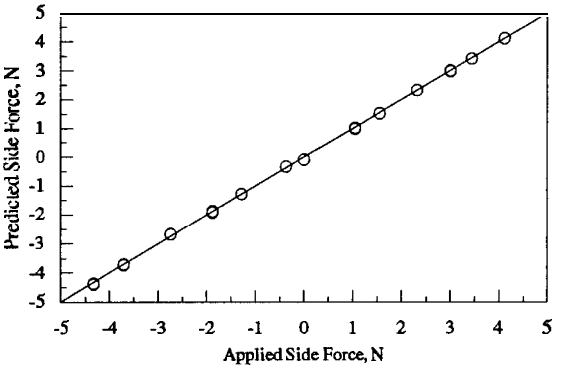

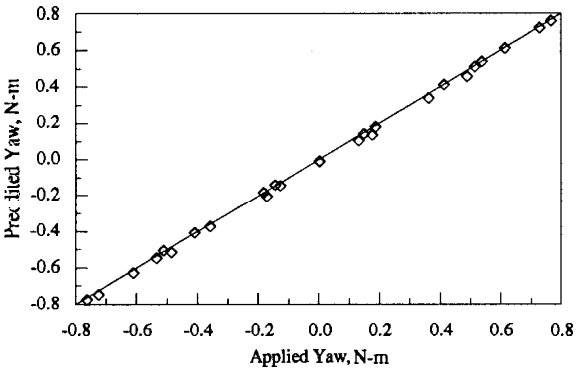

Coefficient Matrix

	Vdrag*	Vside*	Vyaw*	+
Drag	0.6101	0.0041	-0.0732	0.0115
Side Force	0.0029	0.6123	-0.0174	-0.0213
Yaw	0.0009	0.0005	0.2542	0.0043

Calibration Statistics

	Drag	Side	Yaw
Std. Error	0.0616	0.0593	0.0126
Std. Error/Mean	0.0132	0.0259	0.0324
Mean	4.6706	2.2913	0.3880

Figure 24. Effect of a 9.8 1N lift force on calibration errors.

The sensitivity to pitch and roll is examined by displacing the yoke in the vertical direction by 1 to 4 cm thereby changing the line of action of both the drag and side force. (During a standard calibration, these forces are applied through the centerplane of the balance.) When forces are measured on the model in the wind-tunnel, the lines of action of these forces are unknown and likely to be different from the balance centerplane. By displacing the yoke vertically and calibrating the balance as usual, the possible effect of this difference in line of action can be observed. As the loads are varied during calibration, the pitching and rolling moments are also varied. Figure 25 compares the magnitudes of the applied pitch and roll moment to the applied yawing moment. The voltages that result from this off-centerplane calibration can than be used with a coefficient matrix from a standard calibration to "predict" the loads that were actually applied. Again, there is a slight increase in the error as shown in figure 26, but the percentage

error stays below 1.5% of the average load for both drag and side force and less than 2.5% for yaw moment.

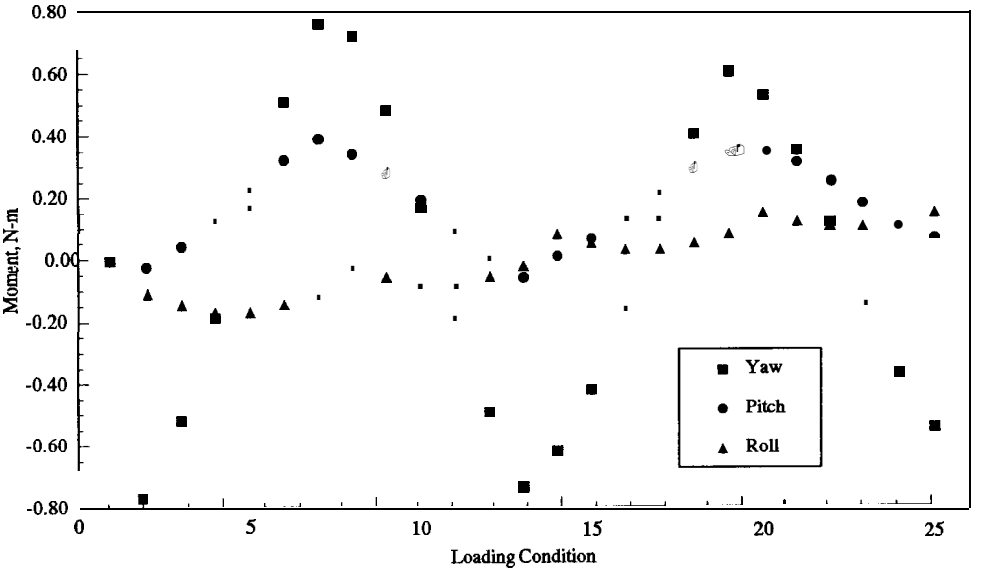

Figure 25. Variation in applied moments during calibration with yoke displaced 3.8 1 cm vertically.

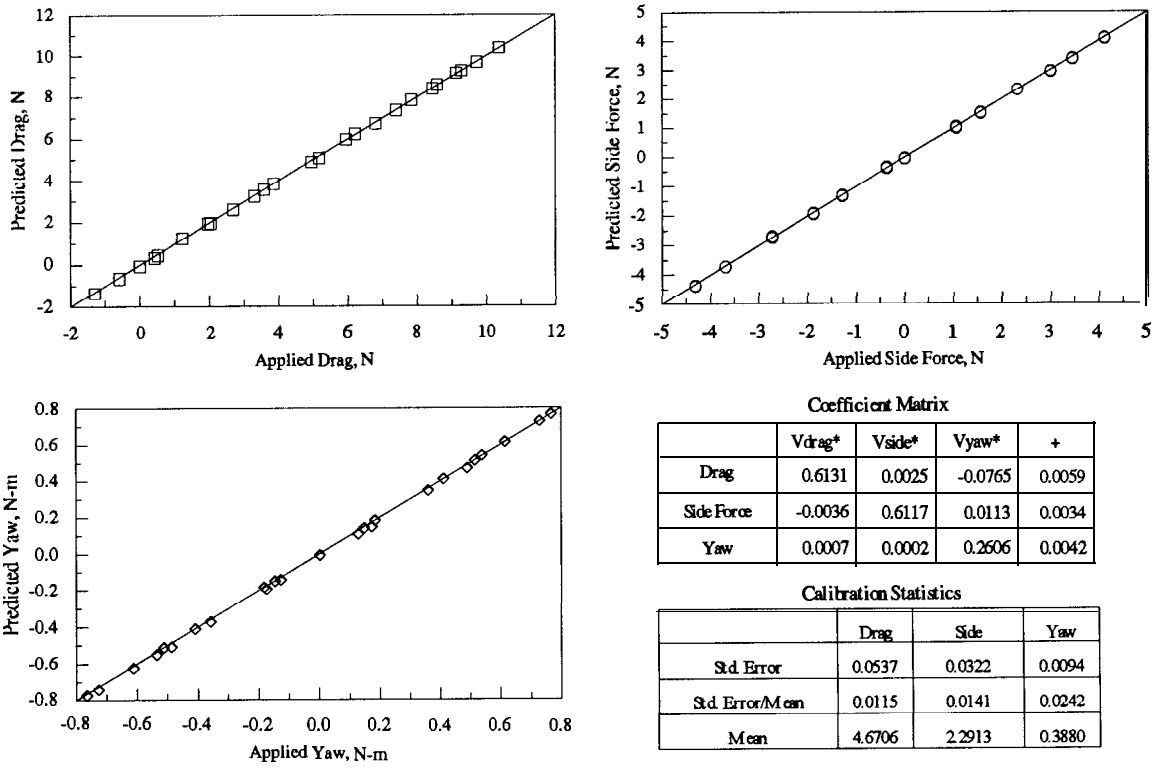

Coefficient Matrix

	Vdrag*	Vside*	Vyaw*	+
Drag	0.6131	0.0025	-0.0765	0.0059
Side Force	-0.0036	0.6117	0.0113	0.0034
Yaw	0.0007	0.0002	0.2606	0.0042

Calibration Statistics

	Drag	Side	Yaw
Std. Error	0.0537	0.0322	0.0094
Std. Error/Mean	0.0115	0.0141	0.0242
Mean	4.6706	2.2913	0.3880

Figure 26. Effect of pitch and rolling moments on calibration errors

Frequency Response to Unsteady Loading The force balance exhibits several significant modes of oscillation. Since there is little natural damping in the system, strong resonances are observed. Figure 27 gives a response curve for an unsteady load applied to the balance alone in the sideforce (cross stream) direction. The fluctuating load is provided by a motor with an eccentricly mounted weight fastened to the calibration weight pan. Resonances are noted at 45 Hz and at 80 Hz. The addition of the model adds considerable weight to the system and reduces the lowest resonance frequency to the range 20-30 Hz.

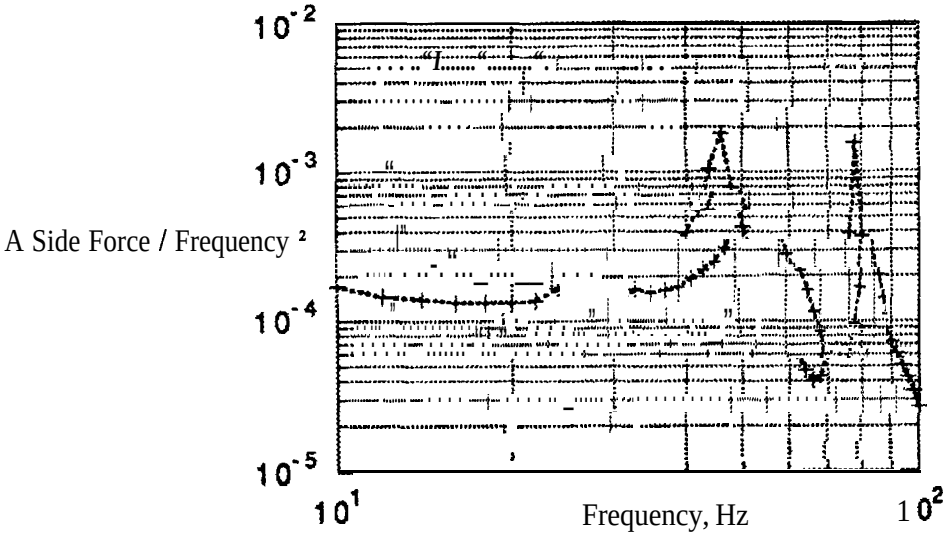

Figure 27. Dynamic response of force balance

The major unsteady loads are to be expected at the wake vortex shedding frequency given approximately by

$$\frac{fd}{U} \cong 0.2$$

where f = the shedding frequency

d = the effective diameter, 0.237 m

U = wind tunnel speed

The above relation predicts the shedding frequency to lie in the range ≈ 17 Hz at a wind tunnel speed of 20 m/sec. This value is too close to the lowest model resonance to allow unsteady measurements to be made. We are presently implementing an artificial, viscous damper for the balances. The damping can be adjusted to the critical value giving the optimum frequency response. These same tests showed that the fluctuating loads did not significantly affect the average readings.

IV. The Design and Construction of the Test Models

The Lumina APV The models used for this study are 1/8th scale replicas of the General Motor's Chevrolet Lumina All-Purpose Vehicle (APV) shown in figure 28. The physical characteristics of this 3-door, 7-passenger vehicle are listed in table 1. The maximum cross-sectional area is 2.82 m^2. The APV design is a product of the Italian firm, Pininfarina (designers for Ferrari). It has a forebody of extreme rake, and a rather blunt base. The APV was chosen over other mini-vans because of this large difference in fore-and-aft geometry. By reversing the model, one has essentially a totally different vehicle. These radically opposed contours provide the opportunity to judge the influence of vehicle shape upon performance in a platoon.

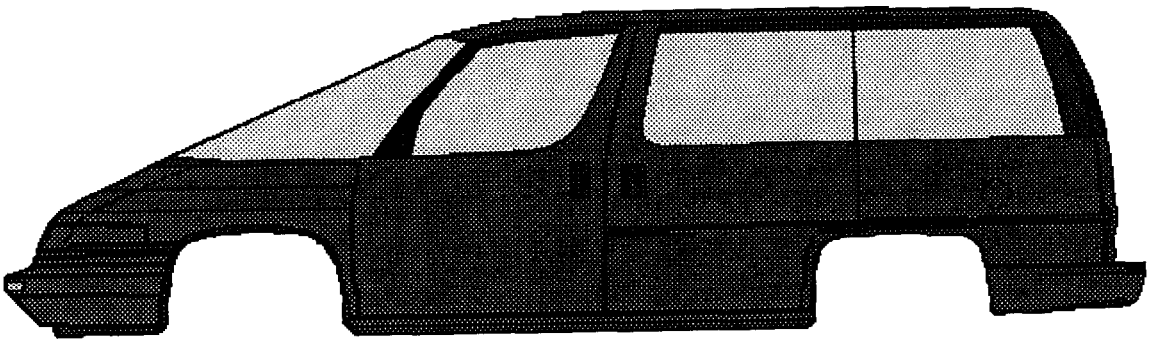

Figure 28. General Motor's Chevrolet Lumina APV

Table 1. Technical Data on Lumina APV*

Dimensions	
Wheelbase, in./mm	109.8 / 2788
Track, in./mm	59.2 / 61.4 / 1503 / 1559
Length, in./mm	194.2 / 4933
Width, in./mm	73.9 / 1878
Height, in./mm	65.7 / 1670
Ground clearance, in./mm	9.0 / 229
Mfr's curb weight, lb	3827
Weight distribution, f/r, %	59 / 41
Fuel capacity, gal	20.0
Weight/power ratio, lb/hp	23.2
Wheel size, in.	15 x 6
Tire size	205/70SR15

* Source: Motor Trend Magazine

Type	90° V-6, liquid cooled, cast iron block and heads
Bore x stroke, in. / mm	3.60 x 3.40 / 96.5 x 86.4
Displacement, cl / cu	231 / 3791
Compression ratio	8.5:1
Valve gear	OHV, 2 valves/cylinder
Fuel / induction system	Multipoint EFI
Horsepower, hp @ rpm, SAE Net	185 @ 4300
Torque, ft lb @ rpm, SAE Net	220 @ 3200
Horsepower / liter	43.5
Redline, rpm	Not applicable
Recommended fuel	Unleaded regular

Drivetrain	
Layout	Front engine, front drive
Transmission type	4-speed auto.
Gear ratios	
(1st)	2.92:1
(2nd)	1.57:1
(3rd)	1.00:1
(4th)	0.70: 1
Axle ratio	3.06:1
Final-drive ratio	2.14:1
Engine rpm, 60 mph in top gear	1700

EPA, city/hwy., mpg	17/24

Prototype Model Fabrication General Motors was kind enough to provide an IGES formatted file containing the position coordinates of the outer envelope of the APV. The file was forwarded to 3-D ***Systems,*** located in Valencia, California, a pioneer of Stereo Lithography. Stereo Lithography is a rapid prototyping method based upon the hardening of a special photopolymer at sites controlled by a computer-driven laser beam. Most of the automobile and aircraft companies now have such machines. To visualize how the fabrication is achieved, imagine any complex three-dimensional shape to consist of many thin slabs (of appropriate cross section)-much the way topographic terrain models are frequently displayed. In this application, an ultraviolet laser traces a cross-section of the object onto the surface of a vat of liquid polymer, selectively hardening the polymer to a depth of 0.125 mm (.005 inch). As each layer is formed, the platform supporting the model is lowered below the surface in similar increments in preparation for the next laser scan.

Using an available software package, SDRC® Ideas™, the IGES file is used to generate a wireframe of the APV. All minor surface features such as door and window seams, side view mirrors and door handles are removed. These features are eliminated because they significantly complicate the model, but do not contribute to a fundamental understanding of the platoon process. For similar reasons the undercarriage, which is not included in the original IGES file, is assumed to be flat. The wheel-well details, also not given in the IGES file, are based on measurements from a production vehicle.

At this point, the wireframe represents the exterior surface of the APV model. A second wireframe -a slightly scaled down version of the first-is then centered inside the original wireframe. This becomes the inner surface of the model shell. The wall thickness is chosen to be 4.8 mm. If future models are constructed, a thicker wall will probably be chosen to improve model rigidity. A 11.4 cm x 15.2 cm rectangular opening is centrally positioned in the undercarriage to accommodate the force balance. Finally, a 4-post support structure is separately designed for the force balance.

The wireframe is now used to generate a solid-surface model of the van consisting of approximately 100,000 triangular facets. It is this series of coordinates which are used to program the laser motion. The APV model is too large to be accommodated in current Stereo Lithography machines, and must be partitioned into four separate parts. To assure proper alignment when reconnecting these pieces, dowel pin holders are placed at strategic points along the interior perimeter. To "build" the physical model requires approximately 30 hours in the 3-D System SLA-500 Stereo Lithography machine. Figure 29 is a photograph of the top and bottom, front portions of the model as they are removed from the SLA-500. The four parts are joined using a thin layer of polymer and exposure to ultraviolet light. The finished product is used as a master model for a two-part RTV mold. Eight working models are cast of fiberglass from the RTV mold.

Each model is provided with a durable surface finish by spray coating in an auto-body shop. Two coats of white enamel and a single, clear coat give a surface finish of quality identical to a standard automobile finish. Wheels for the models are cut from hardwood and sprayed with the same surface finish. Aluminum axles are machined to fit the model undercarriage snugly, and are secured to the model by self tapping screws. Each wheel is press-fit to the axle. Figure 30 is a picture of the finished product in position for testing in the wind tunnel.

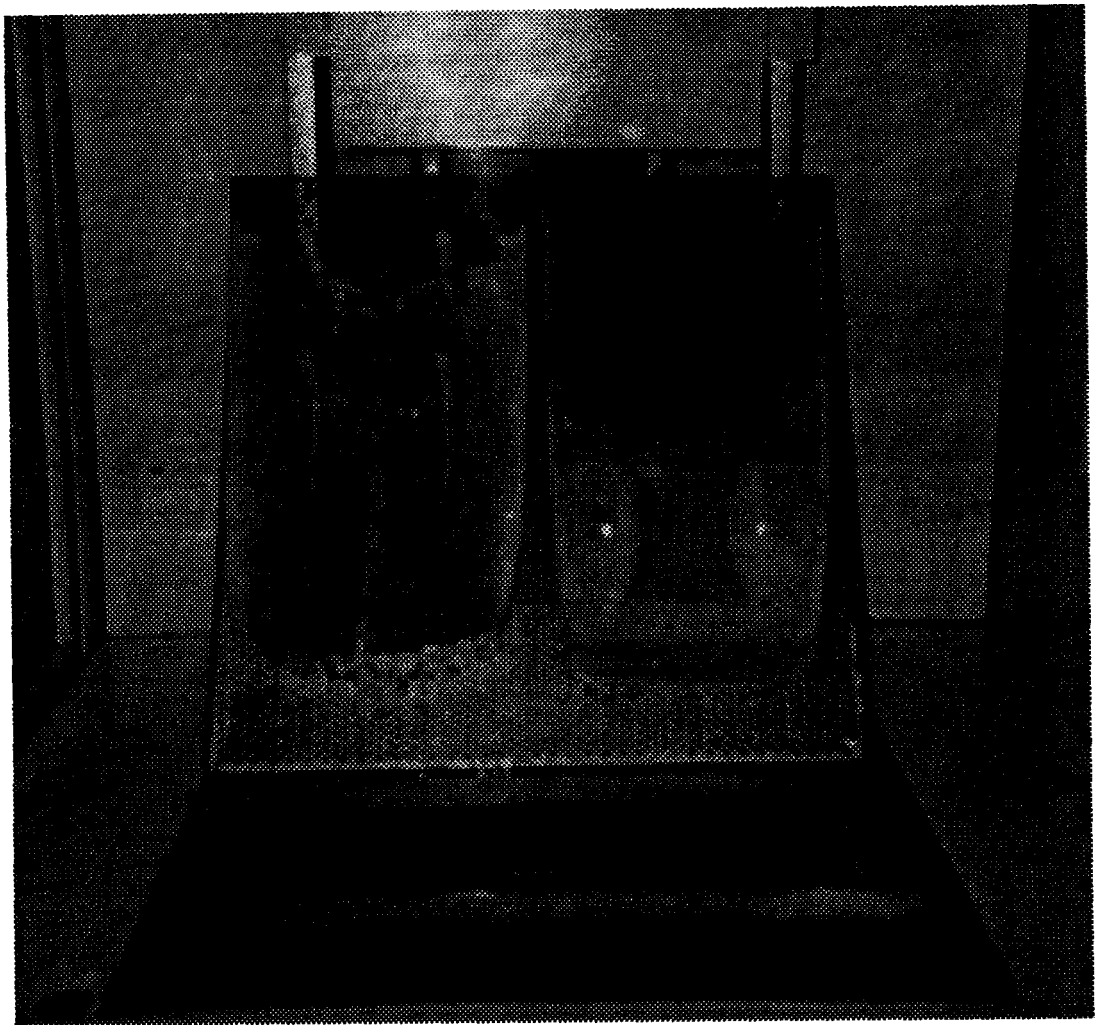

Figure 29. Photograph of the top and bottom front portions of the master model as they are removed from the SLA-500 stereo lithography machine.

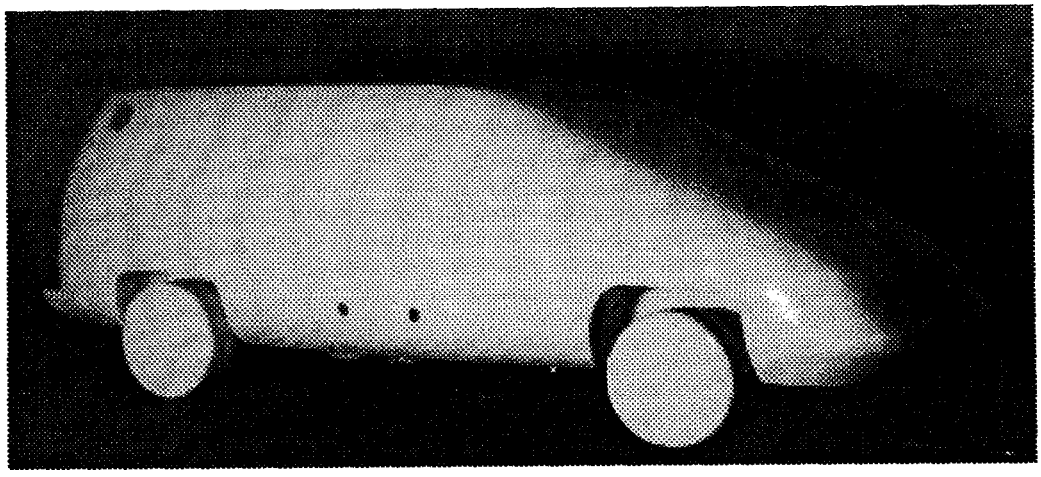

Figure 30. Photograph of model in the wind tunnel.

Model Support Details The force balance is a sandwich construction consisting of upper and lower mounting plates, and a central, cruciform-shaped, strain member (details discussed in section III). The uppermost plate is attached with machine screws to the mounting posts in the interior of the model. The length of the vertical mounting posts is such that the lower plate of the balance is flush with the model undercarriage. This lower plate fills the cut-out in the undercarriage, leaving a 2 mm clearance around the perimeter. To insure rigidity between the model shell and the force balance, the central cavity of the model is filled with a closed-cell, polyurethane foam.

The model and force balance are supported by two 15.9 mm diameter posts which extend from the lower plate of the force balance down through the ground plane and attach to one of four specially designed, moveable carriages. The carriages are mated to an optical rail affixed to the lower surface of the ground plane box (figure 2). Each carriage can be moved along the optical rail, and can be manually locked at any desired position along the tunnel centerline. (There is a central slot in the ground plane which allows this axial movement of the support posts. The slot is covered during tunnel operation.) The model ground clearance is adjusted by moving a nut along the threaded mounting posts. The support posts fit into carriage sleeves, and are locked in place to secure the model once the proper ground clearance is established. The drag of the support posts, and the portion of the model undercarriage containing the force balance lower plate, are not directly included in the measured drag. We believe the presence of the support posts has a minimal influence on the flow field around the vehicle.

Model-to-Model Reproducibility All four models containing force balances are as nearly alike as possible. Thus each model placed separately at the same location in the wind tunnel should have the same drag (also side force and yaw moment, but these are nearly zero). The differences in measured drag coefficients between models is a good indication of the resolution of the force measurement. Repeated placing and replacing of the *same* model results in measured differences in drag coefficient of about ± 0.003 N. For a nominal drag coefficient of 0.33, the error is of the order of 0.9%–very small indeed. The differences between the drag coefficients for *different* models are of the same order for two of the models. However larger differences were originally discovered between two other models. These larger differences are due to slight misalignments of the force balance within the model, and can be eliminated by a readjustment of the position using shims. The largest difference in measured C_D between all four models represents a deviation from the mean C_D of about 2%, (see discussion on page 45).

V. DRAG MEASUREMENTS

Reynolds Number, Trip Ring, and Ground Plane Sensitivities Drag coefficient data is presented in figure 3 1 for a single model installed at position x = 280 cm in the wind tunnel for a range of wind tunnel speeds. C_D is based upon a nominal value of the freestream velocity. In one case, the model has a tripping ring to insure rapid transition to turbulent boundary layer flow. Boundary layer tripping is a commonly used technique to avoid unwanted flow separation which might occur at the (lower) model Reynolds numbers but not at the (higher) Reynolds numbers characteristic of full scale operation. The tripping device used here is a flat, serrated rubber strip which can be stretched around the nose of the model at a position (s=15.25 cm) approximately two-thirds the distance from the front bumper to the top of the windshield. The Reynolds number at the trip location is approximately Us/ν = 240,000, where s is the distance along the surface from the bumper. The thickness of the trip is approximately δ^* at this location. The model rests either upon the porous ground plane or upon a portion of the ground plane which is covered with a thin sheet of mylar, referred to *as* a *footprint* from here on, to minimize suction or blowing which might possibly arise from the local pressure changes in the vicinity of the vehicle.

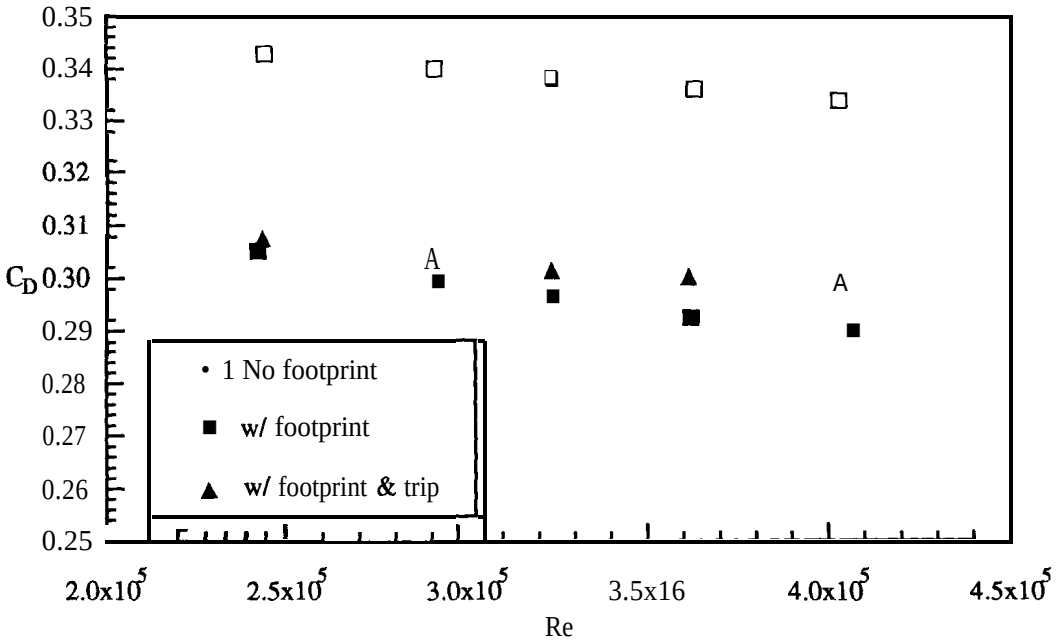

Figure 3 1. Effect of Re, trip & footprint on C_D

Consider first the open symbols which represent the porous ground plane. There is a small decrease in drag coefficient of about 3 per cent as the Reynolds number varies by a factor of about two – from $2.4x10^5$ to about $4.1x10^5$. (This reference Reynolds number is based upon the model effective diameter $d = \sqrt{4A/\pi} = 0.237$ m, where A is the cross-sectional area of the model.) A

small decrease is to be expected with increasing Reynolds number because the drag contribution directly attributable to skin friction is slightly less. The contributions due to pressure differences and to skin friction behave as follows.

$$C_D = (\text{pressure contribution}) + (\text{skin friction contribution})/(Re)^{4/5}$$

Plotting C_D versus the inverse 4/5 power of the Reynolds number for the data in figure 3 1 gives an approximately linear dependence, and suggests that about 90 per cent of the drag results directly from pressure differences, while the remaining 10 per cent arises from shear stress along the model surface (skin friction). This is a useful breakdown to keep in mind. It can be used to extrapolate the skin friction contribution to moderately higher or lower Reynolds numbers provided there are no drastic changes in the flow patterns. The remaining results – unless otherwise noted – are recorded at Reynolds numbers in the range $3.2–4.1 \times 10^5$ corresponding to wind tunnel speeds of 20 -25 meters/second.

The presence or absence of the non-porous footprint below the model has a significant effect upon the flow field. With the footprint in place, the single vehicle drag coefficient is reduced by about 15 percent. The implication is that local variations in pressure in the vicinity of the model do interact with the porous ground plane to produce a net increase in drag coefficient. This interaction is of course suppressed by the footprint.

Tripping the boundary layer results in a slight increase in drag at all Reynolds numbers. This small increase is probably due to the drag of the trip itself, and not to any significant changes in the flow pattern. Since tripping produces no real benefit, the results will be presented with no trip present.

Corrections for Wind Tunnel Walls The flow around the model in the wind tunnel is constrained by the bounding walls, and must increase in speed to a greater degree than if the walls were not present. Since the velocity is increased, the drag is also increased above the value obtained in the absence of walls. The correction for this spurious "blockage" effect consists in basing the drag coefficient upon a realistic estimate of the higher velocity surrounding the model. Empirical blockage corrections often used depend upon the ratio of model cross-sectional area to wind tunnel cross-sectional area. In the present case,

$$A_{model} / A_{wind\ tunnel} \approx 0.04,$$

is small, and the correction is of the order of a few per cent. A more precise blockage correction procedure utilizes a measurement of the static pressure distribution along one of the walls of the wind tunnel, and a knowledge of the wind tunnel geometry, to evaluate terms in an analytic

expression for the flowfield (Hackett, et al., 1979). It is accurate, but cumbersome to apply in our case because the Dryden wind tunnel has an octagonal cross section. We will resort to a simpler procedure, but one which also makes use of the static pressure distribution along the wind tunnel ceiling. First, the difference in pressure between the tunnel empty and the tunnel containing the model is determined. A number of such pressure difference distributions with the model vehicle at various positions in the wind tunnel are shown in figure 32. The pressure difference ΔC_p is defined as:

$$\Delta C_p = (p_{empty} - p_{with\ model})/(\tfrac{1}{2}\rho U_\infty^2)$$

ACP is positive when the velocity in the model cross-section is greater than in the empty tunnel. The presence of the model creates a characteristic signature which is independent of the position of the model. There is an increase in velocity (positive ΔC_p) to a local maximum in the cross-section just downstream of the plane containing the center of the model. Behind the model, the difference pressure coefficient decreases to a smaller non-zero value which represents the blockage effect of the vehicle wake. Our correction for blockage consists of taking the velocity corresponding to the maximum ΔC_p as representative of the velocity in the plane of the model. This value of velocity is used to determine the local dynamic pressure as the basis of the drag coefficient. Thus

$$D = C_{Dlocal}(Area)(\tfrac{1}{2}\rho U_{local}^2),$$

and

$$\tfrac{1}{2}\rho U_{local}^2 = PO - p_{local}$$

p_{local} determined at the point of maximum ΔC_p .

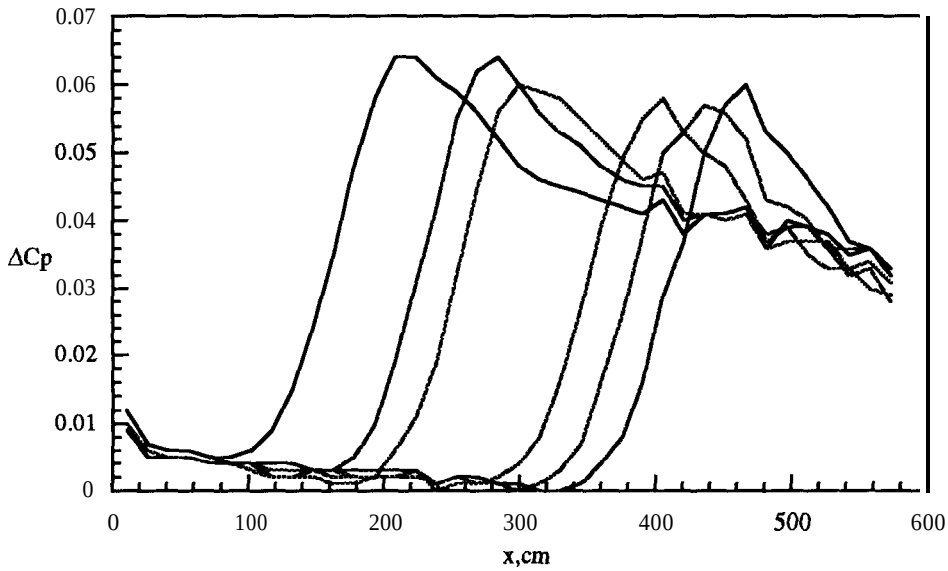

Figure 32. Single model pressure signatures at different streamwise locations

There is another effect of wind tunnel confinement which was briefly touched upon in chapter III. Due to boundary layer growth along the walls, the core flow in the wind tunnel increases slightly in the downstream direction, as noted again in figure 33. Here $C_p = p_{local} - p_\infty / (\frac{1}{2}\rho U_\infty^2)$, and p_∞, U_∞ are taken to be the values obtained by the reference Pitot-static tube at the front of the test section.) The usable portion of the ground plane extends from x = 40 cm to x = 500 cm. Ahead of x = 40 cm, the flow is still accelerating around the nose of the ground plane. Beyond x = 500 cm, the flow is influenced by the trailing edge flap. The favorable pressure gradient (decreasing pressure) is most noticeable over the forward half of the test section, and largely disappears over the downstream two meters when suction is applied. A (small) favorable pressure gradient will cause a (small) increase in drag because the forward portion of the vehicle experiences a slightly greater pressure than the pressure occurring over the rear portion. This effect is often referred to as "horizontal buoyancy" because it is similar in form to the vertical force produced upon a body by the hydrostatic pressure gradient in a fluid at rest.

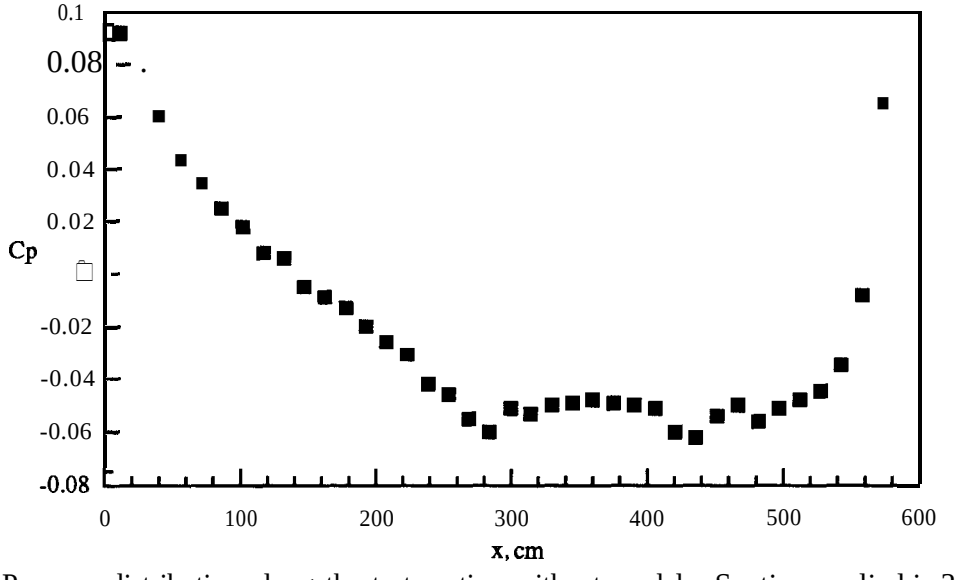

Figure 33. Pressure distribution along the test section without model. Suction applied is 35% of max.

The single vehicle results presented here have not been corrected for this small effect. However, the platoon measurements to be discussed momentarily are presented as ratios of the drag coefficient in the platoon to the single vehicle drag coefficient at the identical position in the wind tunnel Since both drag coefficients contain the similar horizontal buoyancy effect, the *ratio* is substantially independent of horizontal buoyancy.

To understand the importance of blockage and buoyancy, figure 34 contains three estimates of drag coefficient for a typical vehicle model run with the model placed at different positions along the length of the test section. The open symbols correspond to the drag coefficient determined on the

basis of the wind tunnel velocity at the forward position of the reference Pitot tube. Since tunnel speed and the measured drag actually increase with downstream position, the drag coefficient – when referenced to the fixed upstream velocity – will also increase. This is clearly incorrect. The hatched symbols represent the same drag measurement, but now referenced – at each model position – to the local velocity in the empty tunnel. Better, but still not correct. The filled symbols represent the best estimate corrected for blockage by using the higher local velocity in the presence of the model. It can be seen that these final coefficient estimates are sensibly independent of position in the wind tunnel, and have the smallest standard deviation.

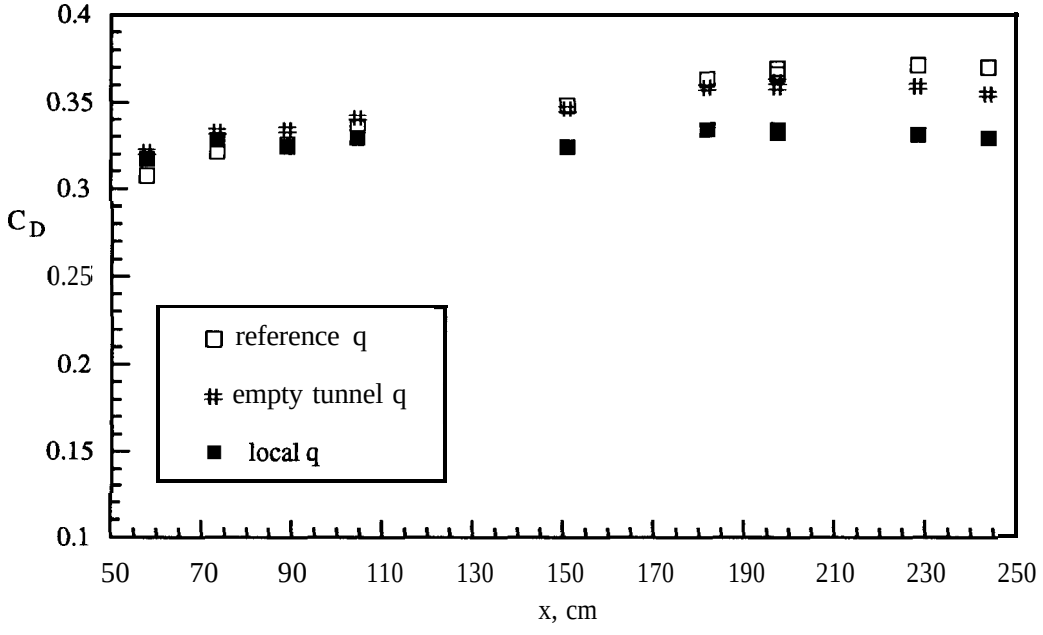

Figure 34. Effect of blockage correction method on C_D

The Single-Vehicle Drug Coefficient Figure 35 contains drag coefficient estimates for a single vehicle at different positions in the wind tunnel, utilizing all the blockage corrected data available for four different models. These data represent measurements by several individuals recorded over a period of several months. Each model contains a separate force balance. The force balances are calibrated prior to each use in the wind tunnel. Each drag measurement is accompanied by a determination of the reference Pitot-static pressures, and by a digitization of the static pressure distribution at 38 stations along the wind tunnel ceiling. Two surface conditions are maintained – the first is the unaltered, porous ground plane surface. The second surface contains a stick-down shelf paper strip of 91 centimeter width along the centerplane of the tunnel from x=120 cm to x=396 cm. The vehicle positions are contained within this strip so there is always a minimum of 1/4 car length of covered surface ahead and behind the vehicle.

The estimates fall into two ranges depending upon whether the ground plane is covered or porous. In fact, the ground plane is the only significant variable among the different conditions presented. The average drag coefficient on the porous ground plane – considering all models at all tunnel positions – is $C_D = 0.328 \pm 0.006$ (or 2%). There is a slight tendency for the green model to record higher values and the red model to record lower values, and no significant difference between blue and yellow.

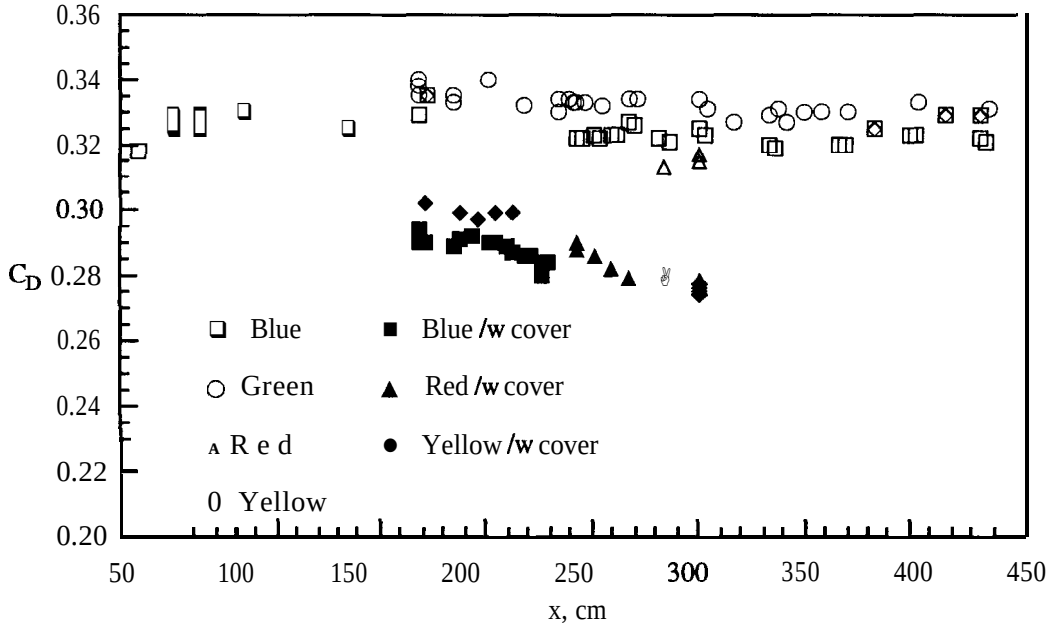

Figure 35. Single model drag coefficient estimates after correction

For the covered surface, the drag coefficient is lower, $C_D = 0.288 \pm 0.007$. A portion of this variance is a result of a slight but noticeable downward trend with downstream position. This probably represents the effect of boundary layer growth on the solid surface. Measurements of the boundary layer thickness at x=300 cm with the cover strip in place give $\delta^* \approx 4.2$ mm. Wind tunnel testing by others indicates that having too thick a surface boundary layer retards the flow under the vehicle and generally leads to a decrease in the estimated drag coefficient, Conventional wisdom is that the ground plane boundary layer may be neglected provided the model vehicle ground clearance exceeds $10\delta^*$. Here the ground clearance is about 37 mm, so the rule-of-thumb is violated at the most downstream vehicle position.

For platoon drag measurements, the covered surface is not a possible choice because boundary layer thickness would be prohibitively large. In fact, the 4-vehicle platoon at spacing of 1 car-length takes up the entire usable test section – a length of 4.7 meters. The purpose of the porous surface is to control boundary layer growth. The "penalty" to be paid for its use is that the flow over the porous surface interacts with the vehicle to produce a higher drag coefficient. The platoon

drag estimates to follow are presented as a *ratio* of the vehicle drag as a platoon member, divided by the drag of the single vehicle. Since both measurements utilize the same porous ground plane, the ground plane effect is accounted for to lowest order. But although the *ratio* should be less sensitive to the ground plane surface condition than the drag coefficient itself, there may still be interactions between the platoon and the ground plane which remain unaccounted. The effect will not be clear until more detailed measurements become available. In the meantime we present these results with this word of caution.

Platoon Drag Drag is measured on each of 2, 3 and 4 models in tandem in the wind tunnel. The spacing between models is uniform and measured from the trailing edge of the forward vehicle to the leading edge of the rear vehicle. The distance is normalized by the model length, so that spacing 1 is a distance of 1 car-length. The data presented is averaged over at least three sets of independent measurements. All test results lie within the error bounds established from the single vehicle measurements shown in the figures.

The 2-Vehicle Platoon Figure 36 gives data for a 2-vehicle platoon as a function of spacing between the vehicles. The forward vehicle is represented by the squares – the rear vehicle by circles. The ordinate is the vehicle drag coefficient as a member of the platoon, $C_{Dplatoon}$, normalized by the single vehicle drag coefficient *at the same position in the wind tunnel,* $C_{D\infty}$. Both estimates are corrected for blockage. In this case, the surface is the porous ground plane. For separations greater than about one vehicle length, the relationship between the drag coefficients is what would be expected. The forward vehicle is not influenced by the presence of the trailing vehicle at these separations. The rear vehicle – being exposed to a lower oncoming velocity in the wake of the forward vehicle – experiences a drag savings of about 25 per cent at spacing 1, decreasing to about 15 per cent savings at spacing 3. The slope of the data for the trail car suggests that the C_D ratio will remain below unity out to a spacing of about 10 car-lengths.

As spacing decreases from a value of about one, the forward vehicle begins to feel the presence of the trailing vehicle. The drag coefficient of the forward vehicle drops steadily as spacing decreases – to a value of about $0.85C_{D\infty}$ when the spacing is half a model length. C_D for the trailing car drops to about $0.66C_{D\infty}$ at spacing 1/2. Three sets of independent measurements have been made to support these observations. The three separate test results all lie within the error bounds established from the single vehicle measurements shown in the figure. (The raw data for all these measurements is presented in the appendix.) Indications are that there is a crossover at about spacing 1/3 and the drag of the trail vehicle becomes greater than the lead vehicle. However at spacings less than 1/2, the flowfield is very unsteady, and model vibrations may cause uncertainties not accounted for here. Data at these small spacings will not be presented until additional measurements have verified the results.

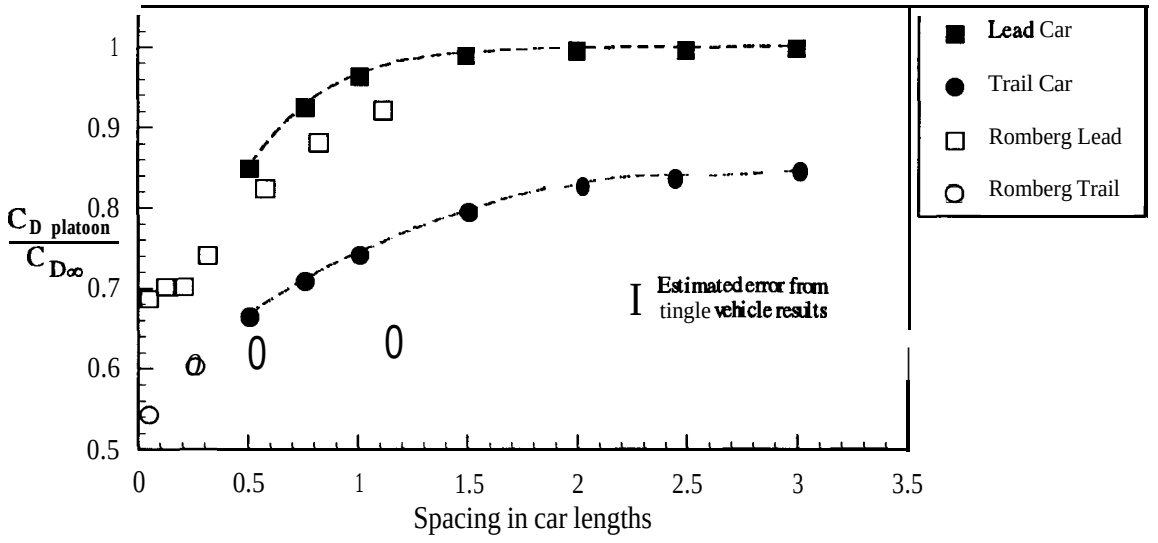

Figure 36. Drag reduction for a 2-car platoon

Data from Romberg, et al.(1971) is reformatted and presented in figure 36 along with the 2-vehicle platoon data. The results for the lead car for both studies are in surprisingly good agreement considering the very different geometries used. The results for the trailing car, where overlap exists, are different. Notably, the data of Romberg, et al. shows only a slight increase in trailing car drag as spacing increases from 1/2 to 1. It suggests that an extremely large spacing would be required for the trail car C_D ratio to return to unity. Interestingly, the two Romberg, et al. data points at spacing 0.05 and 0.25 fall almost directly on a continuation of our trail-car data.

The 3 and 4-Vehicle Platoons The 3-vehicle and 4-vehicle drag coefficients are shown respectively in figures 37 and 38 as the filled symbols. The results are quite striking. In the 3-vehicle platoon at spacing 1/2, the middle vehicle has the lowest drag coefficient – approximately 55 % of the single-vehicle value! Also at spacing 1/2, the trailing vehicle has an intermediate drag coefficient of 0.68 $C_{D\infty}$, but the trail vehicle drag (coefficient) is not as strong a function of vehicle spacing. The result is that at spacing 1, vehicle 3 crosses vehicle 2 to achieve, and thereafter maintain, the lowest drag.

A similar behavior is observed for the 4-vehicle platoon. The two interior members of the platoon have the lowest drags at spacing 1/2. The drag coefficient for the third vehicle has now fallen to about 50 per cent of the single-vehicle value! The trail vehicle now has a drag coefficient of $0.62C_{D\infty}$ at spacing 1/2, and there are corresponding crossovers, so that at (approximately) spacing 1, the trail vehicle becomes the low-drag vehicle.

The trends in these results are consistent, and allow a generalization to a platoon of n-vehicles, where n is greater than four. The hatch marks and open squares in figure 38 represent data for the lead vehicle in 2 and 3-vehicle platoons. By comparison with the 4-vehicle result, it is concluded

that the drag of the lead vehicle is not much affected by the size of the platoon (provided of course there are at least two vehicles). The drag of the first interior vehicle also appears little affected by the number of vehicles in the platoon, as the circle symbols in figure 38 suggest. However, succeeding interior vehicles appear to have progressively lower drag coefficients, as is true for the 3rd vehicle in the 4-vehicle platoon. The drag coefficient of the trail vehicle also decreases with increasing size of the platoon, as the data for crosses (n=2), open triangles (n=3), and solid diamonds (n=4) indicates.

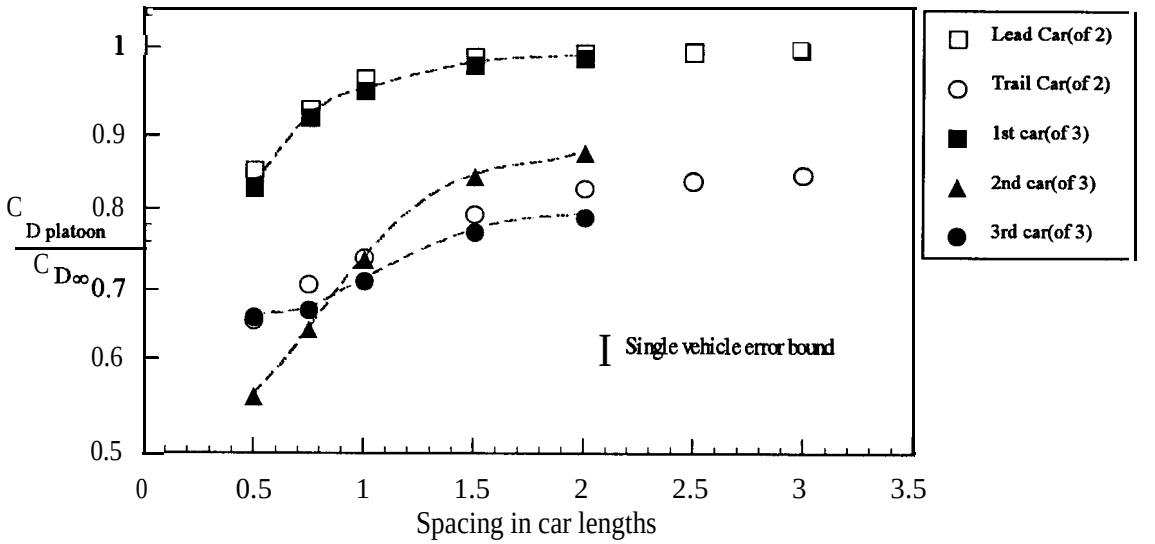

Figure 37. Drag reduction for a 3-car platoon. Open symbols show previous 2-car data.

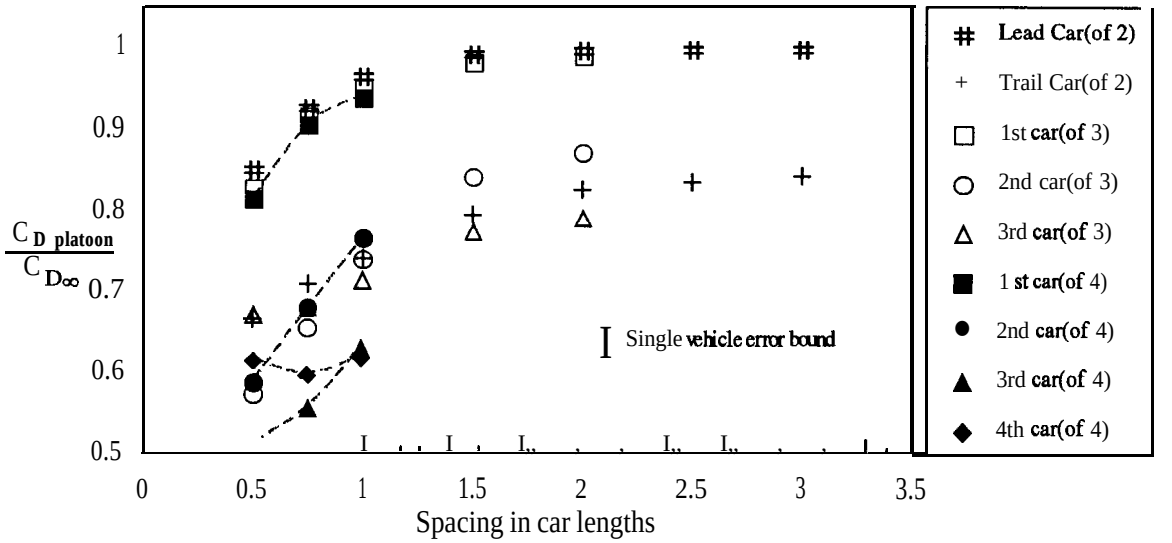

Figure 38. Drag reduction for a 4-car platoon. Open symbols show previous 3-car data. Hatched symbols show previous 2-car data.

Average Drag Savings for n-Vehicle Platoon The measurements presented above show that reductions in drag for automobiles traveling in a platoon are substantial. The quantified savings can best be presented in terms of an average drag coefficient for the platoon as shown in figure 39. The average is defined as

$$(C_{Dplatoon})_{average} / C_{D\infty} = (1/n) \Sigma(C_{Di} / C_{D\infty}),$$

where i represents the i^{th} member of the platoon. All three platoons approach the same 10 per cent saving at spacings much larger ***than*** one ***vehicle-length.*** At spacings less ***than*** one, ***the incremental saving*** is about 0.06 for each additional platoon member. Such a trend cannot continue indefinitely, and one would anticipate the average platoon drag to approach a limit point as the number of platoon members increases to large values. The present data can be used to estimate this limit by replotting the average drag coefficients as a function of 1/n for various values of spacing, figure 40. Extrapolating each of these spacing to the origin gives an estimate of the drag for that spacing as n increases indefinitely. This result is also shown in the preceding figure as the curve labeled n = ∞.

Returning again to figure 39 and to spacing 1/2, the 4-vehicle platoon represents an average drag coefficient of about $0.6C_{D\infty}$. The predicted minimum is approximately $0.5C_{D\infty}$, and all platoons of length greater than four would lie within these two bounds. It should also be noted that the slopes in figure 39 imply even greater reductions at smaller spacings.

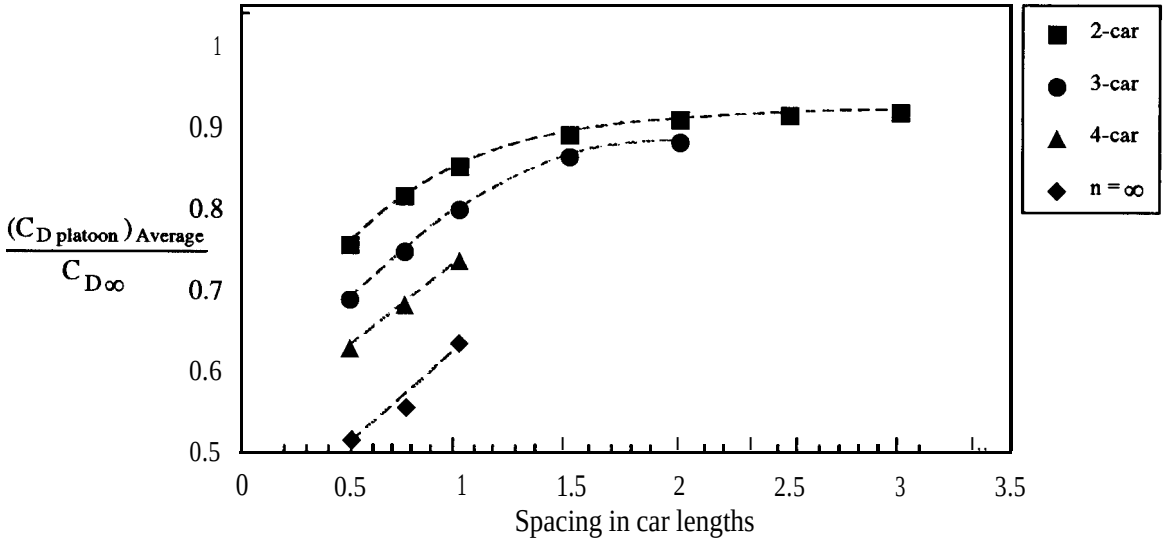

Figure 39. Average drag of a platoon of varying size

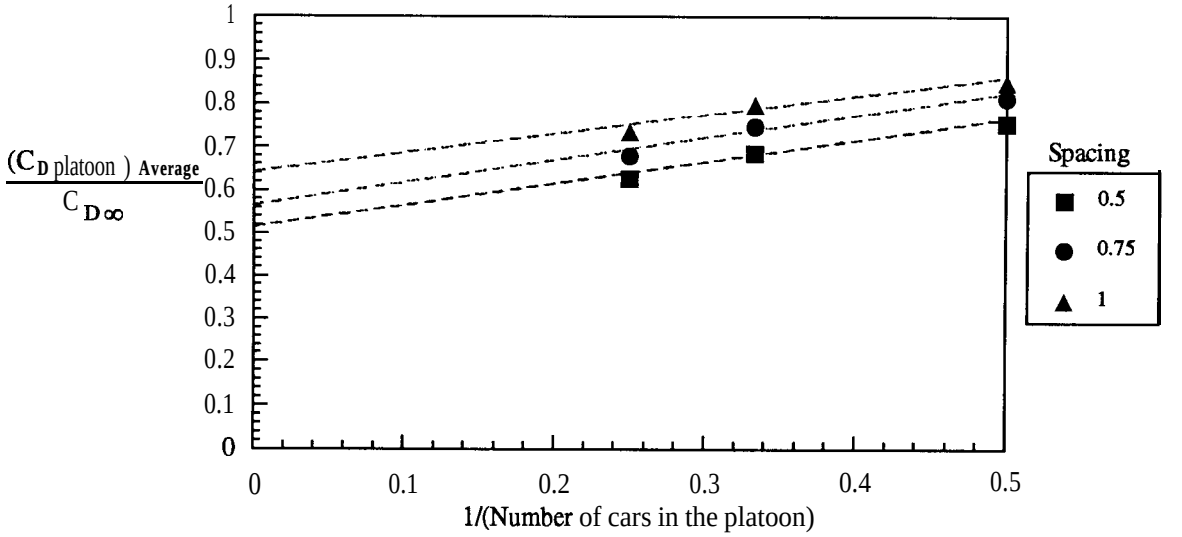

Figure 40. Average drag coefficients as a function of l/n cars

Mileage Estimates and Projected Fuel Savings Using Platoon-Averaged Drag Coefficients

Reductions in drag are a benefit in every imaginable way. Less drag means less fuel consumption – and consequently less pollution – for the same platoon speed. Alternatively, a greater platoon speed could be sustained for the same non-platoon fuel consumption. For example, if these results are translated to full-scale vehicles, platoon operation at 55 MPH (where overcoming aerodynamic drag represents roughly 50 per cent of fuel expenditures) would be expected to result in a 20-25 per cent fuel saving compared to non-platoon operation at identical speeds (Sovran et al. 1983). Extrapolation of our wind tunnel result to full-scale vehicles must be done cautiously for several reasons. Full-scale road vehicles are aerodynamically "dirtier" than our wind tunnel models, and probably would experience less drag reduction. In addition, we have not conclusively established the influence of the porous ground plane. Vehicle shape is also expected to have a significant influence upon possible drag reductions.

With respect for these differences, the method of Sovran(1983) for tractive-energy-based estimates of fuel economy is applied to our wind tunnel data. Results are presented in figures 41 and 42. The fuel economy of the APV for highway driving conditions is nominally 24 miles per gallon. Figure 41 shows that this can be increased to a value of over 3 1 miles per gallon for large platoon sizes with an inter-vehicle spacing of 0.50. Figure 42 shows the same data as a percentage of the single car highway gas mileage.

When the C_D of a vehicle traveling on a highway is decreased (by joining a platoon), the power required decreases and allows two options. One option is to increase U until the power required matches the original. The other option is to continue at the same U and ease off the accelerator pedal. With the latter option, the engine is operated at a smaller fraction of full load. This new

operating condition would correspond to a point on the engine map that will probably have a higher value of brake specific fuel consumption(bsfc). Since the engine is operating at a higher bsfc, the reduction in fuel consumption due to the decrease in drag is not maximized. Sovran's method is based on an idealized car model for which the enginedriveline system is rematched to recover the original bsfc. This would be equivalent to cars shifting into a special "platooning gear", so that the values in figures 41 and 42 reflect the maximum savings possible.

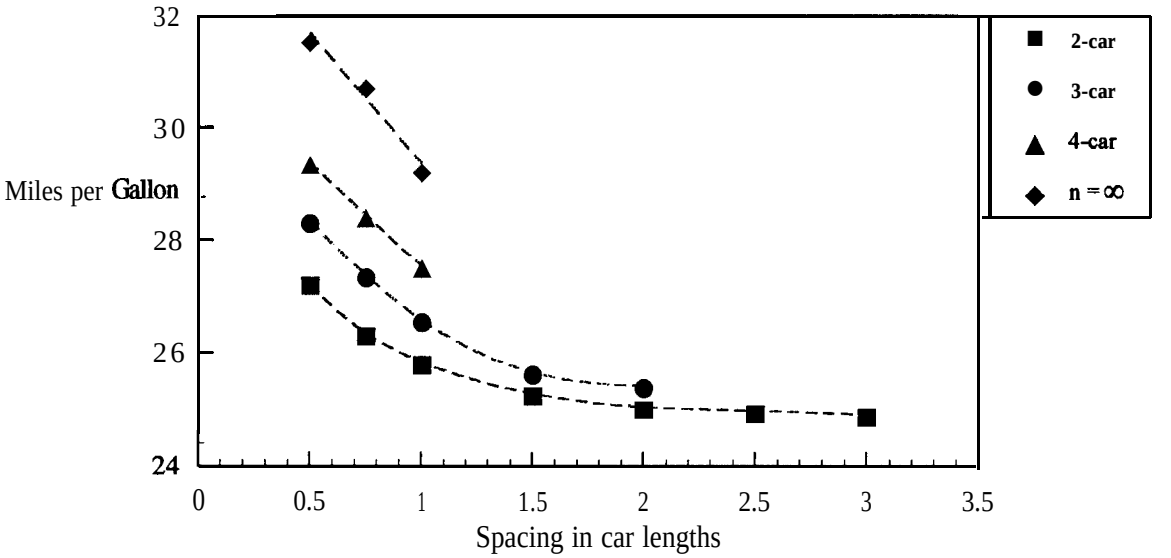

Figure 4 1. Projected effect of platoon size and spacing on the fuel economy (miles per gallon) of the Lumina APV.

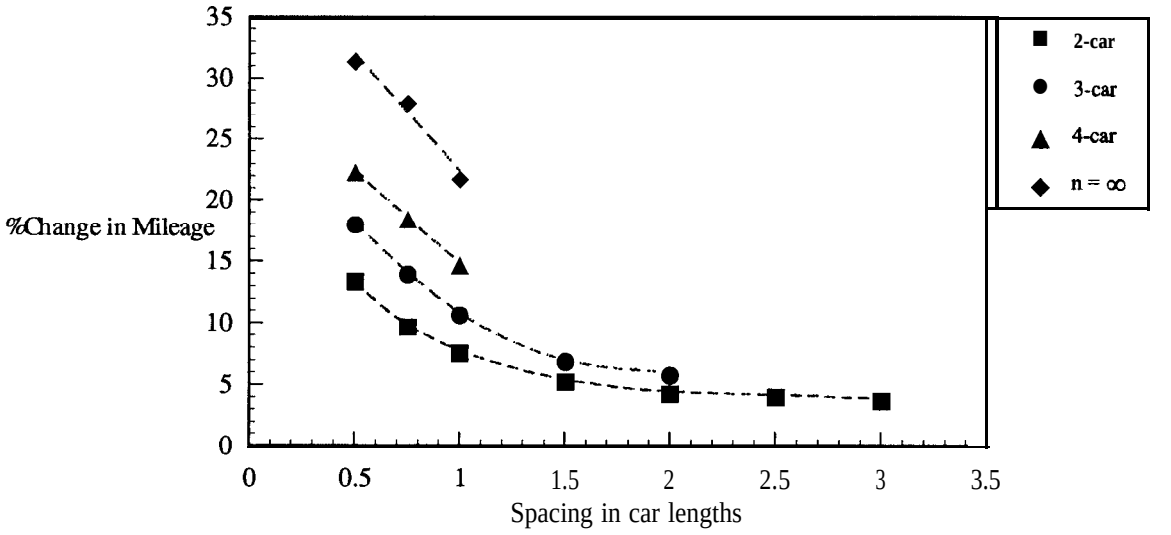

Figure 42. Percentage increase in mileage as a function of platoon size and inter-vehicle spacing.

Additional Research Goals This report is the first of a series of reports summarizing the aerodynamics of platoons. More results will be added to the present findings to provide a complete picture of platoon operation. Imagining a time frame of 3 years for completion, the following list describes an itemized step-by-step procedure making best use of our capabilities. The items categorized as 'immediate' will be completed in the present year ending September 1994. Items categorized as 'longer term' will be proposed for study in the following two years.

Immediate goals:

i.) Complete platoon drag measurements for vehicle spacings of less than one-half car length. The large unsteady forces present at short vehicle spacings required us to modify the force balances by retrofitting each balance with a damping device. The dampers work as expected, and we are now ready to complete the drag force measurements.

ii.) Compare the drag results obtained for a solid ground plane and a porous ground plane. The use of the porous ground plane requires further documentation. Boundary layer growth on the solid ground plane precludes its use for the longer platoons. However, the drag coefficients for the 2 car platoon at short spacings can be used to compare the solid and porous ground planes.

iii.) Estimate the importance of vehicle geometry on drag by utilizing other model arrangements. We anticipate that the strong aerodynamic interactions among platoon members at short spacings will be sensitive to vehicle geometry. Quantification of the sensitivity can be estimated by operating our present vehicle models in different orientations with respect to one another. Drag measurements with model orientation reversed (that is all backs forward), and for back-to-back and front-to-front geometries will be obtained.

iv.) Determine drag, side force & yawing moment for small platoon misalignments. The perfect alignment of the platoon will be destroyed as new vehicles enter and old members leave. Even during steady operation, small misalignments are inevitable. In addition to changes in drag, significant side force and yawing moments will be generated by misalignment. Knowledge of all *the* forces and *the variation of forces* with the degree of misalignment are essential parameters for vehicle control system design.

Longer term (2-3 year) goals

v.) Measurements of platoon drag in a crosswind. The presence of a crosswind is another important platoon misalignment. The present wind tunnel set-up has provision for a ten degree yaw of the platoon direction with respect to the axis of the wind tunnel. At 60 MPH, ten degrees of yaw simulates the effect of a 10.6 MPH sidewind.

vi.) Measurement of the unsteady force components-particularly at spacings less than one vehicle length. The steady forces we have discussed represent the mean or averaged values. There are additional unsteady force components which can be significant at high speeds--particularly for vehicles traveling in the near wake of another vehicle. For platoon operation, the unsteady force components are expected to be significant for control system design when vehicles are operating within the strongly interacting regime (spacing less than one vehicle length).

vii.) Determination of inter-vehicle flowfields. Previous measurements will document forces and yawing moments, but will not provide explanations for how these forces and moments are achieved. A more detailed understanding is required to extrapolate the present results with confidence to other, related situations. Several means for determining the detailed inter-vehicle flowfield include: investigation of surface streamline flow patterns; mapping of local flow velocity and flow direction in regions between vehicles; and detailed studies of separation and reattachment of the flow between vehicles.

viii.) Limited road tests (using full scale vehicles) to verify drag coefficient predictions. We presently have in mind a procedure for directly determining the drag of separate vehicles in 2,3 and 4-vehicle platoons-at least for a limited number of spacings. The results are to be compared with the more complete, detailed results from the wind tunnel tests.

References

1. LeBlanc, P. J.; 1992; *An Experimental Investigation of Transitional Instabilities in Luminar Separation Bubble Flows on airfoils at Low Reynolds Numbers;* Ph.D. Thesis; University of Southern California

2. Hucho, W-H., *Sovran, G.;* 1993; *Aerodynamics of Road Vehicles;* Annu. Rev. Fluid Mech.; No. 25; p. 485-537

3. Ono, K., & Hatamura, *Y.;* 1986; *A New Design for 6-Component Force/Torque Sensors,* Mechanical Problems in Measuring Force and Mass; Wieringa, H. (ed.); Martinus Nijhoff Publishers, Dordecht, p. 39-48

4. Ochiai, *Y.,* Kameoka, K., Sugisako, T., Ono, T.; *1986; Application of a New Beam Type Loadcell to Mechanical Hand;* Mechanical Problems in Measuring Force and Mass; Wieringa, H. (ed.); Martinus Nijhoff Publishers, Dordrecht, The Netherlands

5. Bulmer, M. G.; 1979; Principles of Statistics; Dover, New York

6. Hackett, J. E., Wilsden, D. J., & Lilley, D. E.; 1979; *Estimation of Tunnel Blockage from Wall Pressure Signatures: A Review and Data Correlation,* NASA CR-15,224

7. Romberg, G. F., Chianese, F, Jr., & Lajoie, R. G.; 1971; *Aerodynamics of Race Curs in Drafting and Passing Situations;* SAE Paper No. 710213

8. *Sovran, G.;* 1983; *Tractive-Energy-Based Formulae for the Impact of Aerodynamics on Fuel Economy Over the EPA Driving Schedules,* SAE Paper No. 830304

Appendices

Appendix A: Z-Car Platoon Data

1st Regular 2-Car Platoon Data Set

Both cars facing forward. Yellow was lead (stationary). All single car data was taken before any platoon data was taken. Data at 15 and 20 m/s also taken, results presented later. U_∞=25 m/s.

Single Car Data

Car1#	Position	Drag	Side F	Yaw	C_{Dref}	C_{Plocal}	C_{Dlocal}
Yellow	185.4	6.198	-0.674	-0.041	0.366	-0.088	0.336
Green	278.2	6.254	0.054	-0.121	0.372	-0.110	0.335
Green	309.2	6.209	-0.038	-0.107	0.367	-0.106	0.332
Green	340.2	6.116	0.004	-0.102	0.366	-0.104	0.332
Green	371.2	6.172	0.042	-0.136	0.367	-0.108	0.331
Green	402.1	6.274	0.208	-0.114	0.373	-0.117	0.334
Green	433.1	6.195	0.191	-0.141	0.368	-0.109	0.332

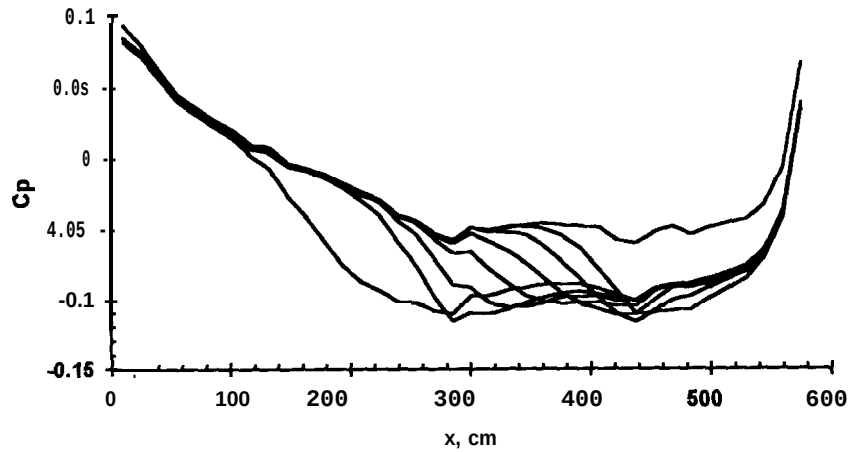

Static Pressure Distribution

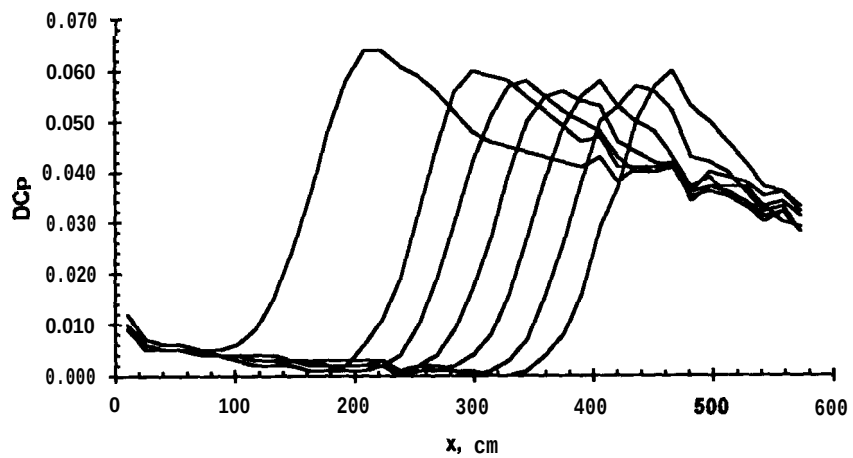

ΔC_p Distribution

Platoon Data

U_{ref}=25 m/s, $Position_1$=185.4 cm

Position2	Spacing	Drag1	SideF1	Yaw1	Drag2	SideF2	Yaw2	CD_{ref1}	CD_{ref2}	$\frac{CD_{ref1}}{CD_{\infty 1}}$	$\frac{CD_{ref2}}{CD_{\infty 2}}$
278.2	0.50	5.302	-0.678	-0.030	4.523	0.063	-0.076	0.315	0.269	0.861	0.723
309.2	1.00	6.018	-0.740	-0.036	4.874	-0.105	-0.098	0.355	0.288	0.971	0.783
340.2	1.50	6.084	-0.728	-0.046	5.089	-0.089	-0.106	0.363	0.304	0.992	0.830
371.2	2.00	6.155	-0.697	-0.045	5.237	-0.067	-0.122	0.366	0.312	1.001	0.850
402.1	2.50	6.162	-0.718	-0.037	5.438	-0.034	-0.125	0.366	0.323	1.001	0.867
433.1	3.00	6.181	-0.739	-0.033	5.441	-0.025	-0.146	0.367	0.323	1.002	0.878

Note: $CD_{\infty}=CD_{ref}$ from single car data

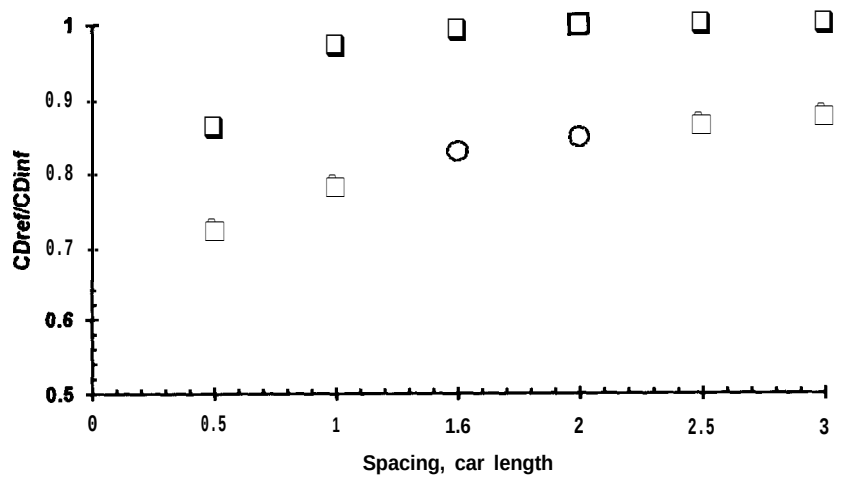

Uncorrected Platoon C_Ds

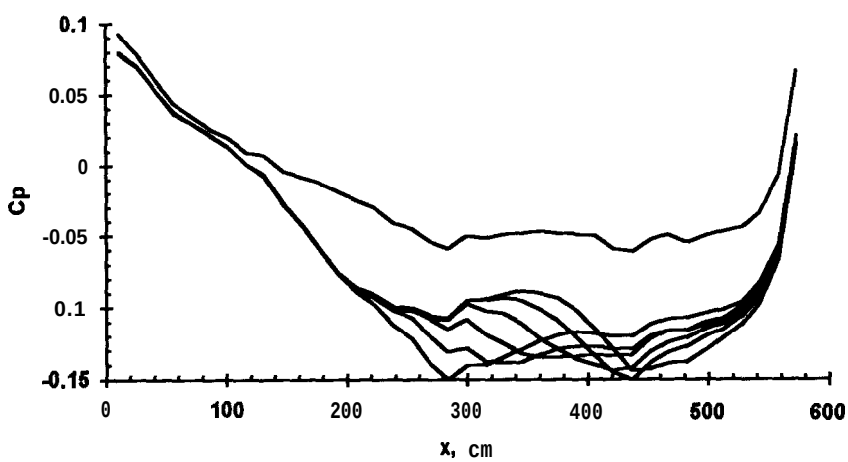

Static Pressure Distribution

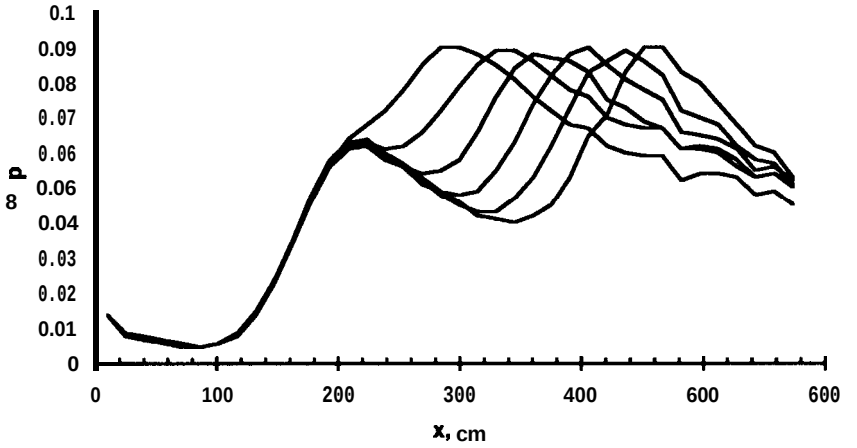

ΔC_p Distribution

Spacing	ΔCp_{max}	X_Cpmax	Cplocal2	Cplocal1	CDlocal2	CDlocal1	$\frac{CD_{loc1}}{CD\_1}$	$\frac{CD_{loc2}}{CD\_2}$
0.500	0.090	280.87	-0.150	-0.089	0.234	0.289	0.861	0.697
1.000	0.089	325.94	-0.139	-0.086	0.253	0.327	0.973	0.761
1.500	0.088	355.98	-0.135	-0.086	0.268	0.334	0.995	0.807
2.000	0.090	401.05	-0.140	-0.087	0.273	0.337	1.003	0.826
2.500	0.089	431.09	-0.150	-0.087	0.281	0.337	1.003	0.843
3.000	0.090	446.11	-0.143	-0.088	0.282	0.337	1.004	0.852

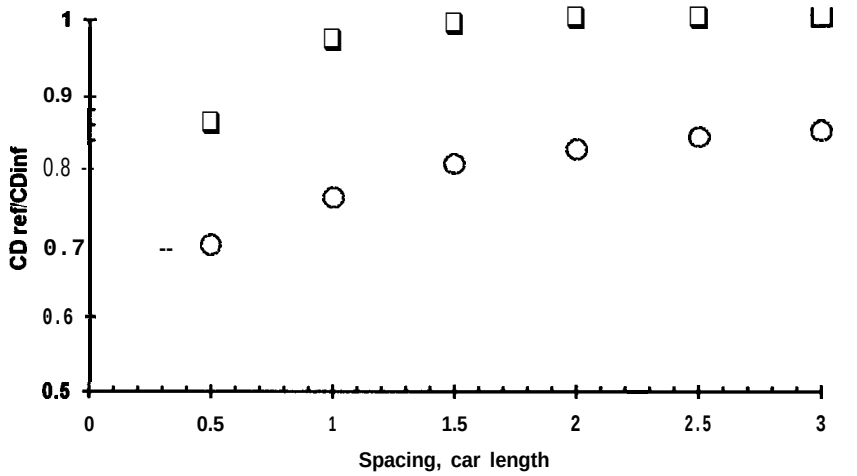

Corrected Platoon C_Ds

2nd Regular Platoon Data Set

Repeat. Both cars facing forward. Green was lead (stationary). CD_{∞} was measured at each location immediately before or after $CD_{platoon}$ was taken.

Single Car Data

Car#	Position	Drag	Side F	Yaw	CD_{ref}	Cp_{local}	CD_{local}
Green	181.6	6.255	0.431	-0.070	0.371	-0.086	0.341
Blue	274.4	6.137	-0.452	-0.047	0.364	-0.110	0.328
Blue	287.5	6.073	-0.634	-0.036	0.358	-0.110	0.323
Blue	305.4	6.089	-0.595	-0.029	0.361	-0.108	0.326
Blue	336.4	5.993	-0.556	-0.034	0.354	-0.103	0.321
Blue	367.3	6.009	-0.507	-0.043	0.356	-0.106	0.321
Blue	398.3	6.098	-0.421	-0.031	0.361	-0.115	0.324
Blue	429.3	6.046	-0.421	-0.053	0.358	-0.109	0.323

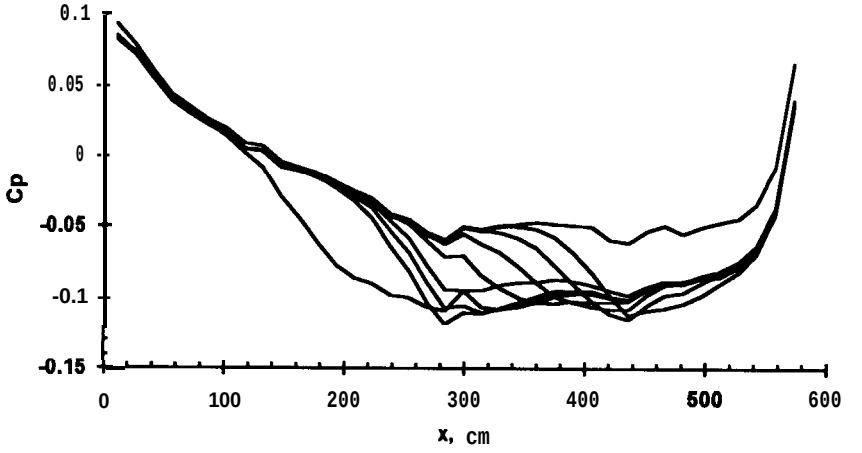

Static Pressure Distribution

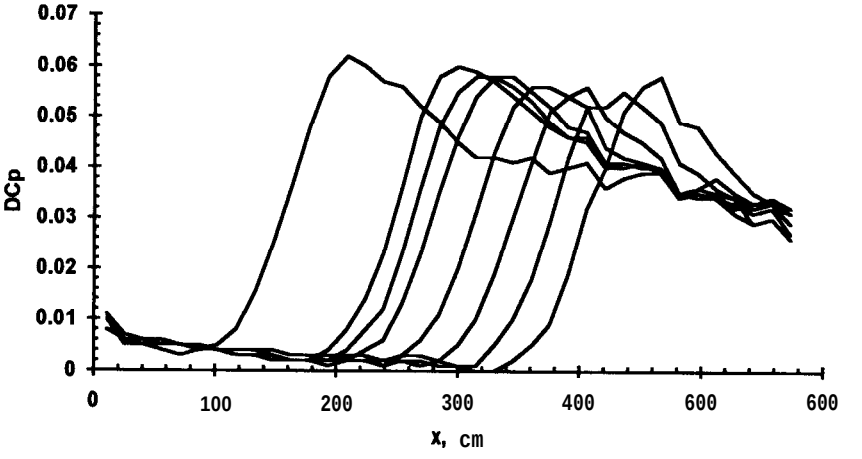

ΔC_p Distribution

Platoon Data

Uref=25 m/s, Position1=181.6 cm

Position2	Spacing	Drag1	SideF1	Yaw1	Drag2	SideF2	Yaw2	CD_{ref1}	CD_{ref2}	$\frac{CD_{ref1}}{CD_{\infty 1}}$	$\frac{CD_{ref2}}{CD_{\infty 2}}$
274.4	0.500	5.366	0.334	-0.065	4.234	-0.396	0.004	0.319	0.252	0.860	0.692
287.5	0.750	5.867	0.385	-0.057	4.438	-0.625	-0.001	0.349	0.264	0.940	0.736
305.4	1.000	6.071	0.369	-0.056	4.697	-0.602	0.001	0.360	0.278	0.969	0.771
336.4	1.500	6.262	0.365	-0.056	4.944	-0.660	-0.005	0.369	0.291	0.994	0.823
367.3	2.000	6.266	0.374	-0.060	5.058	-0.692	-0.021	0.372	0.300	1.002	0.844
398.3	2.500	6.270	0.385	-0.059	5.255	-0.649	-0.024	0.372	0.311	1.002	0.862
429.3	3.000	6.278	0.368	-0.057	5.287	-0.572	-0.043	0.372	0.313	1.002	0.875

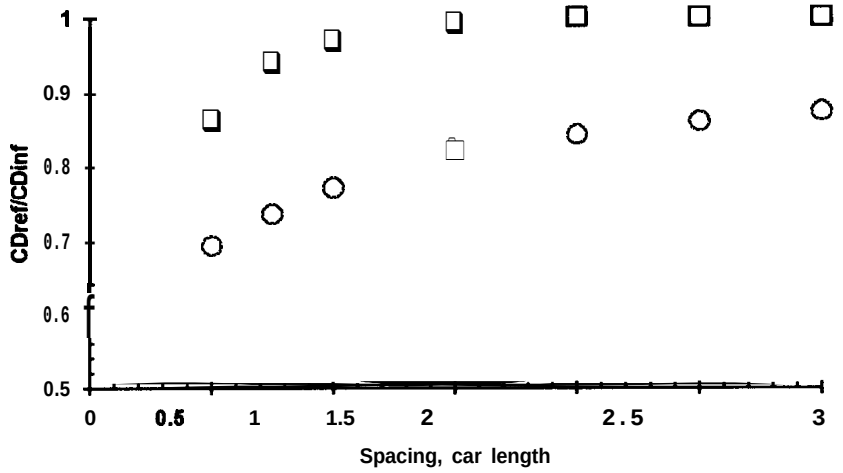

Uncorrected Platoon C_Ds

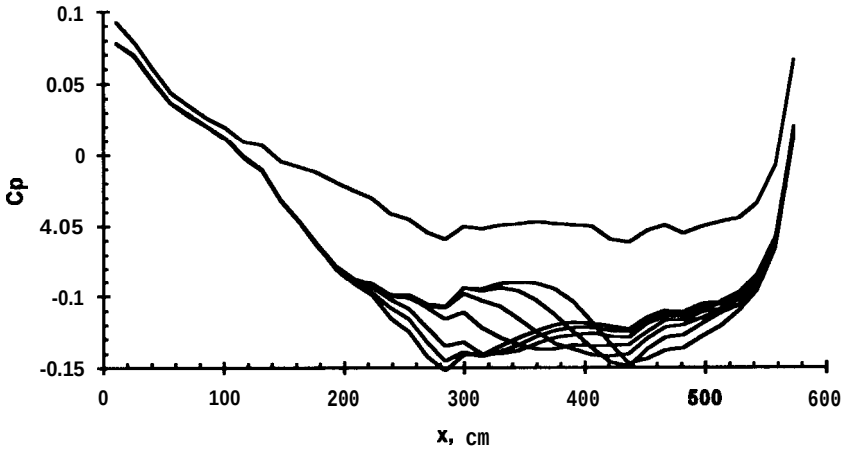

Static Pressure Distribution

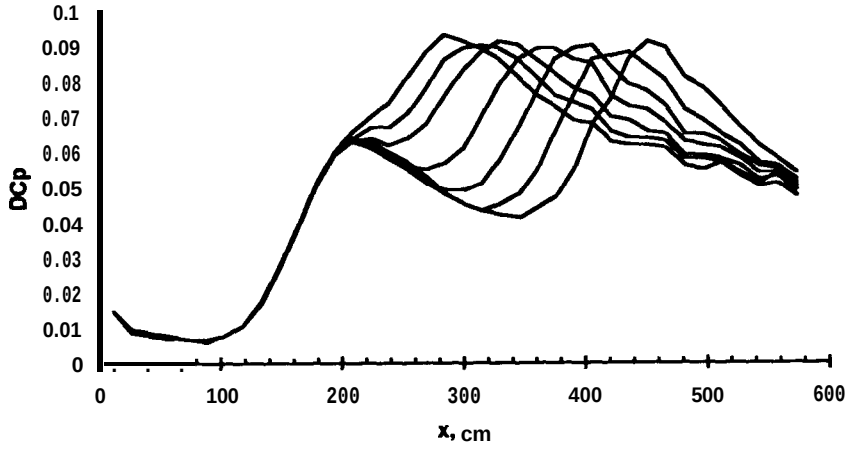

ΔC_p Distribution

Spacing	ΔCpmax	X_Cpmax	Cplocal2	Cplocal1	CDlocal2	CDlocal1	$\frac{CD_{loc1}}{CD_{\infty 1}}$	$\frac{CD_{loc2}}{CD_{\infty 2}}$
0.500	0.093	280.87	-0.152	-0.091	0.219	0.292	0.857	0.666
0.750	0.090	310.92	-0.142	-0.089	0.231	0.320	0.938	0.715
1.000	0.091	325.94	-0.140	-0.088	0.244	0.331	0.969	0.749
1.500	0.089	355.98	-0.137	-0.087	0.256	0.339	0.994	0.798
2.000	0.090	401.05	-0.141	-0.088	0.263	0.342	1.001	0.818
2.500	0.088	431.09	-0.149	-0.088	0.271	0.342	1.001	0.837
3.000	0.091	446.11	-0.144	-0.089	0.274	0.341	1.001	0.848

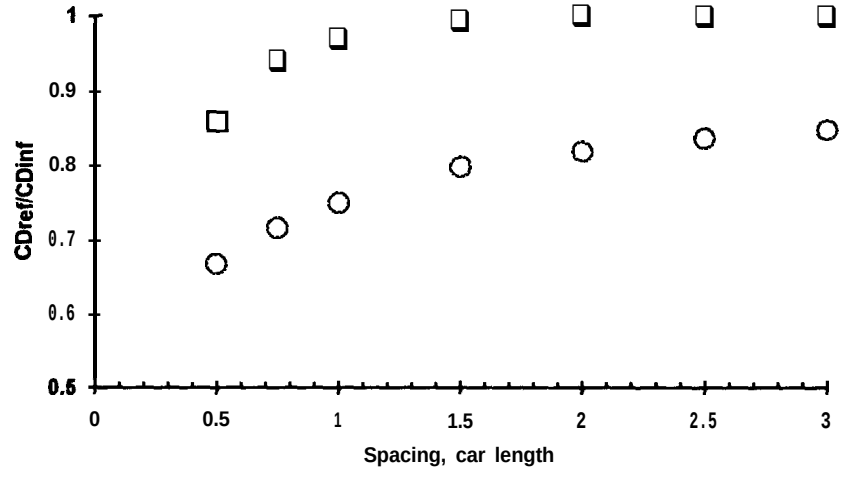

Corrected Platoon C_Ds

3rd Regular Platoon Data Set

Both cars facing stream. Blue was used as trailing car (stationary), Green was moved forward to spacing indicated. CD_∞ was measured at each location immediately before or after $CD_{platoon}$ was taken. U=25 m/s

Single Car Data

Car#	Position	Drag	Side F	Yaw	CD_{ref}	Cp_{local}	CD_{local}
Blue	429.3	6.058	-0.216	-0.055	0.357	-0.105	0.323
Green	181.6	6.224	0.383	-0.050	0.368	-0.086	0.339
Green	212.6	6.361	0.151	-0.081	0.377	-0.106	0.341
Green	243.5	6.330	0.280	-0.055	0.375	-0.120	0.335
Green	274.5	6.290	0.300	-0.099	0.371	-0.107	0.335
Green	305.4	6.247	0.218	-0.086	0.370	-0.106	0.335
Green	320.9	6.114	0.237	-0.088	0.361	-0.102	0.328
Green	336.4	6.160	0.254	-0.078	0.363	-0.100	0.330

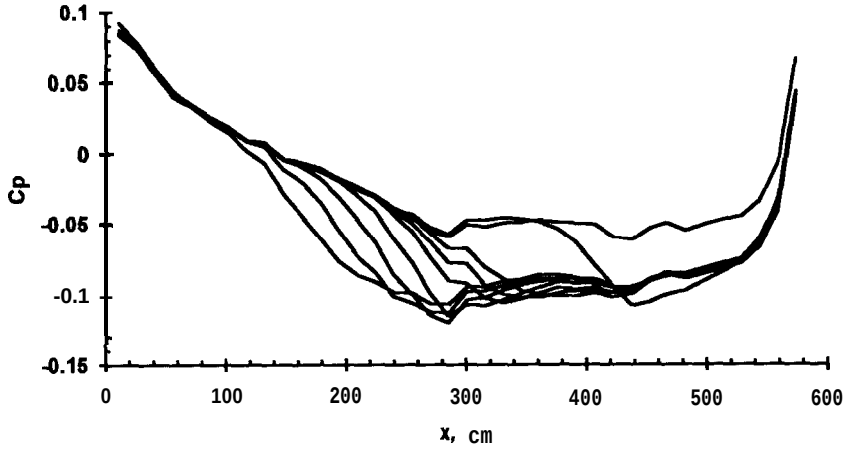

Static Pressure Distribution

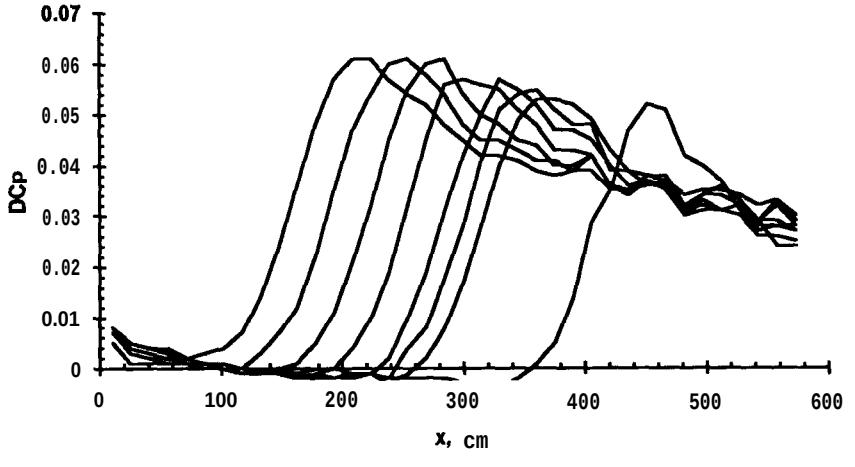

ΔC_p Distribution

Platoon Data

Uref=25 m/s, Position2=429.3 cm

Position1	Spacing	Drag1	SideF1	Yaw1	Drag2	SideF2	Yaw2	CD_{ref1}	CD_{ref2}	$\frac{CD_{ref1}}{CD_{\infty 1}}$	$\frac{CD_{ref2}}{CD_{\infty 2}}$
181.6	3.000	6.202	0.367	-0.053	5.234	-0.476	-0.048	0.367	0.310	0.998	0.868
212.6	2.500	6.377	0.126	-0.085	5.162	-0.476	-0.044	0.376	0.304	0.998	0.852
243.5	2.000	6.334	0.285	-0.055	5.050	-0.523	-0.033	0.374	0.298	0.998	0.835
274.5	1.500	6.213	0.290	-0.102	4.811	-0.480	-0.027	0.368	0.285	0.992	0.798
305.4	1.000	6.038	0.220	-0.088	4.487	-0.424	-0.021	0.357	0.265	0.965	0.742
320.9	0.750	5.673	0.236	-0.090	4.230	-0.421	-0.017	0.336	0.251	0.930	0.703
336.4	0.500	5.213	0.312	-0.071	3.959	-0.224	0.005	0.308	0.234	0.848	0.655

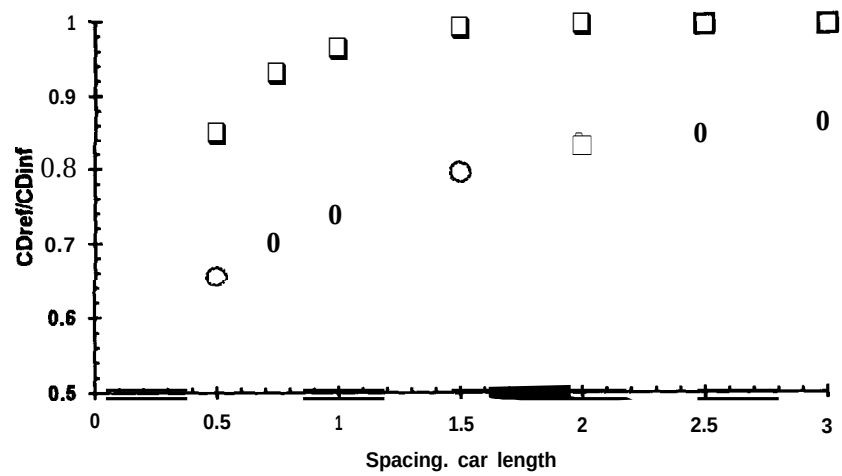

Uncorrected Platoon C_Ds

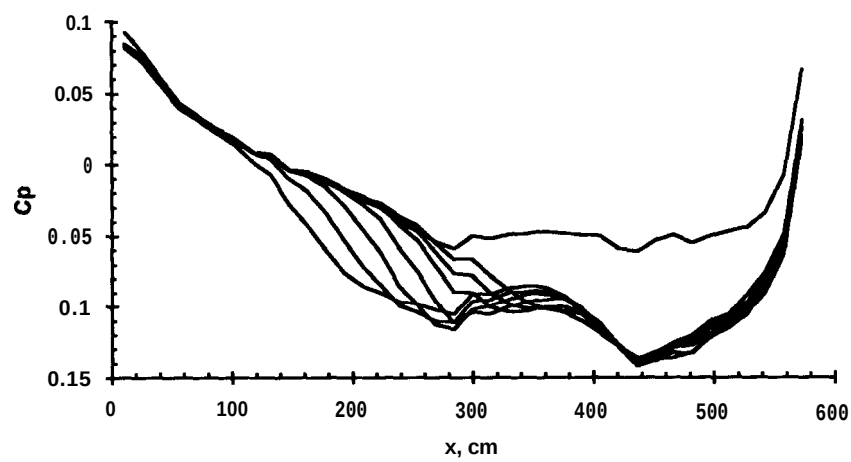

Static Pressure Distribution

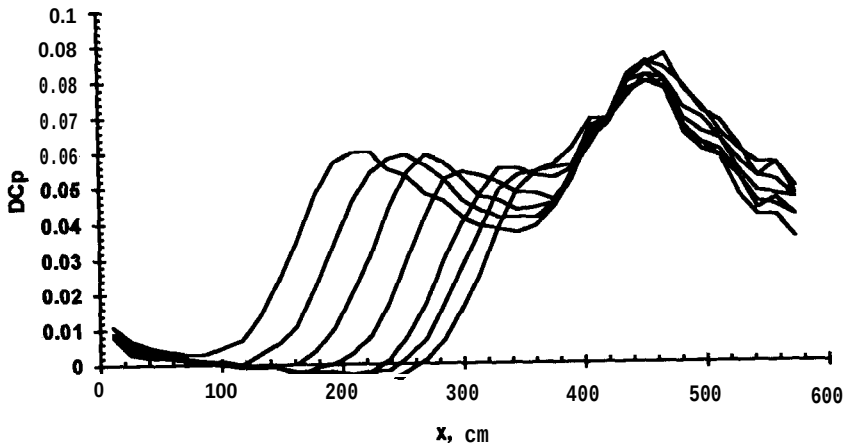

ΔC_p Distribution

Spacing	_Cpmax	X_Cpmax	Cplocal2	Cplocal1	CDlocal2	CDlocal1	$\frac{CD_{loc1}}{CD_{\infty 1}}$	$\frac{CD_{loc2}}{CD_{\infty 2}}$
3.000	0.060	205.76	-0.136	-0.085	0.273	0.339	0.999	0.845
2.500	0.059	250.83	-0.138	-0.104	0.267	0.340	0.999	0.828
2.000	0.059	265.85	-0.137	-0.113	0.262	0.336	1.005	0.812
1.500	0.054	295.89	-0.134	-0.104	0.251	0.333	0.994	0.777
1.000	0.055	325.49	-0.132	-0.104	0.235	0.324	0.967	0.726
0.750	0.056	386.03	-0.134	-0.105	0.221	0.304	0.928	0.685
0.500	0.061	386.03	-0.132	-0.110	0.207	0.278	0.841	0.640

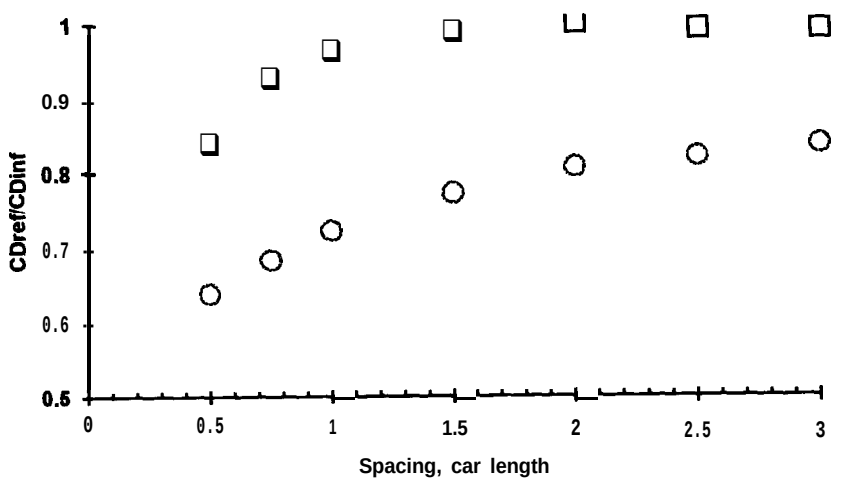

Corrected Platoon C_Ds

Appendix B: 2 ,3 & 4-Car Platoon Series

In this series, the CD of each model alone at each position was recorded just before platoon measurements were taken.

Single Car Data

Car1#	Position	Drag	Side F	Yaw	C_{Dref}	C_{Plocal}	C_{Dlocal}
blue	150.65	5.872	-0.370	0.004	0.350	-0.0731	0.326
blue	104.22	5.666	-0.369	0.003	0.337	-0.0192	0.331
blue	88.75	5.523	-0.256	0.012	0.327	-0.0001	0.326
blue	73.25	5.462	-0.380	0.012	0.323	0.0204	0.330
blue	57.79	5.207	-0.317	0.006	0.309	0.0293	0.319
green	243.52	6.216	0.280	-0.044	0.372	-0.1223	0.331
green	228.04	6.284	-0.044	-0.066	0.373	-0.1182	0.333
green	197.08	6.218	0.172	-0.076	0.368	-0.1035	0.334
green	181.61	6.110	0.346	-0.046	0.365	-0.088	0.336
red	305.44	5.901	-0.612	0.001	0.350	-0.1078	0.316
red	289.94	5.864	-0.718	-0.002	0.348	-0.1077	0.314
yellow	429.26	6.195	-0.663	-0.028	0.365	-0.1054	0.330
yellow	413.79	6.190	-0.646	-0.006	0.368	-0.1159	0.330
yellow	382.83	6.088	-0.740	-0.011	0.361	-0.1062	0.326

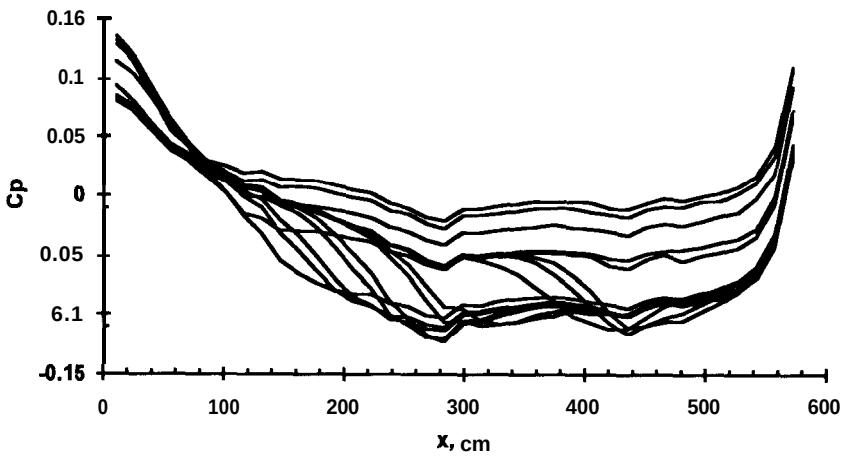

Static Pressure Distribution

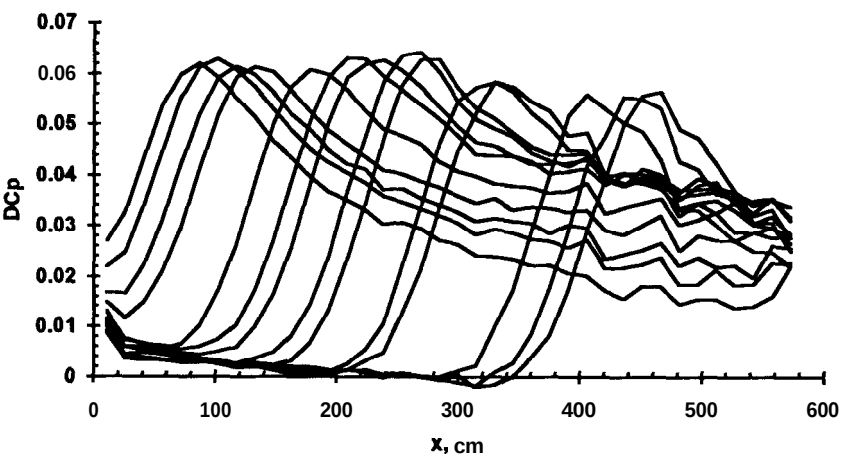

ΔC_p Distribution

2-Car Platoon Data

U_{ref} = 25 m/s

Spacing	Position$_1$	Drag$_1$	Side F$_1$	Yaw$_1$	Position$_2$	Drag$_2$	Side F$_2$	Yaw$_2$	C_{Dref1}	C_{Dref2}	$\frac{C_{Dref}}{C_{D1}}$	$\frac{C_{Dref}}{C_{D2}}$
0.50	104.22	4.663	-0.298	0.006	197.08	4.302	0.072	-0.065	0.277	0.256	0.837	0.762
0.50	197.08	5.300	0.208	-0.073	289.94	3.974	-0.249	0.030	0.315	0.236	0.938	0.752
0.75	88.75	5.022	-0.230	0.009	197.08	4.541	-0.030	-0.068	0.297	0.269	0.911	0.801
0.75	197.08	5.759	0.220	-0.072	305.44	4.158	-0.462	0.014	0.347	0.251	1.033	0.794
1.00	181.61	5.912	0.360	-0.046	305.44	4.499	-0.554	0.022	0.352	0.268	1.048	0.848
1.00	305.44	5.713	-0.644	0.023	429.26	4.684	-0.225	-0.023	0.340	0.279	1.076	0.845
1.50	150.65	5.862	-0.369	0.004	305.44	4.974	-0.372	-0.014	0.347	0.294	1.064	0.930
1.50	228.04	6.227	-0.022	-0.063	382.83	4.959	-0.489	0.012	0.370	0.294	1.111	0.902
2.00	104.22	5.677	-0.371	0.001	289.94	4.967	-0.547	-0.010	0.335	0.293	1.012	0.933
2.00	57.79	5.150	-0.323	0.004	243.52	5.211	0.029	-0.056	0.307	0.310	0.962	0.937
2.00	243.52	6.240	0.266	-0.047	429.26	5.094	-0.505	0.014	0.370	0.302	1.118	0.915
2.00	197.08	6.227	0.155	-0.078	382.83	5.188	-0.561	0.011	0.368	0.307	1.095	0.942
2.50	88.75	5.479	-0.244	0.014	305.44	4.935	-0.573	-0.001	0.326	0.293	1.000	0.927
2.50	197.08	6.204	0.189	-0.076	413.79	5.319	-0.556	0.014	0.368	0.315	1.095	0.955
5.00	57.79	5.199	-0.327	0.004	429.26	5.232	-0.567	-0.017	0.309	0.311	0.969	0.942

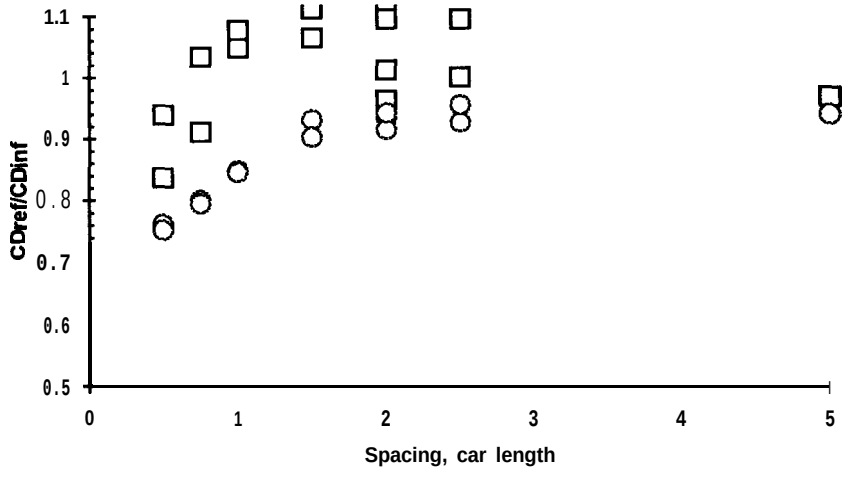

Uncorrected Platoon C_{DS}

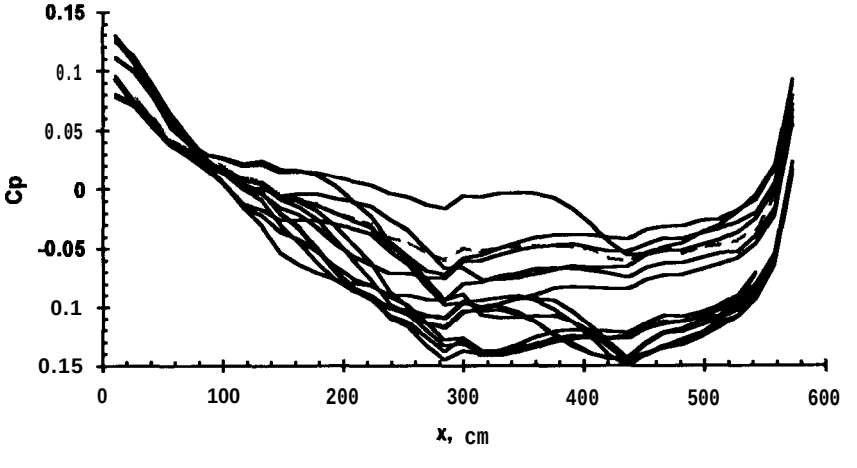

Static Pressure Distribution

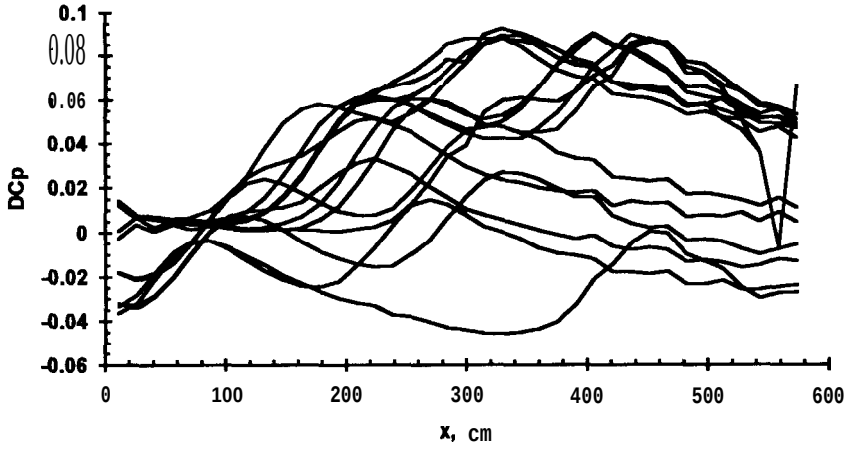

AC, Distribution

Spacing	DCp_{max}	$X_{DCp_{max}}$	$C_{plocal1}$	$C_{plocal2}$	$C_{Dlocal1}$	$C_{Dlocal2}$	$\frac{C_{Dloc1}}{C_{D\infty 1}}$	$\frac{C_{Dloc2}}{C_{D\infty 2}}$
0.50	0.0514	223.30	-0.0219	-0.081	0.271	0.237	0.820	0.705
0.50	0.088	329.72	-0.109	-0.1374	0.284	0.208	0.847	0.662
0.75	0.0335	223.30	-0.0003	-0.0631	0.297	0.253	0.909	0.753
0.75	0.0922	329.72	-0.1069	-0.1416	0.314	0.220	0.935	0.696
1.00	0.0895	344.92	-0.1007	-0.1376	0.320	0.236	0.954	0.746
1.00	0.0877	451.33	-0.1094	-0.1407	0.306	0.244	0.970	0.741
1.50	0.0877	329.72	-0.0703	-0.1371	0.324	0.259	0.994	0.820
1.50	0.0893	405.73	-0.1141	-0.1396	0.332	0.258	0.995	0.792
2.00	0.0478	329.72	-0.0171	-0.0972	0.330	0.267	0.996	0.852
2.00	0.0149	268.91	0.0298	-0.0687	0.316	0.290	0.991	0.877
2.00	0.0861	466.54	-0.1183	-0.1351	0.331	0.266	1.000	0.807
2.00	0.0899	405.73	-0.1009	-0.1402	0.334	0.269	0.996	0.824
2.50	0.027	329.72	0.0019	-0.0764	0.326	0.273	1.000	0.863
2.50	0.0895	436.13	-0.1009	-0.15	0.334	0.274	0.995	0.831
5.00	0.0007	451.33	0.0298	-0.0537	0.318	0.295	0.999	0.894

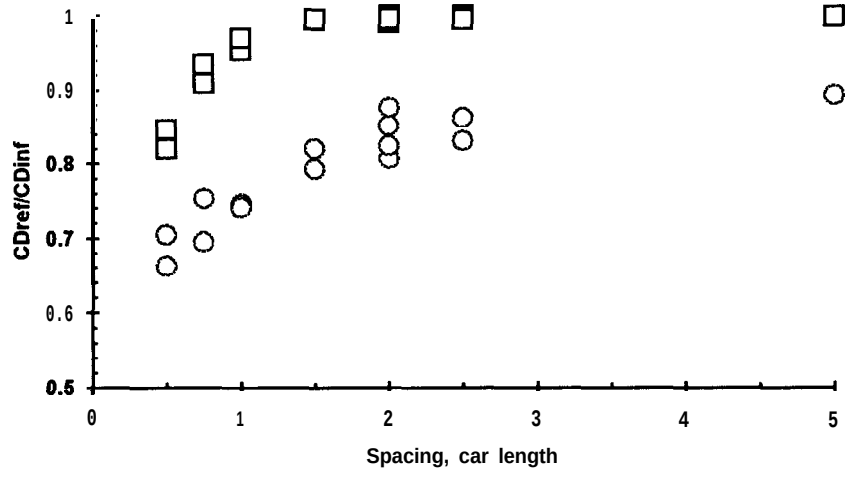

Corrected Platoon C_Ds

3-Car Platoon Data

U_{ref} = 25 m/s

Spacing	Position1	$Drag_1$	Side F_1	Yaw_1	Position2	Drag2	Side F_2	Yaw2	Position3	$Drag_3$	Side F_3	Yaw3
0.50	104.22	4.651	-0.301	0.005	197.08	3.646	0.149	-0.055	289.94	4.016	-0.187	0...014
0.50	197.08	5.297	0.233	-0.069	289.94	3.349	-0.170	0.030	382.83	4.210	-0.378	0.041
0.75	88.75	5.000	-0.233	0.011	197.08	4.124	-0.014	-0.071	305.44	4.009	-0.341	0.013
0.75	197.08	5.786	0.241	-0.071	305.44	3.795	-0.386	0.020	413.79	4.363	-0.330	0.020
1 .00	57.79	4.868	-0.312	0.001	181.61	4.497	0.385	-0.024	305.44	4.172	-0.495	0.020
1 .00	181.61	5.884	0.340	-0.049	305.44	4.304	-0.573	0.020	429.26	4.508	-0.356	0.008
1.50	73.25	5.332	-0.365	0.011	228.04	5.065	-0.137	-0.073	382.83	4.618	-0.443	0.005
2.00	57.79	5.155	-0.329	0.003	243.52	5.199	0.024	-0.058	429.26	4.748	-0.447	0.011

Spacing	C_{Dref1}	C_{Dref2}	C_{Dref3}	$\frac{C_{Dref}}{C_{D1}}$	$\frac{C_{Dref}}{C_{D2}}$	$\frac{C_{Dref}}{C_{D3}}$
0.50	0.276	0.216	0.238	0.819	0.583	0.686
0.50	0.313	0.198	0.249	0.844	0.570	0.690
0.75	0.296	0.244	0.238	0.907	0.658	0.678
0.75	0.343	0.225	0.259	0.924	0.642	0.703
1.00	0.291	0.268	0.249	0.939	0.735	0.710
1.00	0.352	0.258	0.270	0.965	0.735	0.740
1.50	0.317	0.301	0.275	0.982	0.808	0.761
2.00	0.307	0.309	0.282	0.991	0.832	0.774

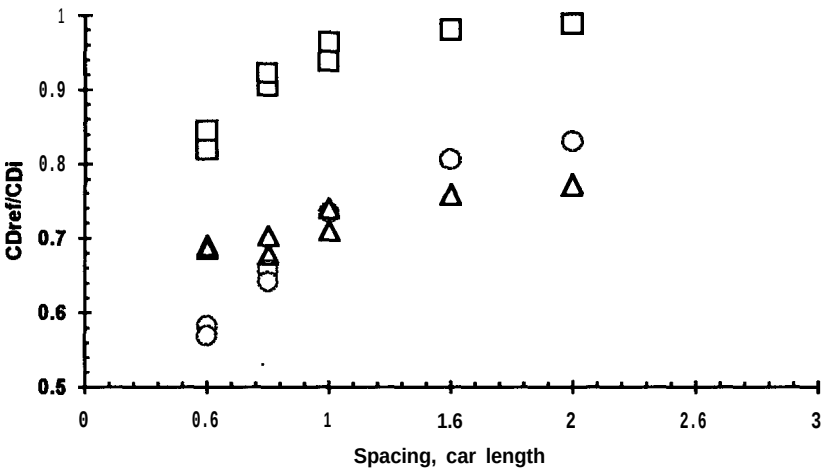

Uncorrected Platoon C_Ds

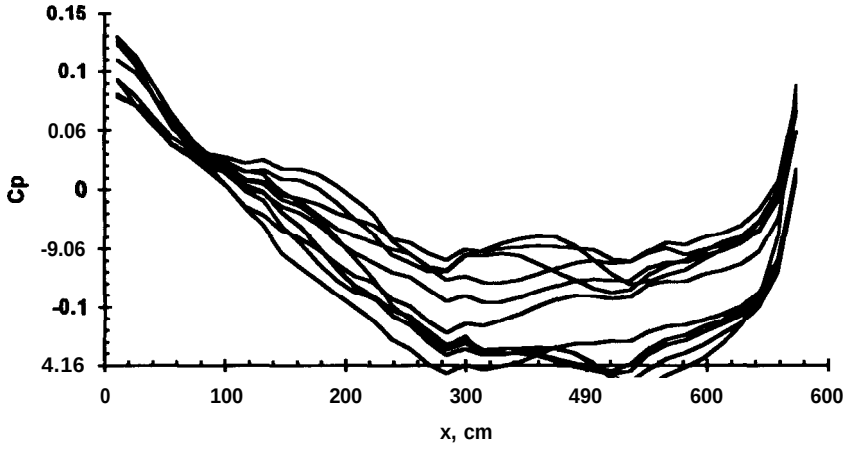

Static Pressure Distribution

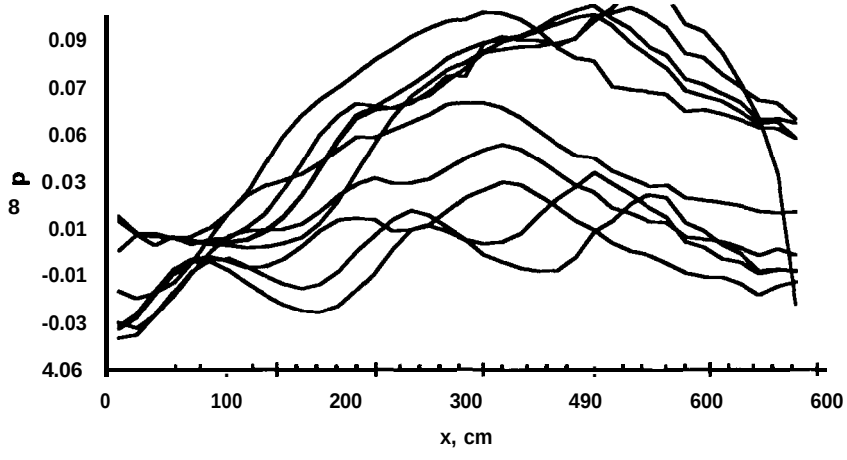

ΔC_p Distribution

Spacing	DCp_{max}	$X_{DCp_{max}}$	Cp_{local1}	Cp_{local2}	Cp_{local3}	$C_{Dlocal1}$	$C_{Dlocal2}$	$C_{Dlocal3}$	$\frac{C_{Dloc1}}{C_{D\infty 1}}$	$\frac{C_{Dloc2}}{C_{D\infty 2}}$	$\frac{C_{Dloc3}}{C_{D\infty 3}}$
0.50	0.064	299.31	-0.0211	-0.0929	-0.1137	0.270	0.198	0.214	0.817	0.593	0.682
0.50	0.1045	405.73	-0.1073	-0.1399	-0.1548	0.283	0.174	0.216	0.843	0.554	0.661
0.75	0.0456	329.72	0.0005	-0.0699	-0.095	0.296	0.228	0.217	0.908	0.684	0.687
0.75	0.1036	436.13	-0.1022	-0.1353	-0.1641	0.311	0.198	0.222	0.928	0.628	0.674
1.00	0.0297	329.72	0.0283	-0.0392	-0.0791	0.299	0.258	0.231	0.938	0.769	0.731
1.00	0.1147	451.33	-0.0878	-0.138	-0.1677	0.324	0.226	0.231	0.965	0.717	0.701
1.50	0.0337	405.73	0.0219	-0.0693	-0.084	0.324	0.282	0.253	0.984	0.845	0.777
2.00	0.0242	451.33	0.0305	I-0.0681	I-0.0772	0.316	0.289	0.262	0.992	0.875	0.795

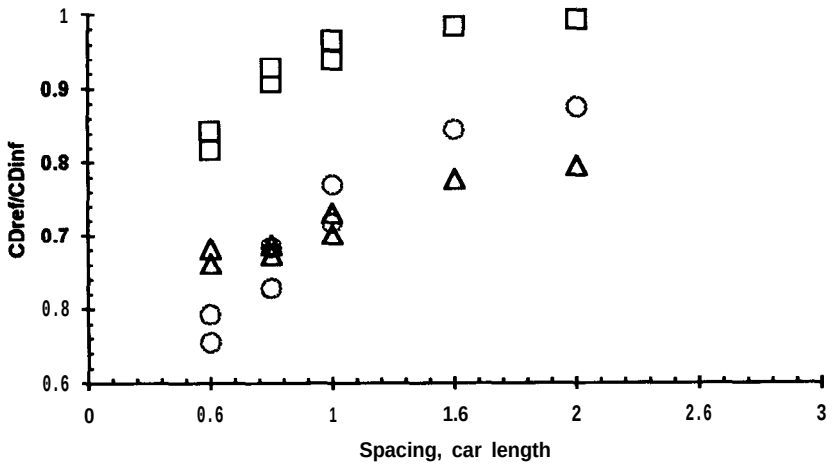

Corrected Platoon C_Ds

4-Car Platoon Data

$U_{ref} = 25$ m/s

Spacing	Position$_1$	Drag$_1$	Side F$_1$	Yaw$_1$	Position$_2$	Drag$_2$	Side F$_2$	Yaw$_2$	Position$_3$	Drag$_3$	Side F$_3$	Yaw$_3$
0.5	104.22	4.654	-0.311	0.004	197.08	3.634	0.141	-0.057	289.94	3.353	-0.168	0.022
0.75	88.75	4.970	-0.238	0.011	197.08	4.093	-0.013	-0.069	305.44	3.585	-0.230	0.026
1	57.79	4.873	-0.315	0.001	181.61	4.488	0.437	-0.019	305.44	3.980	-0.464	0.028

Spacing	Position$_4$	Drag$_4$	Side F$_4$	Yaw$_4$	C_{Dref1}	C_{Dref2}	C_{Dref3}	C_{Dref4}	$\frac{C_{Dref}}{C_{D1}}$	$\frac{C_{Dref}}{C_{D2}}$	$\frac{C_{Dref}}{C_{D3}}$	$\frac{C_{Dref}}{C_{D4}}$
0.5	382.83	4.219	-0.301	0.027	0.276	0.215	0.199	0.250	0.817	0.579	0.571	0.693
0.75	413.79	4.124	-0.237	0.013	0.296	0.244	0.213	0.246	0.906	0.657	0.609	0.667
1	429.26	4.156	-0.353	0.022	0.291	0.268	0.238	0.248	0.940	0.734	0.678	0.680

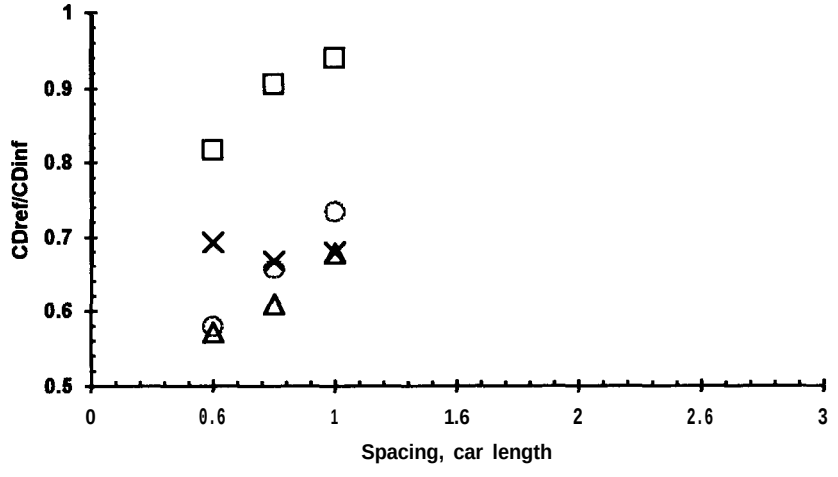

Uncorrected Platoon C_Ds

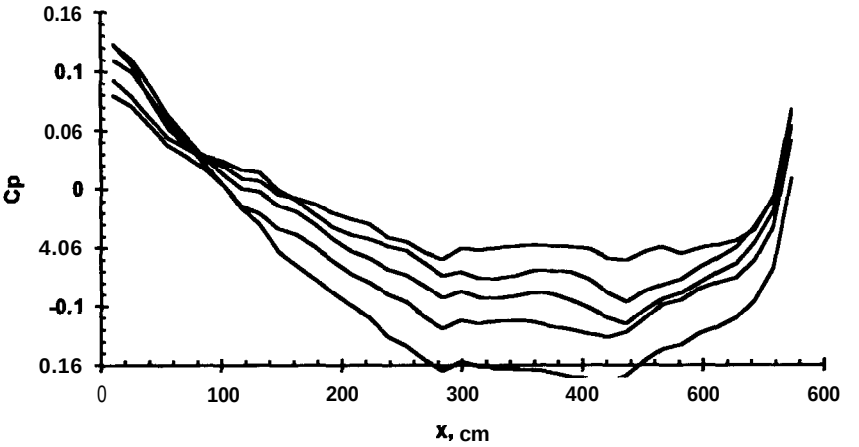

Static Pressure Distribution

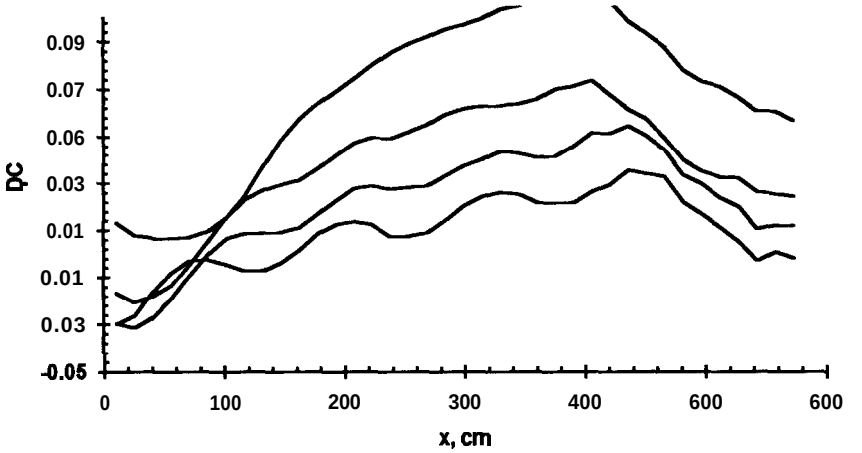

ΔC_p Distribution

Spacing	DCp_{max}	$X_{DCp_{max}}$	$C_{plocal1}$	$C_{plocal2}$	$C_{plocal3}$	$C_{plocal4}$	$C_{Dlocal1}$	$C_{Dlocal2}$	$C_{Dlocal3}$	$C_{Dlocal4}$
0.5	0.0736	405.73	-0.0200	-0.0900	-0.1126	-0.1239	0.270	0.197	0.178	0.222
0.75	0.0545	436.13	0.0007	-0.0684	-0.0909	-0.1150	0.296	0.228	0.196	0.220
1	0.0357	436.13	0.0288	-0.0387	-0.0734	-0.0962	0.300	0.258	0.221	0.226

Spacing	$\frac{C_{Dloc1}}{C_{D\infty1}}$	$\frac{C_{Dloc2}}{C_{D\infty2}}$	$\frac{C_{Dloc3}}{C_{D\infty3}}$	$\frac{C_{Dloc4}}{C_{D\infty4}}$
0.5	0.816	0.588	0.513	0.616
0.75	0.907	0.680	0.558	0.599
1	0.940	0.769	0.632	0.621

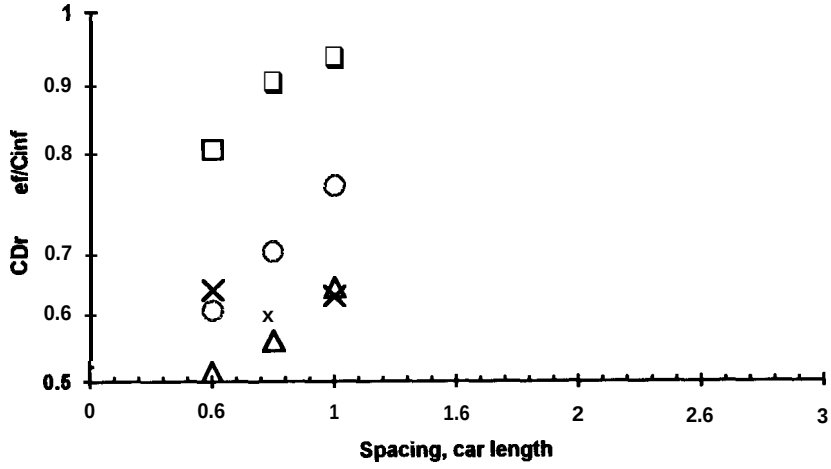

Corrected Platoon C_Ds

Appendix C: Suction Fan Performance

Manufacturer's Data

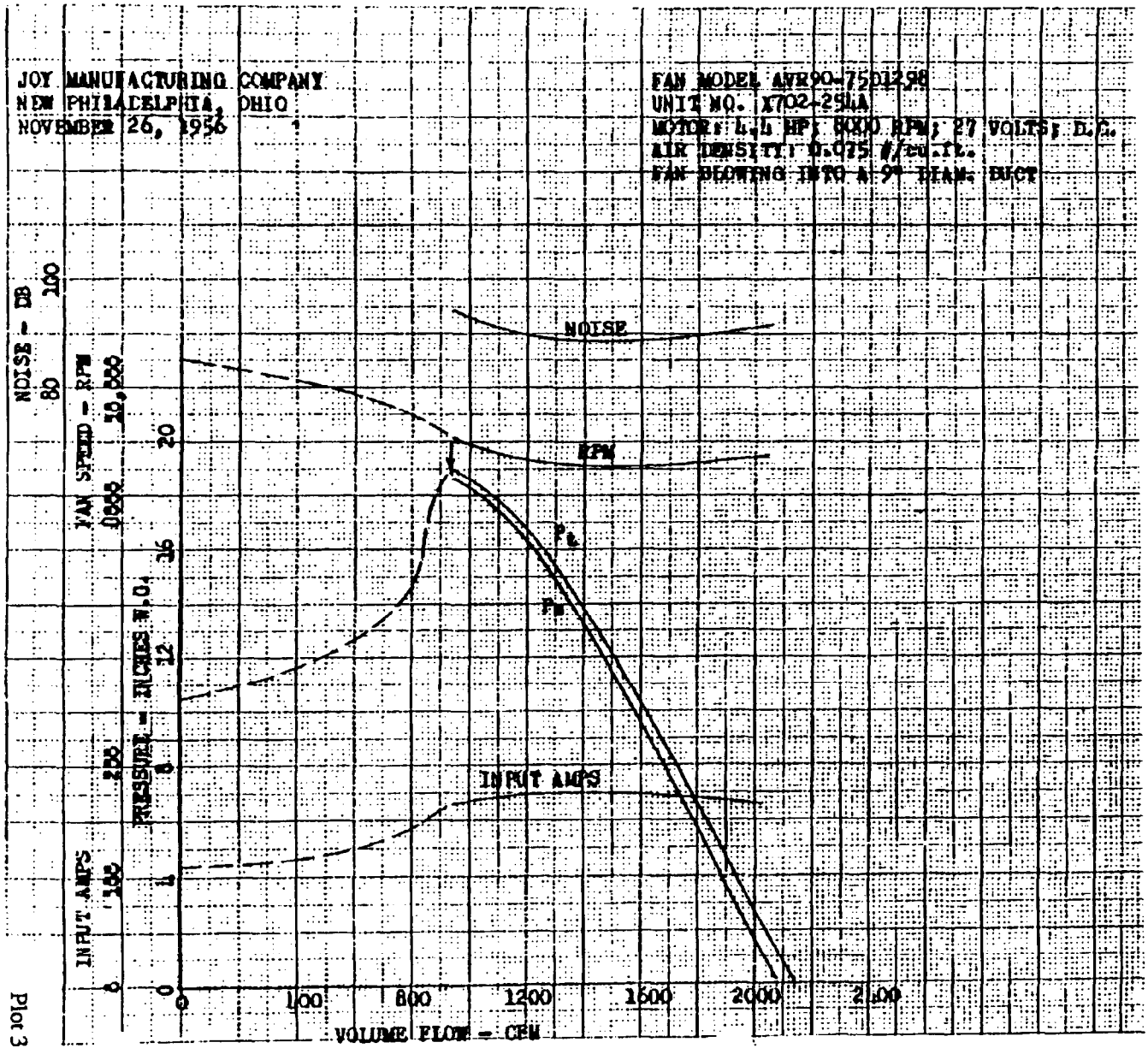

Pressure us Volume Flow (March 24, 1992)
(Metric Units)

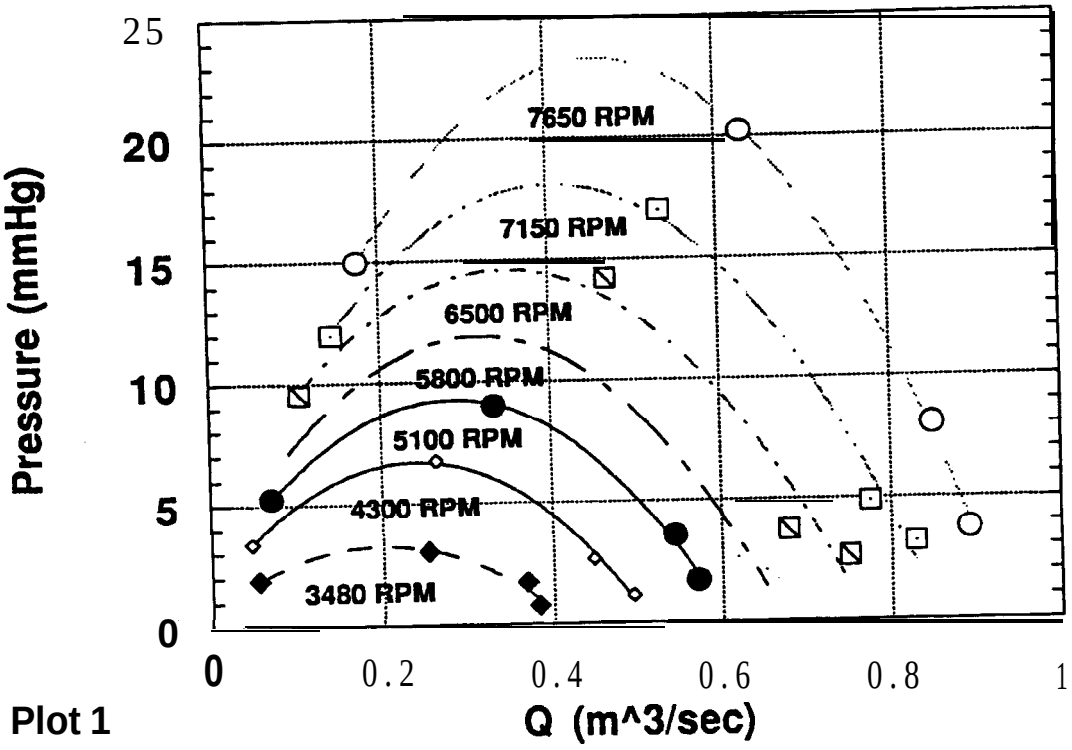

Plot 1

Pressure us Volume Flow (March 24,1992)
(English Units)

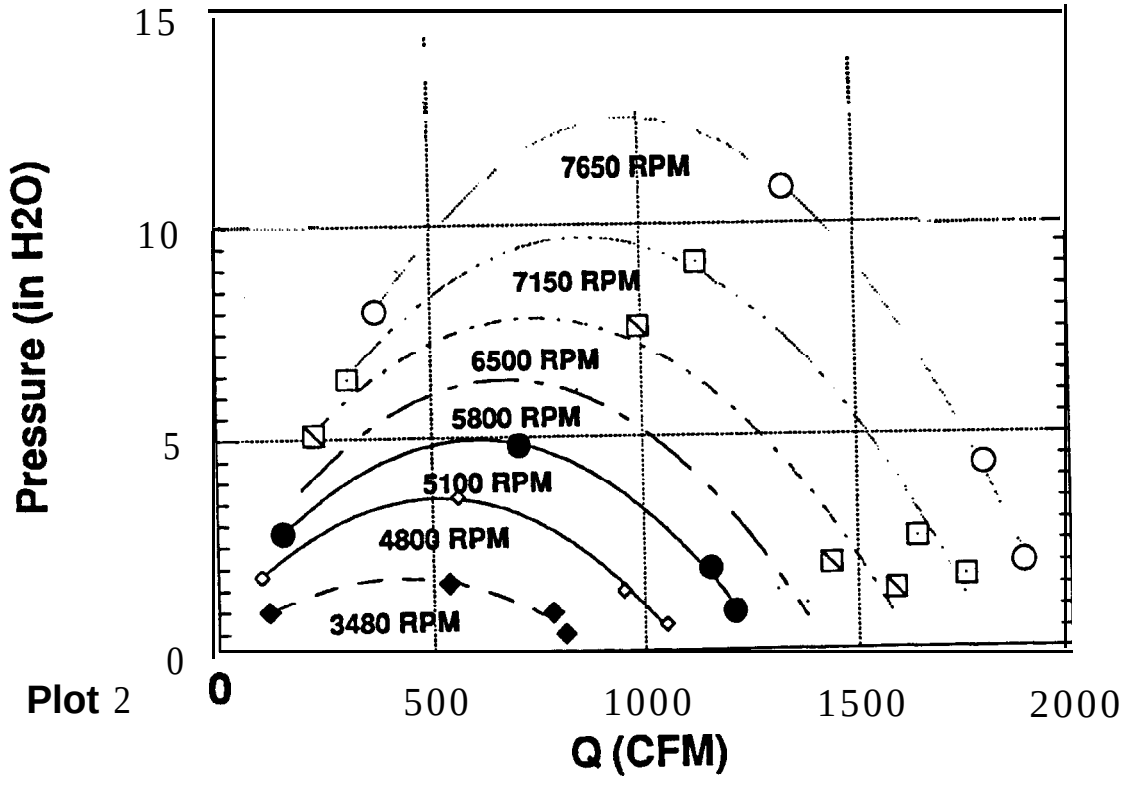

Plot 2